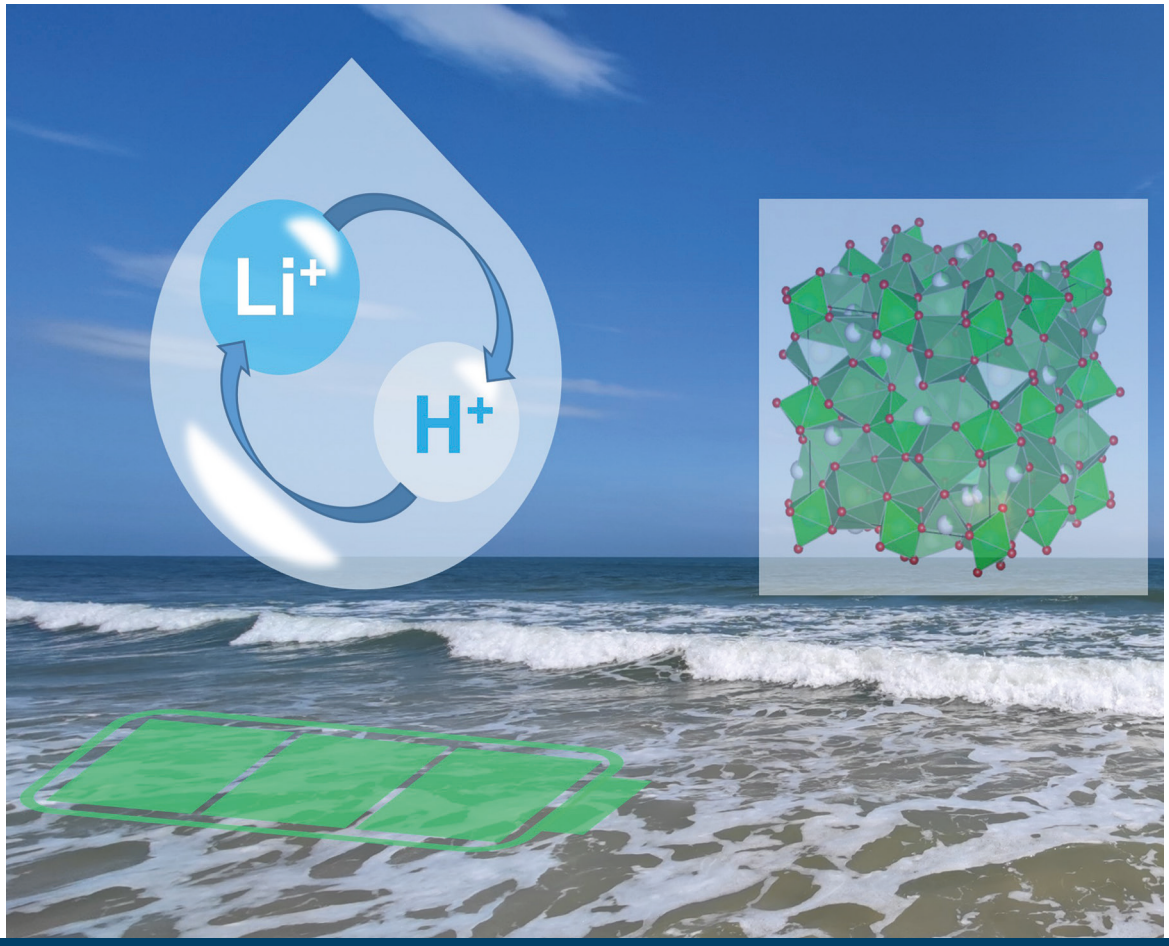

Sustainable Fabrication of Ceramic Solid Electrolytes for Solid-State Lithium Batteries

Ruijie Ye

Energie & Umwelt / Energy & Environment
Band / Volume 607
ISBN 978-3-95806-694-6

Mitglied der Helmholtz-Gemeinschaft

JÜLICH
Forschungszentrum

Schriften des Forschungszentrums Jülich
Reihe Energie & Umwelt / Energy & Environment Band / Volume 607

Forschungszentrum Jülich GmbH
Institut für Energie- und Klimaforschung
Werkstoffsynthese und Herstellungsverfahren (IEK-1)

Sustainable Fabrication of Ceramic Solid Electrolytes for Solid-State Lithium Batteries

Ruijie Ye

Schriften des Forschungszentrums Jülich
Reihe Energie & Umwelt / Energy & Environment Band / Volume 607

ISSN 1866-1793 ISBN 978-3-95806-694-6

Bibliografische Information der Deutschen Nationalbibliothek.
Die Deutsche Nationalbibliothek verzeichnet diese Publikation in der
Deutschen Nationalbibliografie; detaillierte Bibliografische Daten
sind im Internet über http://dnb.d-nb.de abrufbar.

Herausgeber und Vertrieb:	Forschungszentrum Jülich GmbH Zentralbibliothek, Verlag 52425 Jülich Tel.: +49 2461 61-5368 Fax: +49 2461 61-6103 zb-publikation@fz-juelich.de www.fz-juelich.de/zb
Umschlaggestaltung:	Grafische Medien, Forschungszentrum Jülich GmbH
Druck:	Grafische Medien, Forschungszentrum Jülich GmbH
Copyright:	Forschungszentrum Jülich 2023

Schriften des Forschungszentrums Jülich
Reihe Energie & Umwelt / Energy & Environment, Band / Volume 607

D 82 (Diss. RWTH Aachen University, 2023)

ISSN 1866-1793
ISBN 978-3-95806-694-6

Vollständig frei verfügbar über das Publikationsportal des Forschungszentrums Jülich (JuSER)
unter www.fz-juelich.de/zb/openaccess.

A. Abstract

Solid-state lithium batteries (SSLBs) are considered to be one of the most promising next-generation Li batteries due to their high capacity and intrinsic safety. Their sustainable processing offers additional advantages over conventional batteries in terms of ecological and economic benefits. However, the sustainable processing of SSLBs has been only sporadically investigated and need to be optimized.

Garnet-type $Li_7La_3Zr_2O_{12}$ (LLZO) is one representative of oxide-based solid electrolytes (SE) for SSLBs. A thin freestanding LLZO sheet can be fabricated by tape-casting and used *e.g.* as separator in SSLBs, since tape-casting is an industrially established process and enables large-scale production of such SEs. However, organic solvents and additives employed in conventional slurry recipes for tape-casting give rise to health and safety concerns and additionally cause high cost for solvent recovery. Hence, development of a water-based processing route reduces both manufacturing costs and environmental footprint.

In this work, a tape-casting process for LLZO SEs is developed using water as solvent, the water-soluble biopolymer as binder and other harmless polymers as plasticizers. During the aqueous processing, a Li^+/H^+ exchange takes place, but this Li^+/H^+ exchange reaction is reversible in the procedure and results in the formation of stoichiometric cubic LLZO at the end. The obtained free-standing LLZO thin sheets have a relative density of 90% to the theoretical density and exhibit an ionic conductivity of 0.15 mS cm^{-1} at room temperature.

Afterwards, a sustainable, water-based processing route for the garnet-supported SSLB featuring a $LiFePO_4$-polyethylene oxide (LFP-PEO) composite cathode is also presented. After optimizing the composition of the cathode, full cells composed of the water-processed LFP-PEO cathode and the prepared LLZO thin sheet are assembled. The full cells deliver a specific capacity of 136 mAh g^{-1} at a current density of 50 µA cm^{-2} with a Coulombic efficiency above 99% over 50 cycles.

Furthermore, the developed aqueous tape-casting method is adopted to fabricate ceramic $LiCoO_2$ (LCO)-LLZO composite cathodes. After the optimization of processing parameters including pre-densification pressure and sintering conditions, dense free-standing LCO-LLZO cathodes are obtained, which have no secondary phases produced by side reactions. Enabled by a modified

solid polymer membrane prepared in aqueous solution, this cathode is integrated into garnet-supported SSLBs. The assembled SSLBs deliver high areal capacities (> 3 mAh cm^{-2}) and show improved cycling stability (lower capacity decay) comparing to other bulk-type SSLBs with LCO-LLZO cathodes.

In this work, the first sustainably produced LLZO SE was reported, where water and eco-friendly polymers were applied within tape-casting. On this basis, two types of SSLBs were successfully developed with LFP-PEO and LCO-LLZO composite cathodes, respectively, which were fabricated for the first time by sustainable water-based processes. This work demonstrated the feasibility of an environmentally friendly processing route for SSLBs. Further optimization, *e.g.* enhancing the power density and the cycling stability, are needed to achieve the best of both commercial and ecological benefits.

B. Kurzfassung

Aufgrund ihrer hohen Kapazität und Sicherheit gelten Festkörper-Lithiumbatterien (SSLB) als eine der vielversprechendsten Li-Batterien der nächsten Generation. Ihre nachhaltige Verarbeitung könnte zusätzliche ökologische und ökonomische Vorteile gegenüber konventionellen Batterien bieten. Allerdings ist diese oft nur sporadisch untersucht, und muss optimiert werden.

Der granat-artige $Li_7La_3Zr_2O_{12}$ (LLZO) ist ein Vertreter der oxidbasierten Festelektrolyte (SE) für SSLBs. Durch Foliengießen, das ein industriell etablierter Prozess ist, wird eine dünne, freistehende LLZO-Schicht in großem Maßstab hergestellt. Die organischen Lösungsmittel und Zusatzstoffe, die in den herkömmlichen Schlickerrezepten für das Foliengießen verwendet werden, führen jedoch zu Gesundheits- und Sicherheitssorge, und verursachen außerdem hohe Kosten für die Lösungsmittelrückgewinnung. Daher verringert die Entwicklung eines wasserbasierten Verfahrens sowohl die Herstellungskosten als auch die Umweltbelastung.

In dieser Arbeit wird ein Foliengießen-Verfahren für LLZO-SEs entwickelt, das Wasser als Lösungsmittel, das wasserlösliche Biopolymer als Bindemittel und andere unbedenkliche Polymere als Weichmacher verwendet. Während der wässrigen Verarbeitung findet ein Li^+/H^+-Austausch statt. Aber diese Li^+/H^+-Austauschreaktion ist in dem Verfahren reversibel und führt am Ende zur Bildung von stöchiometrischem kubischem LLZO. Die erhaltenen freistehenden LLZO-Dünnschichten haben eine relative Dichte von 90% der theoretischen Dichte und weisen eine Ionenleitfähigkeit von 0,15 mS cm^{-1} bei Raumtemperatur auf.

Anschließend wird ein nachhaltiger, wasserbasierter Verarbeitungsweg für die granatgestützte SSLB mit einer $LiFePO_4$-Polyethylenoxid (LFP-PEO)-Mischkathode vorgestellt. Nach der Optimierung der Kathodenzusammensetzung werden die Vollzellen aus der wasserverarbeiteten LFP-PEO-Kathode und der vorbereiteten LLZO-Dünnschicht zusammengesetzt. Die Vollzellen liefern eine spezifische Kapazität von 136 mAh g^{-1} bei einer Stromdichte von 50 µA cm^{-2} mit einem Coulombischen Wirkungsgrad von über 99% über 50 Zyklen.

Darüber hinaus wird die entwickelte wässrige Foliengießmethode zur Herstellung von keramischen $LiCoO_2$ (LCO)-LLZO-Mischkathoden eingesetzt. Nach der Optimierung der Verarbeitungsparameter, einschließlich des Vorverdichtungsdrucks und der Sinterbedingungen,

werden dichte, freistehende LCO-LLZO-Kathoden erhalten, die keine durch Nebenreaktionen entstehenden Sekundärphasen aufweisen. Mit Hilfe einer modifizierten festen Polymermembran, die auch in wässriger Lösung hergestellt wird, wird diese Kathode in granatgestützte SSLBs integriert. Die zusammengebauten SSLBs liefern hohe Flächenkapazitäten (> 3 mAh cm^{-2}) und zeigen eine verbesserte Zyklenstabilität (geringerer Kapazitätsabfall) im Vergleich zu anderen Massen-SSLBs mit LCO-LLZO-Kathoden.

In dieser Arbeit wurde über die erste nachhaltig hergestellte LLZO SE berichtet, bei der Wasser und umweltfreundliche Polymere im Foliengießen eingesetzt wurden. Auf dieser Grundlage wurden erfolgreich zwei Arten von SSLBs mit LFP-PEO- bzw. LCO-LLZO-Mischkathoden entwickelt, die zum ersten Mal durch nachhaltige wasserbasierte Prozesse hergestellt wurden. Diese Arbeit zeigte die Machbarkeit eines umweltfreundlichen Verfahrens für SSLBs. Weitere Optimierungen, z.B. zur Erhöhung der Leistungsdichte und der Zyklenstabilität, sind erforderlich, um die besten kommerziellen und ökologischen Vorteile zu erzielen.

Table of Contents

1 Introduction and Objectives

Climate change is one of the most concerned global challenges nowadays. The consumption of fossil fuels with related CO_2 emissions triggers the greenhouse effect causing major environmental problems.[1] Huge efforts have been employed on the energy transition to CO_2-free renewable energy sources like solar or wind for example, but these are inherently intermittent and thus not constant reliable sources of power. Hence, large-scale energy storage systems are needed for the stationary application to stabilize the electric grid and to make the best use of these renewable energies.[2, 3] The state-of-art lithium ion battery (LIB) technology, that has been dominating the market of portable electronic devices and electric vehicles, is now also increasing its share in the stationary storage.[4-9] One main drawback of conventional LIBs is their flammable liquid electrolytes that raise concern regarding safety issues when cells and systems are scaled up. The approach by replacing the liquid electrolytes with the solid ones is one of the alternative solutions to build safer LIBs, known as solid-state lithium batteries (SSLBs). Beside improved safety, they can offer other advantages over conventional batteries such as enhanced energy density and wider operation temperature window.[10, 11]

Commercial and/or laboratorial LIBs and SSLBs are usually evaluated by cost, safety, and performance indicators including specific energy, energy, and power density, and cycle life as well as shelf life, but rarely by their environmental impact, *i.e.* the sustainability.[12] To specify, the sustainability of battery refers to the battery that is manufactured from green materials by sustainable processes. Green materials are less or nontoxic materials with compositions of abundantly available or produced from renewable raw materials, while sustainable processes are devoted to improve carbon footprint in the production.[12] The current processing routes of LIBs and SSLBs mostly involve health-hazard organic solvents, which raise healthy and safety concerns and lead to increasing manufacturing costs due to the need of solvent recovery. Besides, synthetic polymer binders involved are usually produced from fossil fuels, where the ecological footprint should be further reduced. Hence, the development of a green, water-based processing route that can reduce both manufacturing costs and environmental footprints is of great concern of academia and industries.

The garnet-type Li^+-conductor is considered as one promising solid electrolyte material for SSLBs.[13] But the garnets are known undergoing a Li^+/H^+ exchange reaction with moisture,[14] which makes the aqueous processing of this material challenging.

The main goals of this thesis is to design, fabricate and optimize "sustainable" SSLBs. To achieve these aims, following tasks are to be conducted:

- Fabrication of free-standing ceramic Li^+-conducting separators for SSLBs with sustainable receipt comprising water and biopolymers, optimization of the ceramics/binders ratios for tape casting, and achieving the room-temperature ionic conductivity > 0.1 mS cm^{-1} for the ceramic Li^+-conductor separators fabricated in water;
- Investigation on the Li^+/H^+ exchange involved in the aqueous processing of the ceramic Li^+-conductors, and elucidating the underlying reaction mechanisms;
- Water-based processing of ceramic-polymer composite cathodes for SSLBs, identification of the ideal mixing ratios of the ceramic- and polymer-components, evaluation of the influence of this mixing ratio on the battery performance, and achieving stable cycling of SSLBs with coulombic efficiency > 99% and specific capacity > 130 mAh g^{-1} at a current density of 50 µA cm^{-2}, as well as elucidating the possible degradation mechanisms of the SSLBs;
- Water-based processing of ceramic mixed cathodes for SSLBs, optimization of the processing parameters (*e.g.* lamination pressure, sintering atmosphere) for the ceramic mixed cathodes, and achieving a high-capacity SSLB (> 3 mAh cm^{-2}), as well as elucidating the possible degradation mechanisms of the SSLBs.

2 Literature Overview

2.1 Solid-State Lithium Batteries and Solid Electrolytes

2.1.1 Secondary battery technologies

The secondary battery is an electrochemical energy storage device that allows repeatable conversion between electrical and chemical energy. The electrical energy is released from the chemical compounds via electrochemical reactions at the electrodes during discharging, while the electrical energy is converted to chemical energy via the reversed reactions during charging. Hence, the secondary batteries are also known as rechargeable batteries. In contrast, the battery that cannot be recharged after discharging is called primary battery.

A secondary battery consists of one or more electrochemical cells. The fundamental configuration of an electrochemical cell is composed of a positive electrode, a negative electrode, and electrolyte (**Figure 2.1**). The positive electrode has a higher electrode potential than the negative electrode. During discharge, oxidation and reduction occur at the negative and the positive electrode, respectively. Electrons e^- move from the negative electrode to the positive one through the outer circuit, forming an electric current I in the opposite direction. Thus, in the battery society, the positive electrode in batteries is often called cathode, and the negative one anode. During charge, an external voltage source applies electric current to the cell. The electroactive material in the positive electrode is oxidized, and the one in negative electrode is reduced. In both cases of charge and discharge, charge carriers, mostly the ions dissolved in the liquid electrolyte, move inside the cell between the two electrodes to keep them electrically neutralized. In practical batteries, current collectors are often equipped to regulate and distribute the electric current on the electrodes. To reduce the distance between the two electrodes and thus increase the packing density of the batteries, an insulated separator is deployed between the two electrodes to prevent their physical contact, which would cause short circuit. The porous structure of separators allows the infiltration of electrolytes, enabling the transport of charge carriers across separators.

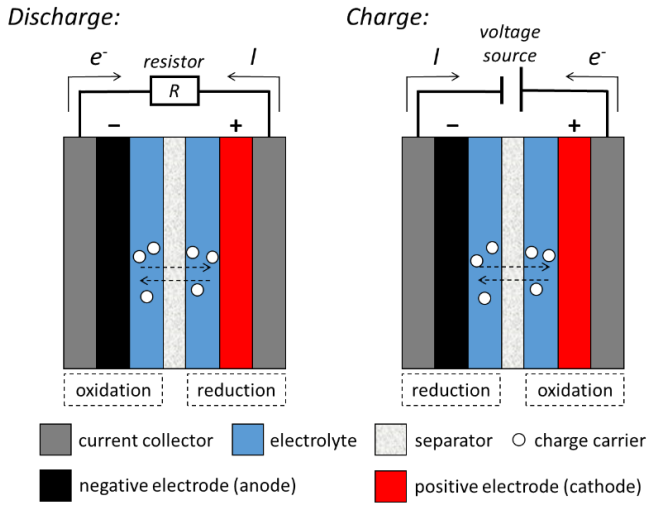

Figure 2.1 Schematic diagram of working principle of an electrochemical cell.

The huge demands on electricity in the electrical age promotes the evolution of the secondary battery technologies (**Figure 2.2**). The most classic technology is lead-acid battery. Since its commercialization in 1890s, it is still widely used in combustion vehicles for starting and lighting, due to the low cost and good reliability.[15] However, the cell chemistry makes the lead-acid battery not suitable for portable electronic devices. Later, the application of nickel cadmium battery (Ni-Cd) in 1960s enables the use of rechargeable batteries in the portable devices. Soon Ni-Cd batteries were substituted by the nickel metal hydride battery (Ni-MH) in 1970s. By replacing the toxic Cd anode with a metal hydride alloy, the Ni-MH battery doubles the energy density comparing to Ni-Cd. A great enhancement in energy density (500 Wh L^{-1} and 200 Wh kg^{-1}) is realized by the LIB technology. Since its debut in 1990s, the state-of-the-art LIB technology becomes one of the most successfully commercialized secondary battery technologies. LIBs power almost all portable electronic devices,[4, 6] electric vehicles,[5] and increase their market share in stationary storage application.[2, 13] Although LIBs exhibit large enhancement in energy density comparing to classic storage systems like lead-acid battery, Ni-Cd and Ni-MH, this present technology is reaching its physicochemical limit (~250 Wh kg^{-1}).[10] Therefore, it is urgent to

develop next-generation technologies with higher energy density, such as SSLBs, Li-sulfur batteries (Li-S), and Li-air batteries.

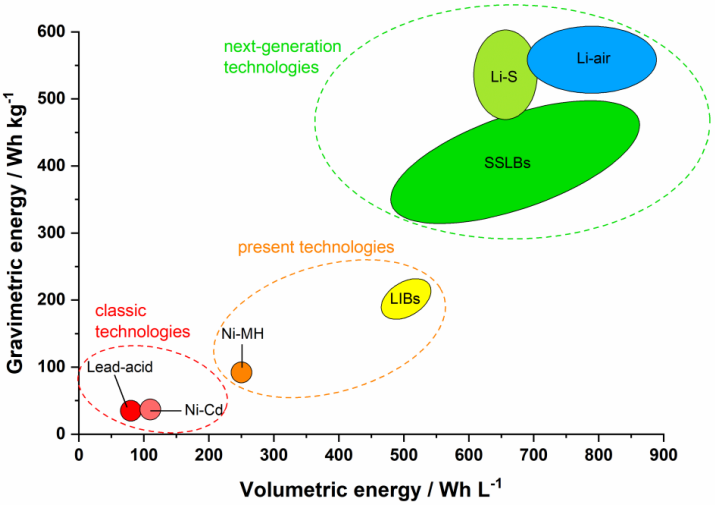

Figure 2.2 Overview of the evolution of secondary battery technologies.[16]

2.1.2 Li-ion batteries and solid-state lithium batteries

The cell chemistry of SSLBs is highly similar to the state-of-the-art LIBs, especially regarding the cathode part. The cathode active materials (CAMs) used in current LIBs can be also adopted in SSLBs. There are mainly three classes of intercalation cathode materials commercialized for LIBs.[17, 18] The first one is the layered structure represented by $LiCoO_2$ (LCO), $LiNi_xCo_yAl_{1-x-y}O_2$ (NCA) and $LiNi_xMn_yCo_{1-x-y}O_2$ (NMC).[19] The elements Ni, Al and Mn were substituted into the LCO structure in order to increase capacity and voltage, improve thermal stability, and enhance the structural cycling stability, respectively.[20] The second structure of cathode material is the spinel-type $LiMn_2O_4$ (LMO), which has a higher voltage than LCO but less capacity.[21] The last one is the olivine-structured $LiFePO_4$ (LFP). The LFP-based LIBs possess long cycle life and shelf life due to the high structural stability of the polyanionic phosphate-network.[22, 23] It shows lower

voltage but higher practical capacity and cycling stability than LCO.[24] Meanwhile, LFP has been demonstrated compatible with the water-based cathode electrode processing for conventional LIBs.[25-36] The electrochemical properties of LFP can tolerate the slight degradations due to the contact with aqueous media.[37-41]

On the anode side, graphite is commonly used material for LIBs.[42] The potential of the lithiated graphite LiC_6 is 0.25-0.01 V *vs.* Li/Li^+, but it could also cause lithium deposition at the electrode surface during fast charging.[43] Alternative materials such as Si[44], Sn[45], SnO_2[46], $Li_4Ti_5O_{12}$[47] for high capacity, and TiO_2[48] for high-rate and long-life operation have been investigated. The highest theoretical capacity would be achieved by directly employing Li metal as the anode material, which is desired to be applied in SSLBs.

The electrolyte is a key factor for the operation of LIBs. The common liquid electrolyte solution consists of binary solvent mixture and lithium salt. This solvent mixture contains high dielectric ethylene carbonate (EC) and either dimethyl carbonate (DMC), ethyl methyl carbonate (EMC) or diethyl carbonate (DEC) with low viscosity. The lithium salt can be lithium perchlorate ($LiClO_4$), lithium hexafluorophosphate ($LiPF_6$) or lithium bis(trifluoromethanesulfonyl)imide (LiTFSI). Although the organic liquid electrolyte provides high conductivity, it has a fatal flaw - the safety issue due to its flammability.[6] Hence, academics and industries are intensively developing new electrolyte systems, including aqueous systems, ionic liquids, inorganic solids, and polymers. The latter two as well as their combination belong to solid electrolytes.

SSLBs that use solid electrolytes (SEs) instead of liquid ones are becoming a promising solution for safer batteries.[10, 11] In SSLBs, SEs not only sustain Li^+-conduction but also acts as the battery separator.[11] As shown in **Figure 2.3a**, though the SEs have higher density than the liquid electrolytes and common separators used in conventional LIBs, SSLBs can still gain increased volumetric as well as gravimetric energy density by replacing the thick graphite anode with thin light lithium metal anode.[10]

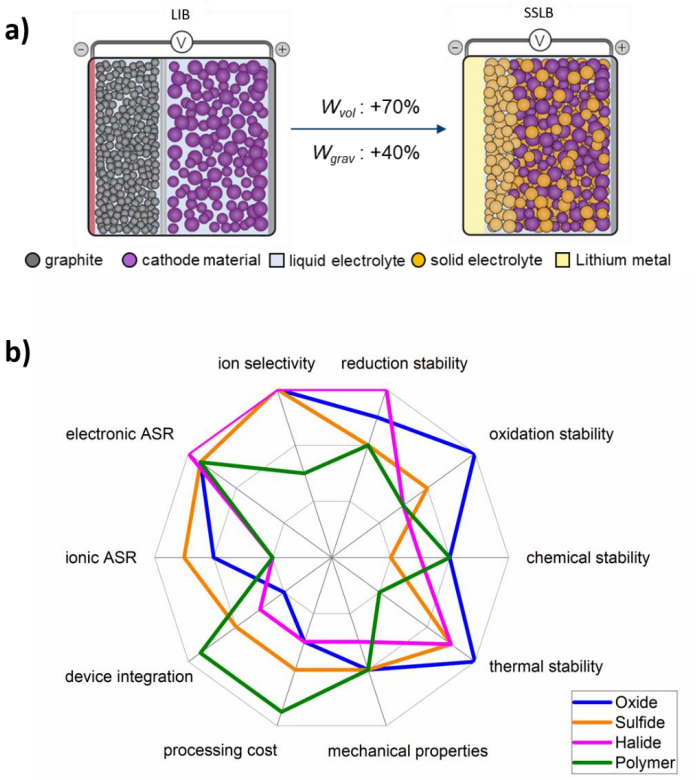

Figure 2.3 a) Comparison of a conventional LIB and a SSLB with the aspect of volumetric (W_{vol}) and gravimetric energy density (W_{grav}). (Reproduced from ref. [10] with permission); b) Performance of different solid electrolyte materials.[11]

2.1.3 Solid electrolytes

A suitable Li^+-conducting electrolyte need to fulfill following properties:[49] 1) high Li^+ conductivity at the operating temperature; 2) negligible electronic conductivity over the entire applied temperature; 3) negligibly small or no grain-boundary ionic resistance; 4) no chemical reactions with both electrodes, especially with Li-metal or Li-alloy; 5) high electrochemical decomposition voltage; 6) environmental benign, low cost and ease of preparation. As shown in **Figure 2.3b**, four main kinds of materials, namely oxides, sulfides, halides, and polymers, are compared regarding their stabilities, electrochemical properties, and practical feasibility.

Oxides. Four types of Li-conducting oxides materials have been developed for SSLBs: perovskite-type, NASICON-type, LISICON-type and garnet-type. Perovskite-type solid electrolyte (*e.g.* $Li_{3x}La_{2/3-x}TiO_3$) exhibits high Li-conductivity (~10^{-5} S cm^{-1}) at room temperature.[50] However, the reduction of Ti^{4+}, when contacted with Li metal, makes this material not suitable for lithium battery application. The term "NASICON" refers to sodium superionic conductor, and materials with the formula $NaM(PO_4)_3$ (M=Ge, Zr, or Ti) were initially developed for sodium ion conduction. By replacing sodium with lithium, the $LiTi_2(PO_4)_3$ system has been widely investigated for Li-conduction and the ionic conductivity can be further improved (~10^{-3} S cm^{-1}) by Al substitution to form $Li_{1+x}Al_xTi_{2-x}(PO_4)_3$ (LATP).[51] But NASICON-type material is also incompatible with lithium metal due to the reduction of Ti^{4+}. $Li_{14}Zn(GeO_4)_4$ is the first material to be given the name lithium superionic conductor (LISICON).[52] Although the LISICON-type materials exhibit room temperature ionic conductivity with 10^{-7}-10^{-5} S cm^{-1}, they are unfortunately highly reactive with lithium metal and atmospheric CO_2.[53] Garnet-type materials have both high ionic conductivity and high chemical stability. The representative substance $Li_7La_3Zr_2O_{12}$ (LLZO)[54] exhibits high Li-conductivity (10^{-5}-10^{-3} S cm^{-1}) at room temperature, and it is found to be the only Li-conducting oxide material that is chemically stable against lithium metal. Owing to their brittle nature, the processing and the integration of oxide solid electrolytes into devices remain challenging, especially when the thickness of them has to be reduced.

Sulfides. Li-conducting sulfides are also called as thio-LISICON, which are developed based on the Li_2S-SiS_2 system.[55] Despite much effort to improve the conductivity (10^{-7}-10^{-3} S cm^{-1}), the drawbacks such as poor chemical stability in moisture and poor compatibility to the cathode materials limit its large-scale production and application.[56]

Halides. Besides the lithium halides used in the $LiBH_4$-LiX system, lithium metal halides have been studied over decades. A representative one is Li_2ZnCl_4[57] with spinel structure, which obtains Li-conductivity accompanied with structural transition at high temperature. Recently, a new type of Li-conducting halides so-called "anti-perovskite" (*e.g.* Li_3OCl[58]) is introduced, which exhibits high ionic conductivity (~10^{-3} S cm^{-1}) at room temperature. The drawbacks of halide materials are the sensitivity to moisture, poor reduction stability, and low oxidation voltage.[59]

Polymers. Solid polymer electrolytes (SPEs) are the solid solutions of lithium salts (*e.g.* LiTFSI, $LiClO_4$) in polymers. The most used polymer host is poly(ethylene oxide) (PEO).[60] The conventional solid polymer electrolytes suffer from low conductivity at room temperature and poor thermal stability, but they are suitable for large-scale processing, and easy to be integrated into cells.[61]

2.2 Garnet-Type Solid Electrolyte

This section is based with modification on the publication 'A Review on Li^+/H^+ Exchange in Garnet Solid Electrolytes: From Instability against Humidity to Sustainable Processing in Water' by Ye et al. It was published during the thesis and reprinted (adapted) with permission from [14].

2.2.1 Garnet Li^+ conductors

The first Li^+ conductor of the garnet family was reported by Thangadurai *et al*. in 2003 as $Li_5La_3Ta_2O_{12}$ with a bulk conductivity around 10^{-6} S cm^{-1} at 25 ˚C.[62] Later, they showed an improved Li^+ conductivity of $4x10^{-5}$ S cm^{-1} at 22 ˚C for $Li_6BaLa_2Ta_2O_{12}$.[63] In 2007, Murugan *et al.* achieved an important breakthrough with the Li-stuffed garnet $Li_7La_3Zr_2O_{12}$ (LLZO), that led to an enhancement in bulk conductivity by one order of magnitude to $3x10^{-4}$ S cm^{-1} at 25 ˚C.[54] Since then, the Li^+ conductivity of LLZO was further increased to 10^{-3} S cm^{-1} by introducing various dopants and substitutions like Al, Ta, Ga, and Nb.[64-66]

Two stable crystal structures exist for LLZO: a cubic phase with the space group (SG) *Ia-3d* and a tetragonal phase with the space group $I4_1/acd$. The cubic LLZO has a Li^+ conductivity two orders of magnitude higher than that of tetragonal form.[13, 49] **Figure 2.4a** shows the crystal structure of cubic LLZO that consists of 8-fold coordinated LaO_8 dodecahedra, 6-fold coordinated ZrO_6 octahedral and Li ions partially occupying the interstitial sites. Based on neutron diffraction studies, the Li ions in cubic LLZO possess three different interstitial sites, namely i) tetrahedral (24*d*), ii) octahedral (48*g*), and iii) off-centered octahedral (96*h*). As shown in **Figure 2.4b**, the 24*d* tetrahedral and the 48*g*/96*h* octahedral share the faces to each other forming a Li^+ pathway so that fast Li^+ conduction is achieved in cubic LLZO. The 24*d* Li ions trapped in the tetrahedral site

are immobile, whereas the Li ions on the 96*h site*, which are slightly off the 48*g* sites, are most anisotropic showing higher mobility.[65]

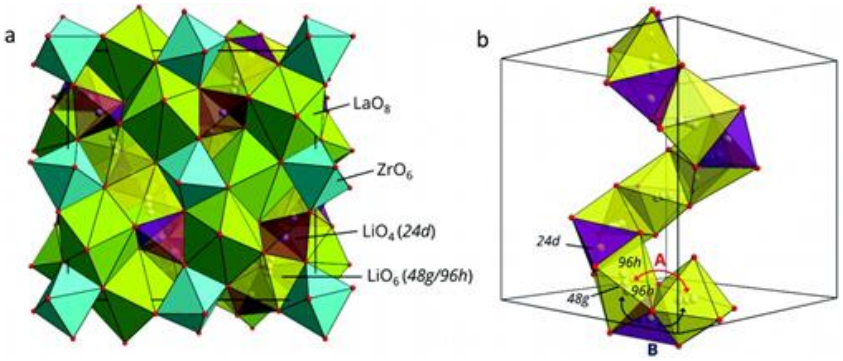

Figure 2.4 a) Crystal structure of cubic $Li_7La_3Zr_2O_{12}$; b) Wyckoff positions of Li ions and two potential Li^+ migration pathways A (preferred in $Li_5La_3M_2O_{12}$) and B (preferred in $Li_7La_3Zr_2O_{12}$). (Reprinted from ref. [65] with permission)

2.2.2 Li^+/H^+ chemistry in garnets

Although LLZO was assumed to be chemically stable in air so that the storage and processing of LLZO in ambient conditions is feasible, several researches reported the formation of a lithiophobic Li_2CO_3 layer on the LLZO pellet surface after exposure to air for a period of time, which is detrimental for the electrochemical performance of the material, *e.g.* large Li/garnet interfacial resistance due to the poor Li wettability of surface impurities.[67-72] A widely accepted explanation to the degradation of LLZO in humidity is a two-step reaction route including the Li^+/H^+ exchange (LHX)[14] between LLZO and moisture in air (**Equation 2.1**) and the subsequent formation of Li_2CO_3 from the as-formed LiOH (**Equation 2.2**):

$$Li_7La_3Zr_2O_{12} + xH_2O \longrightarrow Li_{7-x}H_xLa_3Zr_2O_{12} + xLiOH \quad \text{(Equation 2.1)}$$

$$2LiOH + CO_2 \longrightarrow Li_2CO_3 + H_2O \quad \text{(Equation 2.2)}$$

Besides, the $LiOH{\cdot}H_2O$ formed from the LiOH can be a necessary intermediate prior to or simultaneously with the reaction with CO_2 to form Li_2CO_3.[73]

Since the LHX is the key step in the degradation of LLZO in humidity, many investigations regarding LHX were carried out on various garnets [*i.e.* $Li_5La_3M_2O_{12}$ (M=Ta, Nb)[74-78], $Li_6MLa_2Nb_2O_{12}$ (M=Ca, Ba)[79, 80] and $Li_7La_3Zr_2O_{12}$ with different substitutions (*e.g.* Al, Ta, Nb)[81-85]] in aqueous solutions or organic acids. In most cases, severe Li losses in garnets along with a pH increase of the aqueous solutions were observed, indicating the LHX according to **Equation 2.1**.

So far, the general LHX mechanism for garnets is not yet clarified due to the complications introduced by the replacement of Li ions with protons, which is highly dependent on the garnet composition and substitution content. Ma *et al.* proposed an LHX mechanism for polycrystalline cubic $Li_7La_3Zr_2O_{12}$ powder in water at room temperature.[84] The LHX preferentially occurs at the most anisotropic Li site, 96*h*, leaving both 48*g* and 24*d* sites largely unaffected. With the depletion of Li^+ on the 96*h* site, the 48*g* site might be further dominant in the exchange, but no LHX takes place at the 24*d* site. As a result, the final product of the water treatment has its 24*d* sites occupied by Li ions, 48*g* sites occupied by Li ions and protons, and 96*h* sites solely occupied by protons. This is consistent with the observation by Li *et al.* on $Li_{6.5}La_3Zr_{1.5}Ta_{0.5}O_{12}$ that the Li-ion occupancy of the 24*d* sites is the same before and after LHX, whereas those of 48*g* and 96*h* sites are reduced after LHX.[86] Liu *et al.*[82] and Hiebl *et al.*[87] supported this explanation, based on the investigation on $Li_{6.75}La_3Nb_{0.25}Zr_{1.75}O_{12}$ and single-crystal Al-substituted LLZO, respectively. It has also been found that the crystal structure of LLZO maintains centric *Ia-3d* during the LHX process but with a minor lattice expansion due to the replacement of strong Li–O bonds with the weaker O–H···O bonds.[84, 88] Modelling suggests this lattice expansion has a linear correlation versus the retained Li content in LLZO.[89]

In contrast, Truong *et al.* found that Li ions at the tetrahedral sites in $Li_{5+x}Ba_xLa_{3-x}Nb_2O_{12}$ favor the LHX while octahedral-site ions are rather stable.[90] Similarly, Nyman *et al.* suggested that Li ions in the tightly bound, immobile sites in $Li_5La_3Ta_2O_{12}$ are replaced by protons.[74] Recently, Redhammer *et al.* also found that LHX occurs preferably at the 24*d* sites in single-crystal $Li_6La_3ZrTaO_{12}$.[91] It could be attributed to the small displacement of Li^+ away from 24*d* to a general 96*h* position due to the Ta-substitution, which leads to an enhanced mobility of Li^+ at 24*d* sites. This displacement does not alter the garnet *Ia-3d* structure at 27 ˚C. In the case of the LHX taking place at 90 ˚C, a symmetry reduction from *Ia-3d* to non-centrosymmetric *I-43d* is observed

and the preferable LHX occurs at the 48*e* site (equivalent to the 96*h* site). However, Liu *et al.* addressed that this phase transition can take place even at room temperature for $Li_{6.25}Al_{0.25}La_3Zr_2O_{12}$ with an intensive exchange (> 75%).[92] Galven *et al.* reported a similar observation when $Li_6CaLa_2Nb_2O_{12}$ was treated in refluxed acetic acid.[79] In addition, there have been another two symmetries reported for protonated $Li_5La_3Nb_2O_{12}$, namely the non-centric cubic $I2_13$ and the orthorhombic $P2_12_12_1$.[75, 93] These symmetry changes as well as the structural disorders are generally induced by the change of site occupation and atomic interaction between Li, H and O ions.

The phase transition from tetragonal to cubic induced by LHX has been firstly observed by Galven *et al.* for the tetragonal $Li_7La_3Sn_2O_{12}$ with SG $I4_1/acd$ which turned into cubic $Li_{2.25}H_{4.75}La_3Sn_2O_{12}$ with SG *Ia-3d* after a treatment in refluxed benzoic acid/ethanol solution.[83] The correspondence between the Li^+ sites in the two structures was described as following (**Figure 2.5a**): i) the 24*d* site in the cubic phase are derived from 8*a* (fully occupied by Li^+) and 16*e* (vacancies) sites of the tetragonal one; ii) the 48*g* site of cubic phase originates from 32*g* and 16*f* (both occupied by Li^+) in the tetragonal phase; iii) the 96*h* sites in cubic phase are the former empty 32*g* sites in the tetragonal one. Later, the same phase transition in LLZO triggered by humidity in air was observed as well. According to Larraz *et al.*, the phase transition caused by protonation is irreversible upon heating above 650 ˚C,[94] while the cubic phase without LHX is formed solely by reaching the tetragonal→cubic phase transition temperature for LLZO (625-645 ˚C) and returns to tetragonal phase after cooling (**Figure 2.5b**).[95] Moreover, Orera *et al.* claimed that a non-centrosymmetric *I-43d* cubic phase is obtained below 150 ˚C after the protonation of tetragonal LLZO, while annealing above 300 ˚C results in a centric *Ia-3d* cubic phase with lower H^+ content.[85] Overall, these findings suggest that H^+ can act as a dopant to stabilize the cubic structure of LLZO. This cubic garnet structure stabilized by H^+ is usually called *low-temperature (LT) cubic garnet structure*.[96, 97] In contrast, the cubic phase without LHX is called *high-temperature (HT) cubic garnet*.

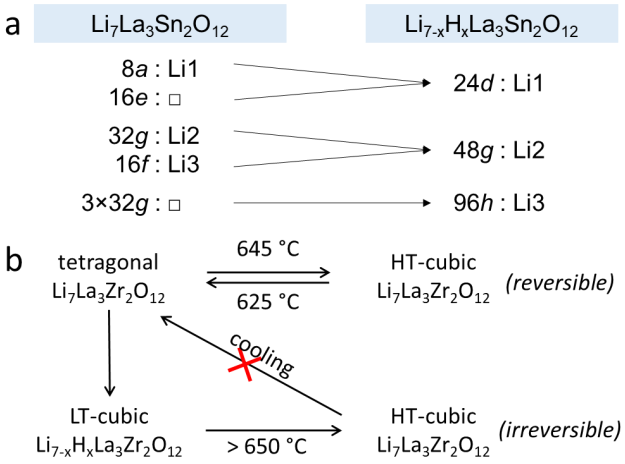

Figure 2.5 a) Correspondence between the Li sites in the two garnet structures: tetragonal $Li_7La_3Sn_2O_{12}$ and cubic $Li_{7-x}H_xLa_3Sn_2O_{12}$. (Reproduced from Ref. [83] with permission.) b) Phase transition between tetragonal, LT- and HT-cubic $Li_7La_3Zr_2O_{12}$.

Figure 2.6a presents the tendency of Li loss in garnets upon the duration of LHX in water or acids based on 7 references[80-85, 98]. It is a challenge selecting the most water-stable garnets, because the Li losses of the garnets even with the same composition vary among different reports. This might be attributed to different test conditions and characterization methods. But it is revealed from **Figure 2.6a** that powders, due to larger surface area, usually show higher LHX than pellets. Depth profile analyses of garnet samples exposure to humid air revealed that the Li_2CO_3 and LiOH with a gradient distribution were only detected in the first 400 nm of the samples (**Figure 2.6b**).[68, 99] The LHX is usually assumed to be fast in the very beginning at the surface of garnets towards water, which leads to an H^+-enriched garnet surface layer. This surface layer consequently hinders the further reaction of water with the interior positions in the garnet and can thus be considered somewhat self-limiting. A study on LHX behavior of polycrystalline $Li_6La_3ZrTaO_{12}$ powder in different surroundings (**Figure 2.6c**) revealed that the exchange rates in all conditions are similar (0.9-1.8x10^{-19} mol s^{-1}) except for the one in warm water at 90 °C (4.6x10^{-19} mol s^{-1}), which results in a much higher estimated H^+ equilibrium concentration than others. Hence, it is believed that the reaction kinetics is more limited by the temperature-

dependent proton diffusion inside garnets rather than by the H^+ concentration in aqueous/acid media.[91] Hiebl *et al.* determined the H^+ diffusion coefficient as 2×10^{-17} m^2 s^{-1} in a protonated Al-doped LLZO.[87]

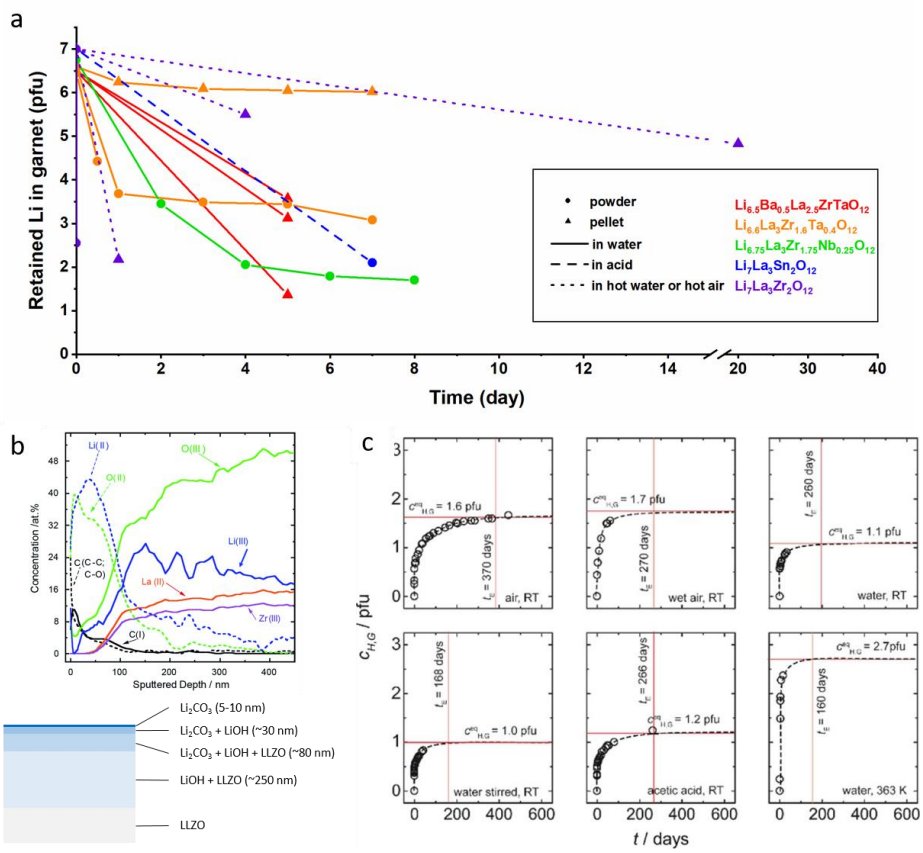

Figure 2.6 a).Retained Li content in garnet after aqueous or acid treatments. b) Depth profile for the concentration of Li, C, O, Zr, and La from the X-ray photoelectron spectroscopy analysis of garnet after preparation in ambient air and a corresponding schematic depicting the contamination layers. (Reprinted from ref. [68] with permission). c) Concentration profiles for garnet powder, fitted exponentially to estimate qualitatively the H^+ equilibrium concentration $c_{H,G}^{(eq)}$. (Reprinted from ref. [91] with permission).

Several reports, as summarized in **Table 2.1**, have shown the phenomenon of reverse LHX in garnets *i.e.* Li^+ reenter the protonated garnets to replace H^+. If the chemical formula (**Equation 2.1**) is written in ionized chemical balance, we obtain **Equation 2.3**:

$$Li_7La_3Zr_2O_{12} + xH_2O \leftrightarrow Li_{7-x}H_xLa_3Zr_2O_{12} + xLi^+ + xOH^- \quad \text{(Equation 2.3)}$$

In order to shift the equilibrium to the left side, we can, according to the principle of Le Chatelier, either remove water from the system or increase the concentration of Li^+ and/or OH^-, *e.g.* by adding Li salts and/or alkali.

Table 2.1 Investigations on reverse Li^+/H^+ exchange of garnets

Entry	Protonated garnets	Condition[a]	Composition after reverse LHX
1	$Li_{0.56}H_{4.44}La_3Nb_2O_{12}$[20]	5 M $LiNO_3$, RT, 4 days	"$Li_5La_3Nb_2O_{12}$"
2	$Li_3H_{2.5}Ba_{0.5}La_{2.5}Nb_2O_{12}$[20]	5 M $LiNO_3$, RT, 4 days	"$Li_{5.5}Ba_{0.5}La_{2.5}Nb_2O_{12}$"
3	$Li_{4.8}H_{1.2}BaLa_2Nb_2O_{12}$[20]	5 M $LiNO_3$, RT, 4 days	"$Li_6BaLa_2Nb_2O_{12}$"
4	$Li_{1.70}H_{5.05}La_3Zr_{1.75}Nb_{0.25}O_{12}$[15c]	5 M $LiNO_3$, 25 ˚C, 4 days	$Li_{1.73}H_{5.02}La_3Zr_{1.75}Nb_{0.25}O_{12}$
5		5 M $LiNO_3$, 60 ˚C, 24 h	$Li_{1.90}H_{4.85}La_3Zr_{1.75}Nb_{0.25}O_{12}$
6		5 M $LiNO_3$, 60 ˚C (ht), 24 h	$Li_{1.91}H_{4.84}La_3Zr_{1.75}Nb_{0.25}O_{12}$
7		sat. LiOH, 60 ˚C (ht), 24 h	$Li_{2.98}H_{3.77}La_3Zr_{1.75}Nb_{0.25}O_{12}$
8	$Li_{2.55}H_{4.45}La_3Zr_2O_{12}$[15e]	2 M LiOH, RT, 15 min	$Li_{4.15}H_{2.85}La_3Zr_2O_{12}$
9	$Li_{3.08}H_{3.52}La_3Zr_2Ta_{0.4}O_{12}$[15b]	1 M LiOH, RT	$Li_{5.36}H_{1.24}La_3Zr_2Ta_{0.4}O_{12}$
10	$Li_{3.44}H_{3.16}La_3Zr_2Ta_{0.4}O_{12}$[15b]	1 M LiOH, RT	$Li_{5.54}H_{1.06}La_3Zr_2Ta_{0.4}O_{12}$
11	$Li_{3.49}H_{3.11}La_3Zr_2Ta_{0.4}O_{12}$[15b]	1 M LiOH, RT	$Li_{5.64}H_{0.96}La_3Zr_2Ta_{0.4}O_{12}$
12	$Li_{3.68}H_{2.92}La_3Zr_2Ta_{0.4}O_{12}$[15b]	1 M LiOH, RT	$Li_{6.04}H_{0.56}La_3Zr_2Ta_{0.4}O_{12}$
13	$Li_{6.53}H_{0.07}La_3Zr_2Ta_{0.4}O_{12}$[15b]	1 M LiOH, RT	$Li_{6.53}H_{0.07}La_3Zr_2Ta_{0.4}O_{12}$
14	$Li_{6.86}H_{0.14}La_3Zr_2O_{12}$[24]	Surface Li_2CO_3, 700 ˚C, 15 min	$Li_7La_3Zr_2O_{12}$
15	$Li_{5.4}H_{1.0}La_3Zr_{1.4}Nb_{0.6}O_{12}$[28]	$LiNO_3$+LiOH powder, 400 °C, 98 MPa, 6 h	$Li_{6.4}La_3Zr_{1.4}Nb_{0.6}O_{12}$

Concentrated Li salt and/or base aqueous solutions, *e.g.* LiCl and LiOH solutions (> 1 M), have been proven to sufficiently suppress the occurrence of LHX for pristine garnets (*e.g.* Entry 13 in **Table 2.1**).[77, 80, 81, 100-102] The high chemical potential of Li^+ and/or OH^- in the aqueous media pushes the chemical balance (**Equation 2.3**) towards the left side, meaning that the LHX is hardly happening. However, to my knowledge, a complete reverse exchange of already protonated garnets has not been achieved in aqueous solutions yet. This might be related to the energy barrier of the replacement of H^+ by Li^+, as the protonated garnet phase is the thermodynamically favored form.[103] The closest attempt to completion was performed by Truong *et al* (Entry 1 in **Table 2.1**).[90] The reverse-ion-exchanged $Li_5La_3Nb_2O_{12}$ has a cell constant of *a*=12.789(3) Å, which is only slightly larger than the pristine one (12.775(2) Å), and no significant weight loss (only ~0.5%) between 300 and 500 °C was observed, indicating only limited decomposition due to H-substitution.

On the other hand, a complete reverse LHX can be accomplished by thermal treatment with the presence of additional Li sources.[104] Larraz *et al.* proposed this thermal evolution of LLZO from its protonated form as following steps:[94]

$$400\text{-}450\ ^\circ C:\ Li_{7-x}H_xLa_3Zr_2O_{12} \longrightarrow Li_{7-x}La_3Zr_2O_{12-x/2} + x/2\ H_2O \qquad \text{(Equation 2.4)}$$

$$650\text{-}700\ ^\circ C:\ Li_{7-x}La_3Zr_2O_{12-x/2} + x/2\ Li_2CO_3 \longrightarrow Li_7La_3Zr_2O_{12} + x/2\ CO_2\uparrow \qquad \text{(Equation 2.5)}$$

With the help of an *in-situ* synchrotron-based high-energy X-ray diffraction technique (HEXRD) (**Figure 2.7**) Cai *et al.* recently suggested that the stoichiometric restoration of LLZO can be completed at higher temperatures (730-950 °C) due to the increased melting point of the eutectic solution of LiOH and Li_2CO_3, thereby impeding the reverse LHX.[105] In this process the stoichiometric LLZO is formed via the reaction of Li_2CO_3 with the intermediate $La_2Zr_2O_7$, which is the decomposition product of protonated LLZO by heating.

Alternatively, a combination of $LiNO_3$ and LiOH, enables the Li recovery at lower temperature, due to their lower melting points than Li_2CO_3, resulting in the overall reaction:[106]

$$400\ ^\circ C:\ Li_{6.4-x}H_xLa_3Zr_{1.4}Nb_{0.6}O_{12} + x/2\ LiNO_3 + x/2\ LiOH \longrightarrow Li_{6.4}La_3Zr_{1.4}Nb_{0.6}O_{12} + x/2\ NO_2\uparrow + H_2O\uparrow$$

(Equation 2.6)

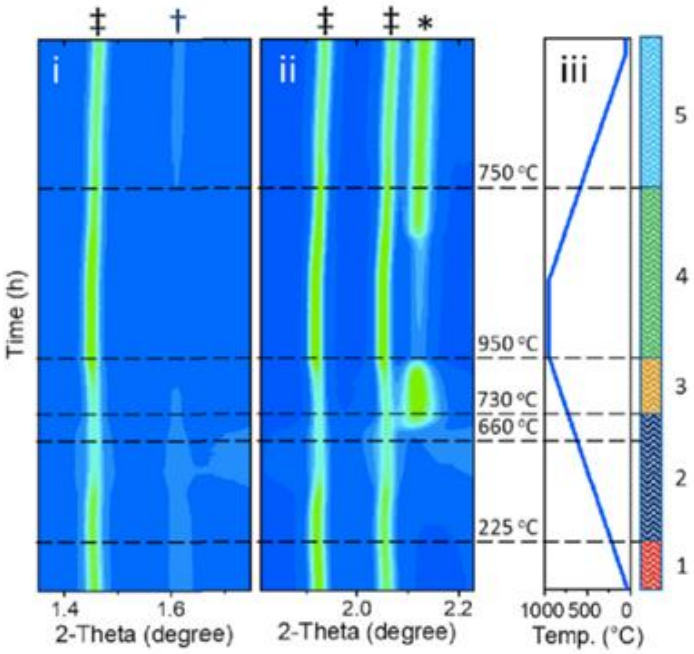

Figure 2.7 High-temperature *in-situ* HEXRD phase evolutions of LLZO. The "‡", "*" and "†" symbols stand for LLZO, $La_2Zr_2O_7$ and Li_2CO_3, respectively. (Reprinted from ref. [105] with permission.)

2.3 Processing of Garnets

This section is partially based with modification on the publications 'A Review on Li^+/H^+ Exchange in Garnet Solid Electrolytes: From Instability against Humidity to Sustainable Processing in Water' by Ye et al. and 'Water-based fabrication of garnet-based solid electrolyte separators for solid-state lithium batteries' by Ye et al. They were published during the thesis and reprinted (adapted) with permission from [14] and [98].

2.3.1 Tape-casting

Commonly, garnet-based separators are fabricated by slicing sintered bulk pellets. Calcined garnet powder is pressed into pellets, followed by either free sintering or advanced sintering techniques such as field assisted sintering,[107] isostatic hot pressing,[108] and flash

sintering.[109] The size of the prepared separators is therefore restricted by the pressing molds. Moreover, slicing by diamond saw often results in separators with thicknesses over 500 µm, which cannot fulfill the expectation of thin separators in battery cells. When the pellets are up-scaled, slicing could also lead to mechanical failure of the cut-off sheets. Hence, it is challenging to fabricate thin, large garnet-based components by a bulk process.

Table 2.2 Examples of fabrication of garnet solid electrolytes by tape-casting

Powder	Solvent	Dispersant	Binder	Plasticizer	Thickness [µm]	Sintering Parameters	Ionic Conductivity [mS cm^{-1}]	Ref.
$Li_{6.25}La_3Al_{0.25}Zr_2O_{12}$	Ethanol Acetone	PAA	PVB	BBP	28	1080 °C, 1 h, N_2 800 °C, 1-4 h, O_2	0.2 (r.t.)	[110]
$Li_{6.25}La_3Ga_{0.25}Zr_2O_{12}$	Ethanol Acetone	PAA	PVB	BBP	25	1130 °C, 0.3 h, N_2 800 °C, 1-4 h, O_2	1.3 (r.t.)	[111]
$Li_7La_{2.75}Ca_{0.25}Zr_{1.75}Nb_{0.25}O_{12}$	Toluene IPA	Fish oil	PVB	BBP	35 (dense) 70 (porous)	700 °C, 4 h, air 1100 °C, 6 h, air	0.22 (22°C)	[112, 113]
$Li_{6.75}La_{2.75}Ca_{0.25}Zr_{1.5}Nb_{0.5}O_{12}$	Toluene IPA	Fish oil	PVB	BBP	14 (dense) 70 (porous)	1050 °C, 1 h, air	n.a.	[114]
$Li_7La_3Al_{0.1}Zr_{1.75}Nb_{0.25}O_{12}$ Li_3BO_3	Toluene Ethanol	Fish oil	EC	PEG DBP	150-175	650 °C, 1 h, air 1000 °C, 6 h, Ar	0.283 (r.t.)	[115]
$Li_{6.16}La_3Al_{0.28}Zr_2O_{12}$ ZnO	Ethanol Xylene Toluene	Fish oil	PVB	PEG BBP	500	600 °C, 1 h, air 1250 °C, 5 h, air	0.08 (25°C)	[116]
$Li_7La_3Zr_2O_{12}$ Al_2O_3	THF, IPA Butanol	Rhodaline	PVA PVB	n.a.	80-100	900 °C, 6 h, air 1200 °C, 6 h, Ar/H_2	0.1 (22°C)	[117]
$Li_{6.4}La_3Zr_{1.4}Ta_{0.6}O_{12}$ Li_2O	Ethanol BuAcO	none	PAR	MB	200	650 °C, 1 h, air 1100 °C, 6 h, air	0.52 (30°C)	[118]
$Li_{6.5}La_{2.8}Ga_{0.2}Zr_{1.75}Nb_{0.25}O_{12}$	Water	none	WB04B -53	none	90 (green)	800 °C, 2 h, air 1040 °C, 2 h, Ar	0.5 (r.t.)	[119]
$Li_{6.5}La_3Zr_{1.5}Ta_{0.5}O_{12}$	Water	none	WB4101		n.a.	800 °C, 2 h, air 1140 °C, 2 h, Ar	0.32 (r.t.)	[119]

IPA: isopropanol; THF: tetrahydrofuran; BuAcO: butyl acetate; PAA: polyacrylic acid; PVB: polyvinyl butyral; PVA: polyvinyl acetate; EC: ethyl cellulose; PAR: polyacrylic resin; BBP: benzyl butyl phthalate; DBP: dibutyl phthalate; PEG: polyethylene glycol; MB: methyl benzoate; r.t.: room temperature; n.a.: not available

Free-standing ceramic thin sheets can be produced by tape-casting. Recently, several researchers have reported applying this technique for the fabrication of garnet thin layers (**Table 2.2**). Yi *et*.

al.[110, 111] successfully fabricated ultrathin layers with a thickness less than 30 µm from Ga- and Al-doped garnet nanopowders. Wachsman and co-workers made great efforts in fabrication of not only dense but also porous garnet layers.[112-114] Several studies reported the using of additional sintering additives, *e.g.* Li_3BO_3,[115] ZnO,[116] Al_2O_3,[117] Li_2O,[118] to achieve higher density of the garnet tapes, which, however, can lead to the reduction of their electrochemical performances. Furthermore, the tape-casting slurries in all these works used organic solvents, raising health and safety concerns and increasing the manufacturing costs due to the need of solvent recovery. Hence, the development of a green, water-based processing route that can reduce both manufacturing costs and environmental footprint are of concern. Since garnet is known to be sensitive to water,[120] there are few reports on water-based processing of garnet till now. To my knowledge, there are only two demonstrated examples in literature reporting the aqueous tape-casting[119] and an aqueous-based gelcasting process of garnets.[121] The reported aqueous tape-cast garnet was found to partially decompose during sintering in air forming Zr-containing secondary phases, which lowered the ionic conductivity by factor of two. The gel-cast SE, on the other hand, is much thicker (1 mm) than tape-cast ones (**Table 2.2**) and would thus decrease the energy density on cell level.

2.3.2 Solvent selection

Prior to the shaping step (*e.g.* pressing, tape-casting), garnet powders are usually ball-milled in solvents to reduce the particle size for an enhanced sinterability. The LHX of garnets was also observed in several common organic solvents, which was shown by the change of the lattice parameter in $Li_{6.25}Al_{0.25}La_3Zr_2O_{12}$ after immersion (**Figure 2.8**).[89] Especially, primary alcohols *e.g.* ethanol, methanol and 1-propanol have significant LHX rates due to the higher acidity and reactivity of the hydroxyl group:

$$Li_7La_3Zr_2O_{12} + x\ R\text{-}OH \rightarrow Li_{7-x}H_xLa_3Zr_2O_{12} + x\ R\text{-}OLi \qquad \text{(Equation 2.7)}$$

2-propanol is a special case, where less LHX occurred due to the weaker acidic character of the secondary alcohol attributed to a possible steric hindrance.[89] In comparison, aprotic solvents without proton-giving functional groups *e.g.* cyclohexane and acetonitrile react much less with garnets. Therefore, aprotic solvents are recommended for wet processing of garnets to prevent

LHX. Another study on solvent-assisted ball-milling showed that acetonitrile successfully limits the Li loss of $Li_{6.4}La_3Zr_{1.4}Ta_{0.6}O_{12}$ to a mere 4%, whereas the powder milled in ethanol showed a Li loss of approximately 30%.[122]

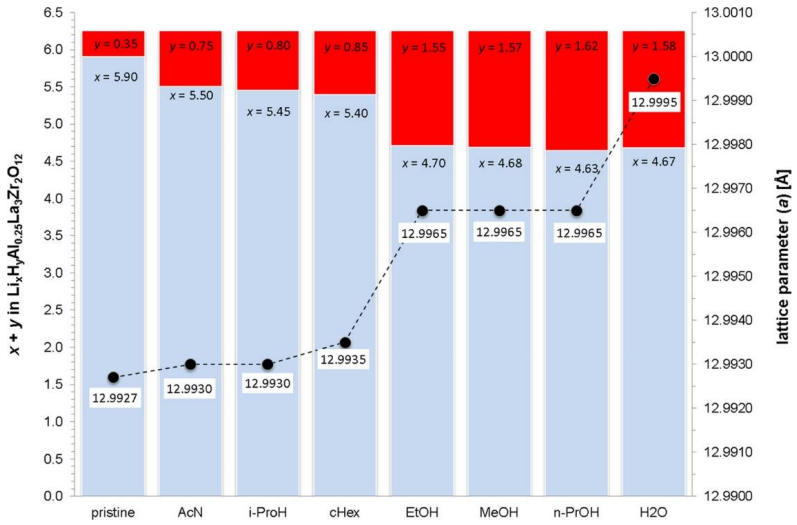

Figure 2.8 Residual Li stoichiometry and lattice parameter of garnet $Li_{6.25}Al_{0.25}La_3Zr_2O_{12}$ powder after immersion in solvents. (Reprinted from ref. [89] with permission.)

However, in large-scale powder production, organic solvents usually cause safety, cost, and recycling issues. Hence, water-based processing is highly attractive to facilitate a more sustainable industrial scale production.[12] Nevertheless, the final component properties of water processed LLZO need to match at least the ones from the organic route, in order to maintain the attractive electrochemical performance of LLZO. To that regard, Truong *et al.* found that the reverse-ion-exchanged $Li_5La_3Nb_2O_{12}$ (entry 1 in **Table 2.1**) had better sinterability than the pristine one and thus higher Li-ionic conductivity.[90] Huang *et al.* demonstrated an aqueous powder processing route for $Li_{6.4}La_3Zr_{1.4}Ta_{0.6}O_{12}$ combining the water-based attrition milling with the spray drying.[123] Uniform fine garnet powder with a particle size of 300 nm was prepared by attrition milling and formed large sphere-like secondary granulates of 5-20 µm after subsequent spray

drying. The pellets sintered from this powder had a relative density close to 94% and a conductivity of 0.419 mS cm^{-1} at room temperature. Peng *et al.* introduced an aqueous-based gelcasting process to fabricate $Li_{6.4}La_3Zr_{1.4}Ta_{0.6}O_{12}$ solid electrolytes, which had a high Li-ionic conductivity of 0.74 mS cm^{-1} at 25 ˚C.[121] This gelcasting technique showed suitable to fabricate structured garnet electrolytes by casting on elaborate molds. Moreover, by the freeze casting technique, vertically oriented porous structures can be obtained in the garnet layers from an aqueous slurry.[124-127] The garnet frameworks fabricated by this freeze casting technique can be applied as structural support for composite cathodes that have improved Li-ionic conduction compared to electrodes from pure cathode active material or highly tortuous composite cathodes from powder mixing.

The LHX can be reversed at elevated temperature in presence of excess Li sources, for which LiOH and Li_2CO_3 are commonly used. Therefore, aqueous processing of garnets is harmless to the electrochemical performance, if a final sintering step at temperatures around 1000 °C is used. Thus, suitable routes for a sustainable fabrication of garnet-based battery components exist, but challenges remain regarding low-temperature sintering, which is often necessary to incorporate high energy density cathode active materials.[128, 129]

Wang *et al.* densified $Li_{6.1}Al_{0.3}La_3Zr_2O_{12}$ by cold sintering at 350 °C using water or HNO_3 as aqueous media.[130] Although relative densities around 90% were achieved, the Li-ion conductivities of the cold-sintered garnet pellets were found to be five orders of magnitude lower than the ones obtained by conventional sintering. This degradation of conductivity was likely due to the dissolution of Al species from the Al-substituted garnet and its precipitation on the grain boundaries, which severely hinders the Li^+ conduction among grains. Ohta *et al.* achieved the sintering of $Li_{6.4}La_3Zr_{1.4}Nb_{0.6}O_{12}$ triggered by a reverse LHX reaction at 400 °C, which further enabled the densification of composite cathode consisting of this garnet and $LiNi_{1/3}Co_{1/3}Mn_{1/3}O_2$.[106] LiOH and $LiNO_3$ play the role as Li^+ providers to recover the Li content in protonated garnet during the hot pressing. It is notable that a high pressure (98 MPa in this research) is necessary in this process to assist densification. The sintered garnet pellet had 90% relative density and a Li^+ conductivity of 0.22 mS cm^{-1} at 25 °C. Moreover, the solid-state Li battery

prepared by the same method shows a low interfacial resistance around 200 Ω cm^2 (both cathode and anode sides), which is promising for industrial battery application.

In summary, handling and processing garnet materials in ambient atmosphere and by water-based processing are already feasible options to develop *e.g.* SSLBs as future high-energy density storage systems. In addition, the tendency to LHX could be used in future recycling strategies, as it could easily leach the Li from garnet materials in batteries properly designed and prepared for recycling. This way, a sustainable life cycle for future batteries, from materials preparation over cell design and manufacturing all the way to end-of-life and recycling can help to shape a greener future.

2.3.3 Garnet-based solid-state lithium batteries

In order to realize the integration of garnet separator into SSLBs, it is necessary to carefully deal with the two interfaces: the garnet/anode interface and the garnet/cathode interface.[131] The poor interface hinders the Li-ion transport, increases the resistance, and leads to the failure of the SSLBs.

The lithium metal anode has attractive advantages such as the low redox potential (-3.04 V *vs.* SHE) and the high theoretical capacity (3869 mAh g^{-1}), and is therefore a promising anode material for next-generation high-capacity batteries. However, the surface of garnet separators, due to LHX, often exhibits lithiophobic behavior, giving rise to poor wetting of lithium metal on the surface and large interfacial resistance.[67] In addition, the poor garnet/Li interface can also cause Li dendrite growth easily due to the inhomogeneous Li^+ flux across the interface.[132] Therefore, tremendous researches have been conducted on the improvement of the garnet/Li interface.[133]

To that end, first of all, the passivation layer on the surface of air-aged garnets consisting of the LHX products Li_2CO_3 and LiOH should be removed, which is usually done by thermal decomposition at 500-700 °C.[67, 107, 134] Recently, novel methods like rapid acid treatment by applying HCl,[135] H_3PO_4/NH_4F,[136, 137] or HCl/HF,[138] have been developed for removing and retrieving the lithiophilic surface of garnets. It is notable that the acid treatment time should be

controlled precisely because excess acid could corrode the bulk garnet and thus lower its Li-ion conductivity.

After obtaining the clean surface of garnet separators, an interlayer between garnets and Li metal can be added to further improve this interface. Various substances have been explored for this purpose. The first category of these substances is metallic or non-metallic simple substances that can form alloy with Li, such as Au,[108] In,[139] Ag,[140] Mg,[141] Al,[142] Sn,[143] Ge,[144] Si,[145] graphite.[146, 147] The second category is metal oxides, *e.g.* Al_2O_3,[148] SnO_2,[149, 150] ZnO,[151, 152] In_2O_3/SnO_2,[153] that can be lithiated by metallic Li. The third category is other inorganic compounds like Li_3N,[154] Cu_3N,[155] C_3N_4,[156] MoS_2,[157] *etc*. Li_3N has high Li-ion conductivity, low Li^+ migration energy barrier, strong wettability with Li metal, and electron insulation.[158-161] It can be introduced onto garnet surface directly by the evaporation of Li followed by a nitridation reaction,[154] but also through the reaction between molten Li and Cu_3N or C_3N_4.[155, 156] Similarly, MoS_2 reacts with Li to form Mo and Li_2S, which improves the wettability of Li on the garnet surface.[157] The last category is solid polymer electrolytes, including PEO,[162] (cross-linked) poly(ethylene glycol) methyl ether acrylate,[163] lithium poly(acrylamide-2-methyl-1-propane-sulfonate),[164] poly-dopamine.[165] These polymer electrolytes have the soft feature that can serve as a buffer interlayer, helping to form the solid-solid interface between garnets and metallic Li with uniform contact.

A good interface on the cathode side requires a good physical contact and electrochemical stability between garnets and CAMs. To obtain such interfaces, a high temperature (> 1000 °C) co-sintering of these materials is usually necessary.[131] The main challenge at such high sintering temperature is the chemical compatibility of CAMs with garnets. The decomposition reaction occurs between garnets and layer-structured cathode LCO thermodynamically above 700 °C,[166] between garnets and the spinel cathode LMO at 500 °C,[128] and between garnets and the olivine cathode LFP already above 400 °C.[167] Several strategies have been developed to overcome the thermal instability. By limiting the sintering temperature (1050 °C) and dwell time to 30 min, no decomposition was observed at the LCO/garnet interface and good cell performance was achieved.[168] By using the sintering agents such as Li_3BO_3[169] or $Li_{2.3}C_{0.7}B_{0.3}O_3$[170], the co-sintering temperature of LCO-garnet composite cathodes can be lowered to 700 °C. By applying

advanced sintering techniques, *e.g.* field-assisted sintering (also referred to spark plasma sintering (FAST/SPS)), bulk highly dense LCO/garnet composite cathodes with clear interface can be fabricated at 750 °C with a dwell time of only 10 min.[107, 171, 172] Apart from the direct co-sintering of CAMs with garnets, novel approaches are based on the infiltration of CAMs particles or their precursors into a porous garnet scaffold.[173, 174] In some cases, the polymer binder polyvinylidene fluoride (PVdF) or the plastic-crystal electrolyte succinonitrile (SCN) is added to fill in the voids between CAMs particles and the garnet frameworks and thus to improve the ionic conduction.[125, 127]

The thermal treatments are usually applied for layer-structured CAMs including LCO and NMC, as they have better chemical compatibility with garnets at high temperature. In the case of olivine CAMs such as LFP, the common approaches to build SSLBs often involve solid polymer electrolytes that can establish a soft interlayer between LFP and the garnet separator. The LFP cathode with PVdF binder for conventional LIBs was applied in SSLBs.[135, 175-177] To dissolve PVdF, the hazardous organic solvents N-methyl-2-pyrrolidione (NMP) or dimethylformamide (DMF) are usually used. Meanwhile, the ionic conduction inside the cathode is low. Certain plasticizers or liquid electrolytes, such as EC and ILs, are introduced into the cathodes to improve the ionic conduction as well as the interface between cathodes and ceramic solid electrolytes.[135, 177] Although ILs are often considered as green solvents,[178, 179] their costs foster the research on low cost alternatives. For the interfacial modification, PEO is also applied in SSLBs.[163, 180, 181] An LFP-PEO composite cathode can establish well-formed and high-conductive interfaces.[134, 182, 183] In all these reports, PEO was dissolved in NMP, DMF or acetonitrile (ACN). Although ACN is not classified as a health hazard, the high flammability and toxicity might still hinder the use of ACN in up-scaling processing. With this regard, the water-based processing route is desired in reducing manufacturing costs and improving the environmental benefits of battery production. On the other hand, PEO is soluble in water due to the hydrophilic interaction via hydrogen bonding with the water molecules.[184-186] Therefore, it is feasible to process the LFP-PEO composite cathode in aqueous media, leading to a ‘greener’ manufacture route. Water-processed LFP-PEO composite cathodes have been applied in PEO-based solid polymer batteries, but so far not yet in the garnet-based SSLBs.[187]

3 Materials and Methods

3.1 Synthesis and Processing

3.1.1 Solid-state synthesis

Solid-state reaction is one of the common synthesis methods for solid materials such as polycrystalline materials, single crystals, glasses etc. The end products are formed through the inter-diffusion of the solid starting materials at the controlled temperature. As the reaction mechanism highly depends on the diffusion rate, high temperature is generally required to accelerate the reaction. Moreover, reducing the particle size and homogeneous mixing of the starting materials are also helpful to enhance the contact area and thus increase the mass transfer. Therefore, a solid-state reaction is commonly composed of following steps: milling, pressing ("pelletizing"), and heating. These steps are often repeated in order to achieve the completion of the synthesis.

Ta- and Al-substituted $Li_{6.45}Al_{0.05}La_3Zr_{1.6}Ta_{0.4}O_{12}$ (LLZ:AlTa) powder was prepared via a four-step solid-state reaction. Briefly, the starting materials, $LiOH{\cdot}H_2O$ (Merck, 98%), La_2O_3 (Merck, 99.9%, pre-dried at 900 °C for 10 h), ZrO_2 (Treibacher, 99.5%), Ta_2O_5 (Inframat, 99.5%), and α-Al_2O_3 (Inframat, 99.9%) were mixed in stoichiometric amounts. The chemical equation of the solid-state reaction can be expressed as:

$$6.45\ LiOH{\cdot}H_2O + 0.025\ Al_2O_3 + 1.5\ La_2O_3 + 1.6\ ZrO_2 + 0.2\ Ta_2O_5$$

$$\rightarrow Li_{6.45}Al_{0.05}La_3Zr_{1.6}Ta_{0.4}O_{12} + 9.675\ H_2O\uparrow \qquad \text{(Equation 3.1)}$$

20 mol% $LiOH{\cdot}H_2O$ in excess was added to compensate for lithium volatilization due to the decomposition of LLZ:AlTa during the high-temperature preparation. After grinding in a mechanical mortar for 1 h, the powder mixture was pressed (130 MPa, 2 min) into pellets for calcination using Al_2O_3 crucible with the closed lid in air at 850°C and 1000°C for 20 h each. Grinding and pressing were repeated between the calcination steps. After the final calcination, the pellets were grinded into powder in mechanical mortar for 1 h. The obtained powder was then ball-milled using ZrO_2 balls (Ø2-5 mm) in ethanol on a rolling band for 60 h and afterwards dried at 70°C in air, followed by further drying at 80 °C under reduced pressure (50 kPa).

The LLZ:AlTa powder was used to prepare the garnet solid electrolyte separators in the following tape-casting process. In addition, Al-free Ta-substituted $Li_{6.6}La_3Zr_{1.6}Ta_{0.4}O_{12}$ (LLZ:Ta) powder was prepared in the same way, which is used in LCO/LLZ:Ta composite cathode for the garnet-supported SSLBs.

3.1.2 Tape-casting

Tape-casting is a well-known technique for large-scale production of ceramic components with layered structures.[188-190] As shown in **Figure 3.1**, large-area foils of ceramic material are prepared from a slurry containing ceramic powder, dispersing agents, binders and plasticizers in a suitable solvent, which is cast in a continuous process and can be cut into desired shape to obtain the component accordingly.

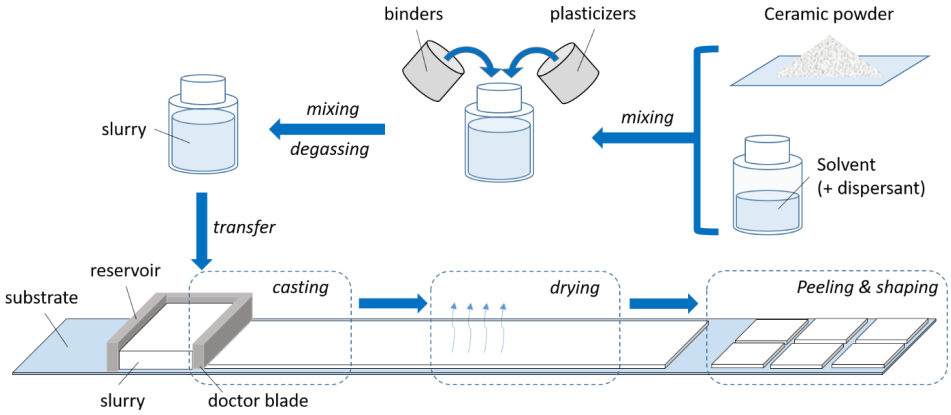

Figure 3.1 Schematic representation of tape-casting process.

Table 3.1 Formulation of slurry for tape-casting of garnet-based separators

Materials	Function	Weight Percent [%]
LLZ:AlTa	solid	52.40
deionized water	solvent	43.66
methylcellulose	binder	0.44
polyethylene glycol	plasticizer	1.75
glycerol	plasticizer	1.75

An aqueous polymer solution was prepared in advance by dissolving methylcellulose (MC, Alfa Aesar), polyethylene glycol (PEG400, Merck) and glycerol (Merck, 99%) in deionized water. The ball-milled LLZ:AlTa powder was added into the polymer Solution. This suspension was then homogenized under vacuum (10 kPa) with 5 mm diameter ZrO_2 beads in a planetary mixer (Thinky, USA) at 1000 rpm for 5 min to form the slurry for tape-casting. The formulation of the slurry is summarized in **Table 3.1**. Afterwards, the obtained slurry was cast on a Mylar foil using a moving doctor blade. The thickness of green[a] tapes was controlled by varying the gap of a doctor blade. After drying overnight at ambient atmosphere, the green tapes were manually peeled off the Mylar foil and cut into desired sizes. Two layers of the green tape were laminated at 80 °C with a pressure of 120 MPa for 2 min to improve the packing density. The laminated green tapes were punched into discs with 14 mm diameter for sintering.

For the tape-casting of the mixed cathode consisting of LLZ:Ta and LCO (Alfa Aesar, 99.5%), the LLZ:AlTa of the above-mentioned slurry formulation in **Table 3.1** was replaced by the LLZ:Ta and LCO powder in a weight ratio of 1:1. The rest processing steps were kept the same as the ones for preparing the tapes of pure LLZ:AlTa separators. Two layers of the mixed cathode green tapes were laminated at 80 °C with a pressure of 250 MPa or 500 MPa for 2 min to improve the packing density. The laminated green tapes were punched into discs with 10 mm diameter for sintering.

For the tape-casting of the LFP/PEO composite cathode, PEO (MW 600,000, Sigma-Aldrich) and LiTFSI (99+%, Sigma-Aldrich) with a EO:Li^+-ratio of 8:1 were first dissolved in deionized water to give polymer solutions with a concentration of 50 $g_{PEO}\ L_{solvent}^{-1}$. LFP powder (Hirose Tech, Taiwan) and SuperP carbon black (99%, Alfa Aesar) were mixed in a mortar by hand and then poured into the prepared PEO aqueous solution (50 $g_{PEO}\ L_{water}^{-1}$). The mixture was well homogenized by planetary mixer (Thinky, USA). The obtained slurry was tape-cast on a battery-grade Al foil by a doctor blade device (MTI, USA). The thickness of cathodes was controlled by the height of the doctor blade. After drying at 50 °C in air for 30 min, the cathode tapes were punched with a 10 mm cutter and further dried overnight at 80 °C in a vacuum oven (Büchi glass oven B-585 Drying,

[a] green: in the ceramic society, the phrase 'green' refers to the object composed of ceramic powders and sometimes organic additives that has been given a designed shape and is ready for sintering. For example, green pellets, green tapes, green bodies. To avoid misunderstanding, the word 'green' in this thesis is used only for this meaning, but not for the meaning of sustainable, environmental friendly or similar.

Germany). Afterwards, the cathodes were stored in an Ar-filled glovebox. Cathodes with various weight ratio of LFP:SuperP:PEO were prepared and more details are summarized in **Table 3.2**.

Table 3.2 Composition, active material loading and thickness of the prepared LFP-PEO cathode electrodes

Cathodes	Weight ratio of LFP:SuperP:PEO			Volume ratio of LFP:PEO	LFP-loading [mg cm^{-2}]	Thickness [µm]
	LFP	SuperP	PEO			
C1	15	3	2.5	2:1	3.7-4.6	50-60
C2	15	3	3.75	1.5:1	2.7-3.2	45-55
C3	15	3	5	1:1	2.8-3.2	40-50
C3t	15	3	5	1:1	8.9-10.2	110-120

For the preparation of PEO-LiTFSI polymer membranes, PEO and LiTFSI with a EO:Li^+-ratio of 8:1 were dissolved in deionized water, bio-ethanol (100% BioFair, Richter Chemie) or ACN (99.8%, Sigma-Aldrich) to give polymer solutions with a concentration of 50 g_{PEO} $L_{solvent}^{-1}$. The polymer solutions were poured onto Mylar foils and dried in ambient atmosphere overnight. The obtained PEO membranes were further dried together with the Mylar foil substrates in a vacuum oven at 80 °C overnight. Afterwards, the PEO membranes were stored in an Ar-filled glovebox.

The SiO_x-modified PEO membranes (Si-PEO) were prepared according to literatures[191, 192]. Briefly, PEO was first dissolved in deionized water to give an aqueous polymer solution with a concentration of 50 g_{PEO} L_{water}^{-1}. After $NH_3 \cdot H_2O$ (28% solution, Alfa-Aesar) was added to adjust the pH of the solution to the value 10.5-11, tetraethyl orthosilicate (TEOS, 99+%, Alfa-Aesar) was added dropwise into the polymer solution under stirring. The reaction was performed at 70 °C for 24 h with a mass ratio of TEOS:PEO at 1:2.. After the reaction finished, the polymer solution was cooled down, and LiTFSI was added in a EO:Li^+-ratio of 8:1. The polymer solution was dropped onto Mylar foils by pipette to form round polymer drops with a diameter of 12 mm. These polymer drops were dried in ambient atmosphere overnight. The obtained Si-PEO membranes were further dried together with the Mylar foil substrates in a vacuum oven at 80 °C overnight. Afterwards, the membranes were stored in an Ar-filled glovebox.

3.1.3 Sintering

Sintering, specifically solid-state sintering in our case, is the bonding and densification of particles by heat treatment below the melting point of the material. The driving force of sintering is the

reduction in the free energy of the powder system mainly provided the curvature of the particle surfaces due to densification and coarsening.[193]

For sintering the garnet separators, the laminated green tape discs were placed between two MgO plates with LLZ:AlTa-coatings inside a closed alumina crucible. The crucible was heated up in air at a heating rate of 1 °C min^{-1} to 700 °C with 1 h dwell time and subsequently at a heating rate of 10 °C min^{-1} to 1175 °C with 4 h dwell time for sintering. The sample were subsequently freely cooled to room temperature. The obtained dense garnet discs were labeled as LLZ-air. Samples of LLZ-air were further placed on an alumina boat and annealed in a tube furnace with flowing argon at 800 °C with 1 h dwell time and were noted as LLZ-Ar.

To prepare the above mentioned LLZ:AlTa-coatings at MgO plates, the LLZ:AlTa powder was first homogeneously spread on the top of a MgO plate, followed by the heat treatment at 1185 °C for 2 hours inside a closed alumina crucible.

For sintering the mixed cathode LCO/LLZ:Ta, the prepared green tape discs were placed on an alumina plate inside an alumina crucible with or without lid. For the case of using closed crucible, certain amount of LiOH powder was added around the alumina plate to create a Li_2O atmosphere when sintering. The crucibles were heated up in air at a heating rate of 2 °C min^{-1} to 750 °C with 1 h dwell time and subsequently at a heating rate of 10 °C min^{-1} to 1050 °C with 0.5, 2, 4, or 6 h dwell time for sintering, followed by free cooling to r.t.. Afterwards, the sintered composite cathodes were immediately transported into an Ar-filled glovebox and stored there.

3.1.4 Solid-state batteries assembly

The fabrication route of the SSLB containing LFP-PEO cathode is described in **Figure 3.2**. In an Ar-filled glovebox, a gold thin film was sputtered (20 mA, 30 s) on the top of the prepared garnet separator to assist Li adhesion using a desktop sputter coater (Cressington 108 auto coater, UK). A fresh lithium foil (99.9%, Alfa Aesar) was calendered by hand and punched with a 10 mm cutter. The Li disc was then attached to the gold-sputtered side of the garnet sheet and was heated to melt. In case of the thick cathodes, a similar procedure was used for In disc as anode to avoid dendrite formation. After cooling down, the LFP-PEO composite cathode disc was attached to the other side of the garnet sheet. The full cell was assembled in a Swagelok cell using Ni plates as

current collectors. The assembled full cells were placed into spring-compressed (10 N) Swagelok cells and sealed. Prior to tests, the cell was stored at 80 °C overnight ensuring a good interfacial contact between garnet sheet and the LFP/PEO composite cathode, and cooled down to 60 °C for battery testing.

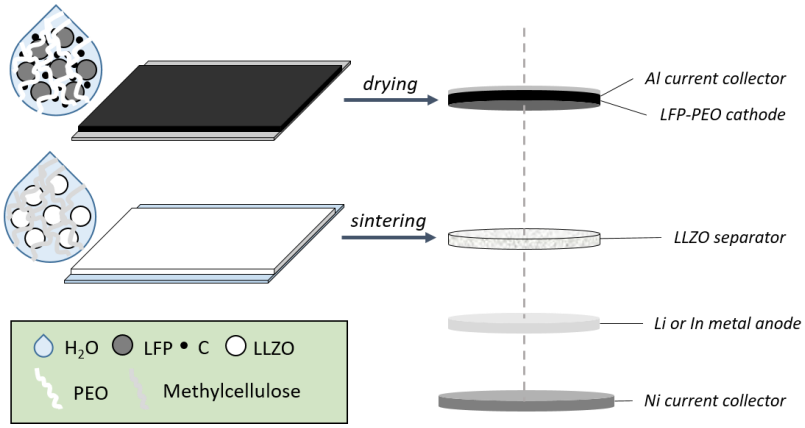

Figure 3.2 Schematic of the water-based fabrication of the LFP-PEO composite cathode and the garnet separator for SSLBs.

The fabrication route of the SSLB containing LCO/LLZ:Ta mixed cathode is described in **Figure 3.3**. The preparation of the anode side with In was with the same procedure as the SSLB with a LFP-PEO cathode. On the cathode side, a SiOx-modified PEO membrane was first placed on the top of the garnet sheet. This special PEO membrane can improve the contact between the garnet separator and the mixed cathode. The sintered LCO/LLZ:Ta cathode with a sputter-coated gold thin film (20 mA, 150 s) on the top as current collector was then attached to the PEO membrane. The full cells were assembled in the same Swagelok cell sets as described before. Prior to tests, the cell was stored at 80 °C overnight, and cooled down to 60 °C for battery testing.

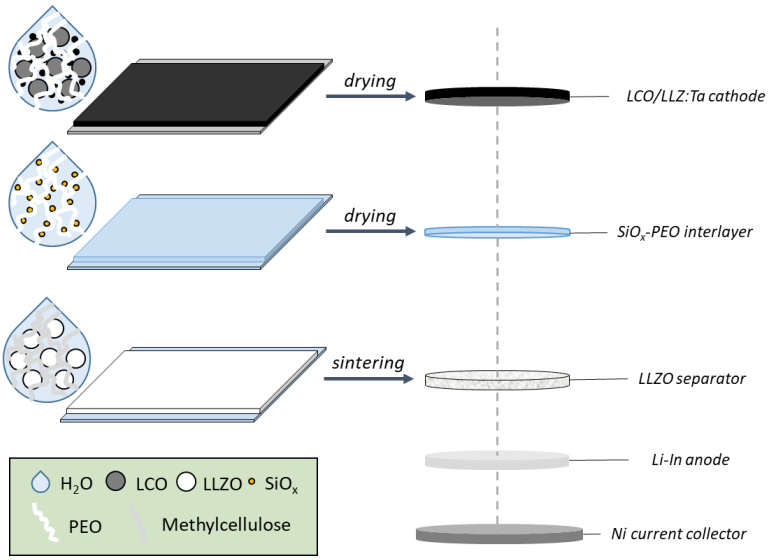

Figure 3.3 Schematic diagram of the water-based fabrication of the SSLBs consisting of the LCO/LLZ:Ta mixed cathode and the garnet separator.

3.2 Material Characterization

3.2.1 Particle size distribution

Laser diffraction is one of the commonly used methods to measure the particle size distribution (PSD) of dispersed particles in a suspension.[194] When a laser beam passes through the dispersion, light is diffracted by the particles. Large particles scatter intensively at narrow angles relative to the laser beam, while small particles scatter weakly at wide angles.[194] Hence, angle and intensity of the scattered light are recorded and analyzed. There are two optical models applied to mathematically transform the data to PSD. The first one is Fraunhofer approximation, which simplify the calculation by assuming that the particles are spherical and opaque, scatter equivalently at wide angles as narrow angles, and interact with light in a different manner than the medium.[194] These assumptions make the Fraunhofer approximation an unsuitable model for analyzing small particles. The other model is Mie theory, which is an exact solution to Maxwell's electromagnetic equations for scattering from spheres.[195] It exceeds Fraunhofer

approximation to include sensitivity to wide angle scatter (smaller sizes) and a wide range of opacity, but still makes assumptions that the particles are spherical and the ensemble is homogeneous.[194] By applying the Mie theory, it is required to know the refractive index of the particle and the surrounding medium.

In this thesis, PSD of LLZ:AlTa powder was determined in ethanol by laser diffraction method using Fraunhofer approximation on a Horiba LA-950V2 instrument (Japan), whereas the PSD of LFP particles was determined using Mie theory by given the refractive index of LFP as 1.63. Prior to each measurement, the suspensions are homogenized in ultrasonic bath for 5 min.

3.2.2 Rheological analysis

Most fluids (*e.g.* suspensions) are non-Newtonian fluids, which cannot be defined by a single value of viscosity.[196] The rheology of these fluids (*e.g.* slurries), can be described as the fluid behavior in response to applied forces, which can be measured by a shear rheometer equipped with concentric rotational cylinder.[197] The fluid is placed within the annulus of one cylinder inside another. The inner cylinder is rotated at a user-defined speed *u*, giving rise to the shear rate $\dot{\gamma}$ inside the annulus, which is the quotient of the speed *u* divided by the distance between the concentric cylinders *y*:

$$\dot{\gamma}[s^{-1}] = \frac{u\,[m{\cdot}s^{-1}]}{y\,[m]} \qquad \text{(Equation 3.2)}$$

To response to the applied force by the rotating inner cylinder, the fluid tends to drag the outer cylinder around, and the force *F* on it is measured, which can be converted to shear stress τ by dividing the force *F* with the contact area of cylinder with the fluid *A*:

$$\tau\,[Pa] = \frac{F\,[N]}{A\,[m^2]} \qquad \text{(Equation 3.3)}$$

Afterwards, the dynamic viscosity η of the fluid can be obtained by dividing the shear stress τ with the shear rate $\dot{\gamma}$:

$$\eta\,[Pa \cdot s] = \frac{\tau\,[Pa]}{\dot{\gamma}\,[s^{-1}]} \qquad \text{(Equation 3.4)}$$

In this thesis, the rheological property of the water-based LLZ:AlTa slurry was measured by a rheometer Physica MCR100 (Anton Paar, Austria) with a cylinder DG26.7 measuring system at room temperature.

3.2.3 X-ray diffraction

X-ray diffraction (XRD) is a non-destructive method for determination of atomic and molecular structures in crystalline materials. Incoming X-ray waves are scattered by regularly arranged atoms, primarily by the atoms' electrons, producing spherical waves emitting from the electrons.[198] In most directions these scattered waves counteract with each other due to destructive interference, while constructive interference occurs in some specific directions, *e.g.* reflection, which can be described by Bragg's equation:[199]

$$n \cdot \lambda = 2 \cdot d \cdot \sin\theta \qquad \text{(Equation 3.5)}$$

where n is an integer, λ is the wavelength of the X-ray wave, d is the distance between diffracting planes, and θ is the incident angle. The left side of the equation is related to the wavelength of the X-ray waves only, which keeps constant before and after the elastic scattering. The right side of the equation expresses exactly the phase difference between the two waves, in which θ is a variable controlled by experimenters. These reflections fulfilling Bragg's law are recorded on the diffraction pattern, which is also called diffractogramme, usually plotting the intensity of reflections versus 2θ. In this case, d can be calculated accordingly, and thus the crystal information is further obtained.[200] Rietveld refinement is one of the most used techniques for the analysis of XRD patterns, which fits a calculated profile to the experimental data.[201] The height, width, and position of those reflection peaks are used to determine the crystal structures. Different crystal phases in mixtures can also be qualitatively separated and quantitatively determined.

In this thesis, samples, in form of powder, tapes, or pellets, were characterized for their phase purities by XRD on a Bruker D4 Endeavor device (Bruker, Germany) using Cu Kα radiation equipped with a 1D detector LynxEye. The TOPAS V4 software (Bruker AXS) was used for Rietveld refinements to determine the lattice parameters of the samples.

3.2.4 Scanning electron microscope and energy-dispersive X-ray spectroscopy

Scanning electron microscope (SEM) takes images of a sample through scanning the sample surface with a focused electron beam. The primary electrons interact with the atoms in the sample, producing various signals for detection, including back-scattered electrons (BSEs), secondary electrons, characteristic X-rays, *etc.*[202]

BSEs are the high-energy electrons reflected or back-scattered by the atoms in the sample via elastic scattering. The back-scattering effect is much stronger by heavy elements than by light elements, resulting in brighter areas in the SEM images.[202] Thus, BSEs are applied to differentiate chemical compositions.

Secondary electrons are low-energy electrons ejected from the conduction or the valence bands of the sample by primary electron beams via inelastic scattering, and characteristic X-rays emit at the same time. With the increasing incident angle of the primary electron beam on the sample surface, more secondary electrons are generated and thus more probably to be detected, resulting in brighter areas in the SEM images for steep surfaces and edges than flat surfaces.[202] Therefore, secondary electrons are used for topographical analysis.

When a secondary electron is ejected from the inner electron shell of the atoms in the sample, an electron hole is created where the electron was. In this case, an electron from an outer electron shell with higher energy fills this hole, and the energy difference between the two electron shells is released in the form of an X-ray called characteristic X-ray, which is collected in the energy-dispersive X-ray spectroscopy (EDS).[203] Such energy differences are correlated to the atomic structure of the emitting elements, and can be predicted by Moseley's law. Therefore, EDS is used to determine elemental composition.

In this thesis, BSE-SEM images and EDS analysis were taken by the Hitachi TM3000 tabletop SEM. For investigation on cross-sections, samples were embedded in EpoFix epoxy resin (Struers, Germany) and mirror-polished. Prior to measurements, all samples were coated with gold thin film using a desktop sputter coater (Cressington 108 auto coater, UK) to form a conductive top layer in order to avoid the possible charging problem during measurements.

3.2.5 Chemical element analysis

Inductively coupled plasma optical emission spectroscopy (ICP-OES) is an analytical method for quantitative determination of chemical elements.[204] The sample in liquid state (*e.g.* solution) is sprayed into mist and introduced directly inside the plasma flame consisting of Ar atoms and charged particles, where excited atoms and ions in the sample are produced after the collision with the electrons and charged ions. Afterwards, electromagnetic radiation is emitted when the excited atoms and ions return to the ground state. These emissions containing characteristic wavelengths of the elements involved are detected and the atomic spectra lines are recorded in the emission spectrum. By the comparison of the intensity of each line with the previously measured intensities of known concentrations of the elements, the concentration can be determined with the help of calibration lines.[204]

In this thesis, the elemental stoichiometry of the LLZ:AlTa and LLZ:Ta samples was determined using an ICP-emission spectrometer (iCAP 7600, ThermoFisher). The powder samples were dissolved in H_2SO_4 together with $(NH_4)_2SO_4$, and the solutions were then diluted for analysis.

3.2.6 Thermal analysis

Thermogravimetry (TG) is a method to measure the mass change of a sample as the function of temperature or time. The sample is placed on a precision balance inside a furnace with controllable temperature. The weight gain or loss of the sample is recorded when the furnace is heated up.[205] A variety of atmospheres can be used for the measurement, including air, vacuum, inert gas, reducing gases, etc. TG is often combined with other analytical methods such as mass spectrometry (MS) to determine the compositions of the decomposed compounds that cause the weight loss of the sample.[206]

In this thesis, TG was conducted on the thermal analyzer (Netzsch STA 449 F1 Jupiter) coupled with MS (Netzsch 403 C Aeolos) in air atmosphere.

3.2.7 Raman spectroscopy

Raman spectroscopy is a spectroscopic technique to determine vibrational modes of molecules or solids through the inelastic scattering of light influenced by the polarizability of the electrons

in the sample.[207] When a monochromatic light (*e.g.* laser) is targeted on the surface of the sample, the photons excite the molecule from a vibrational energy state into a virtual energy state for a short time before the photon is emitted via Raman scattering, meaning that the energy of the emitted photon is either lower or higher than the incident one, resulting in upshift or downshift of the emission wavenumber in the spectra, respectively. This difference in wavenumber is called Raman shift.[208]

In this thesis, the impurities on the surface of LLZ-air and LLZ-Ar separators were identified by Raman spectroscopy, which was carried out with a Renishaw inVia Raman microscope using a solid-state 532 nm excitation laser and 1800 lines per mm grating.

3.2.8 Infrared spectroscopy

Infrared spectroscopy (IR) is a measurement technique for characterization of chemical substances or functional groups via the interaction of infrared radiation with the sample by absorption, emission, or reflection.[209] The mid-IR (4000-400 cm^{-1}) is commonly used to study fundamental vibrations and rotational-vibrational structures, including stretching (symmetric and antisymmetric) and bending (such as scissoring, rocking, wagging and twisting). The mathematical data-process "Fourier transform (FT)" is usually applied to convert the raw data into the actual spectrum, and the sampling technique "attenuated total reflection" (ATR) allows the direct examination of solid or liquid samples without further preparation.[209]

In this thesis, PEO membranes were characterized by attenuated total reflection Fourier transform infrared spectroscopy (ATR-FTIR) in an argon-filled glovebox (O_2 and H_2O < 0.5 ppm). Samples were dried in a vacuum oven (Büchi glass oven B-585 Drying, Germany) at 80 °C overnight prior to the measurements. The characterization was carried out using a FTIR spectrometer (Bruker Vertex 70, Germany) and each measurement was performed in the range of 4000-400 cm^{-1} at a resolution of 4 cm^{-1} for 50 scans.

3.3 Electrochemical Characterization

For all electrochemical measurements, a VMP-300 multi-potentiostat (BioLogic, France) combined with a climate chamber (Vötsch VT4002EMC) was used.

3.3.1 Electrochemical impedance spectroscopy

Electrical resistance is the ability of a circuit element to resist the flow of electric current. Ohm's law defines the resistance in terms of the ratio between voltage and current, but its use is limited to only one circuit element, the ideal resistor. However, circuit elements in the actual conditions often exhibit much more complex behavior. In this place, the concept 'impedance', a more general circuit parameter, is used instead of resistance, and extends the concept of resistance to the alternating current (AC) circuits.[210]

Electrochemical impedance spectroscopy (EIS) is usually measured by applying AC potential to an electrochemical cell and then measuring the current through the cell.[211] It is assumed that a sinusoidal potential excitation is applied. The response to this potential is an AC current signal, which can be analyzed as a sum of sinusoidal functions. Normally a small excitation signal is used so that the response of the cell is pseudo-linear. In this pseudo-linear system, the current response to a sinusoidal potential will be a sinusoid at the same frequency but shifted in phase.[212] After the amplitude (the amount of impedance, $|Z|$) and the phase shift ϕ are registered, the real (Z_{re}) and imaginary part (Z_{im}) of the impedance can be calculated by **Equation 3.6** and **Equation 3.7**, respectively.

$$Z_{re} = |Z| \cdot \cos \emptyset \qquad \text{(Equation 3.6)}$$

$$-Z_{im} = |Z| \cdot \sin \emptyset \qquad \text{(Equation 3.7)}$$

The impedance *Z* is then represented as a complex number

$$Z = Z_{re} - i \cdot Z_{im} = |Z| \cdot (\cos \emptyset + i \cdot \sin \emptyset) \qquad \text{(Equation 3.8)}$$

If the real part is plotted on the x-axis and the (negative) imaginary part on the y-axis of a chart, a 'Nyquist plot' will be obtained (**Figure 3.4**). Each point on the Nyquist plot is the impedance at one frequency (*f*). Low frequency data are on the right-hand side of the plot and higher frequencies are on the left. By analyzing the Nyquist plot, some physico-chemical characteristics, such as inductance, resistor *R* and double layer capacitor *C*, can be obtained.[212]

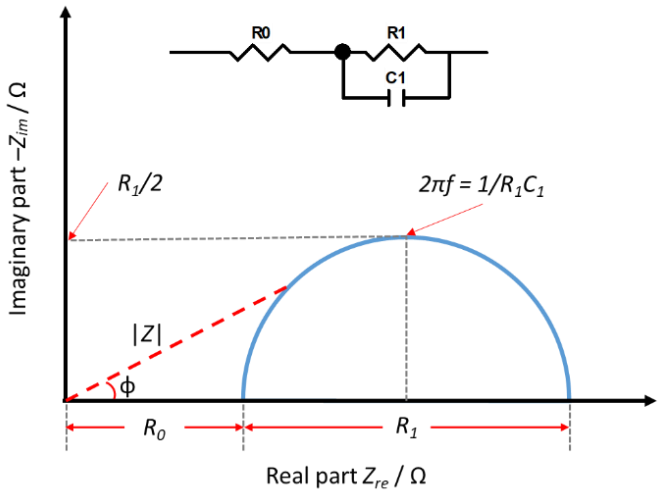

Figure 3.4 Schematic explanation of Nyquist plot, and the equivalent circuit used for interpreting the Nyquist plot.

An equivalent circuit is often used to help understanding the physical meaning of each impedance components in the complex system. Parallel elements of the resistor and the capacitor are usually used to fit semicircles in the Nyquist plot, but sometimes the capacitor contribution is not the same as the ideal capacitor. In this case, a mathematic model called constant phase element (*CPE*) *Q* is used to improve the fitting of the imperfect capacitors,[212] and then the ideal *C* can be calculated by **Equation 3.9**:

$$C = \frac{(Q \cdot R)^{\frac{1}{n}}}{R} \qquad \text{(Equation 3.9)}$$

where *n* is an exponent obtained from the fitting results.

By analyzing the obtained capacitance values, the contribution for the impedance can be interpreted and assigned, for instance in electroceramic samples, according to Irvine *et al.* (**Table 3.3**).[213]

Table 3.3 Capacitance values and their possible interpretation[213]

Capacitance [F]	Phenomenon Responsible
10^{-12}	bulk
10^{-11}	minor, second phase
10^{-11}-10^{-8}	grain boundary
10^{-10}-10^{-9}	bulk ferroelectric
10^{-9}-10^{-7}	surface layer
10^{-7}-10^{-5}	sample-electrode interface
10^{-4}	electrochemical reactions

In this thesis, EIS was used to measure the impedance of LLZ-Ar samples. One LLZ-Ar sheet was sandwiched between two metallic Li foils and heated up to 300 °C to obtain a better contact at the interface. EIS was measured in the frequency range from 7 MHz to 10 mHz with an electrical field perturbation of 20 mV. A fitting of the impedance spectrum was conducted in the software ZView (Scribner). After obtaining the total resistance value R_{total} of the sample, the total conductivity σ of it could be calculated by **Equation 3.10**:

$$\sigma\ [S \cdot cm^{-1}] = \frac{L\ [cm]}{A\ [cm^2] \times R_{total}\ [\Omega]} \qquad \text{(Equation 3.10)}$$

where L is the thickness of the sample and A the contacting area between the sample and the Li metal electrode.

3.3.2 Cyclic voltammetry and linear scan voltammetry

The cyclic voltammetry (CV) is an electrochemical technique to investigate the electroactive reactions.[214, 215] CV is operated in a three-electrode circuit, which is composed of working electrode (WE), reference electrode (RE) and counter electrode (CE). The potential of the WE changes linearly with time between the upper and lower limit. When the potential changes only in one direction (either towards upper limit or towards lower limit), this technique is then called linear scan voltammetry or linear sweep voltammetry (LSV). This loaded potential acts as an excitation signal and is exactly measured by the RE. As a response signal, a current flows between WE and CE. The electrode potential runs through an electrochemical window, in which the electrochemical processes on the WE can proceed, so that a current flows between WE and CE.

The current can be assigned to the corresponding potential in the registered current-voltage-diagram, the so-called cyclic voltammogram. Every peak in cyclic voltammogram represents a redox reaction on the surface of the WE inside the electrolyte. The anodic peak (upwards) corresponds to the oxidation and the cathodic peak (downwards) corresponds to the reduction. The potential of each electrochemical redox reaction can be determined by the position of the peaks.

In this thesis, CV was used to investigate the electrochemical stability of the LLZ-Ar sample and the Li stripping/plating behavior. It was conducted in the potential range from -0.02 V to 5 V *vs.* Li^+/Li at a scan rate of 0.02 mV s^{-1}. The LLZ-Ar sample for CV measurement was sandwiched between one metallic Li foil and one In foil. The Li metal electrode acted as both CE and RE, while the In metal electrode acted as WE. LSV was used to investigate the oxidation stability of the PEO-based membranes, which was sandwiched between one gold WE and one metallic Li CE. The LSV was conducted in the potential range from 3 V to 5 V *vs.* Li^+/Li at a scan rate of 0.02 mV s^{-1}.

3.3.3 Galvanostatic cycling

Galvanostatic cycling is an electroanalysis technique to investigate electrochemical performance of batteries.[216] The changing rate of potential in a fixed range is measured at constant current density for several times. When positive current density is applied, it will show the charging cycle, whereas the discharging cycle will be shown when applying negative current density. This technique is close to the actual application.

In this thesis, a constant-current-constant-voltage (CC-CV) process was used for charging the battery. The purpose of using CC-CV process for charging is to mitigate the capacity loss at the test voltage limit, which is induced by the internal resistance and the slow transport of charge carriers. It avoids the stop of charging due to kinetic limitations and is beneficial for showing the functionality of novel cathode structures.

For the SSLBs with the LFP cathode, the battery was charged to 3.9 V *vs.* Li/Li^+ or 3.3 V *vs.* $Li\text{-}In/Li^+$ (if a Li-In anode is used) with a constant current density of 10, 20, or 50 µA cm^{-2}, and was then held at the voltage until the current dropped to 5 µA cm^{-2}. Afterwards, the battery was discharged to 2.6 V *vs.* Li/Li^+ or 2.0 V *vs.* $Li\text{-}In/Li^+$ with a constant current density of 10, 20, or 50 µA cm^{-2}.

For the SSLBs with the LCO cathode and Li-In anode, a formation cycle was first performed by charging to 3.6 V *vs.* Li-In/Li^+ and discharging to 2.8 V *vs.* Li-In/Li^+ both with a constant current density of 50 μA cm^{-2}. In the following cycles, the CC-CV process was used for charging. The battery was charged to 3.6 V *vs.* Li-In/Li^+ with a constant current density of 50 μA cm^{-2}, and was then held at the voltage until the current dropped to 5 μA cm^{-2}. Afterwards, the battery was discharged to 2.4 V *vs.* Li-In/Li^+ with a constant current density of 50 μA cm^{-2}.

4 Water-Based Fabrication of Garnet-Based Separator

This chapter is based with modification on the publication 'Water-based fabrication of garnet-based solid electrolyte separators for solid-state lithium batteries' by Ye et al. It was published during the thesis and reprinted (adapted) with permission from [98].

4.1 Tape-Casting of Garnet Solid Electrolyte Layers

Ta- and Al-substituted $Li_{6.45}Al_{0.05}La_3Zr_{1.6}Ta_{0.4}O_{12}$ (LLZ:AlTa) was selected as the SE material because Ta and Al can stabilize the cubic structure of LLZO and lead to an increased ionic conductivity.[66, 217] The synthesized powder corresponds to a cubic LLZO phase, as follows from the XRD patterns (**Figure 4.1**). A small impurity phase of Li_2CO_3 detected in XRD can be attributed to the excess lithium reagent added into the synthesis process for compensating lithium loss during the whole sintering process, which is confirmed by ICP-OES giving the overall lithium concentration high than the targeting $Li_{6.45}Al_{0.05}La_3Zr_{1.6}Ta_{0.4}O_{12}$ (**Table 4.1**).

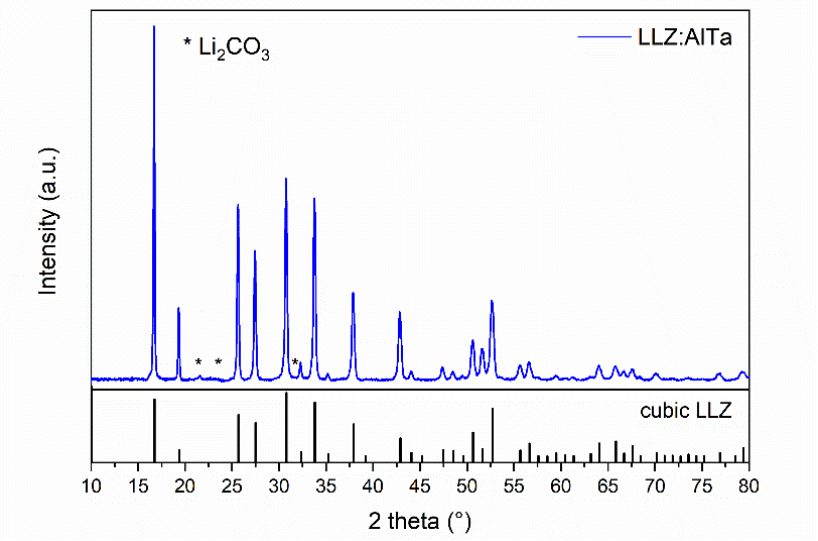

Figure 4.1 XRD pattern of as-synthesized LLZ:AlTa powder (Reference pattern: ICSD#182312).

For tape-casting, a slurry comprising the milled LLZ:AlTa powder and aqueous binder system was prepared. The PSD of the LLZ:AlTa powder (**Figure 4.2**) shows a trimodal curve for the powder before ball-mill, indicating the presence of large particles or agglomerates, whereas the powder after ball-milling shows only one narrow peak with a D_{50} value of 1.17 µm and is suitable for the tape-casting process.

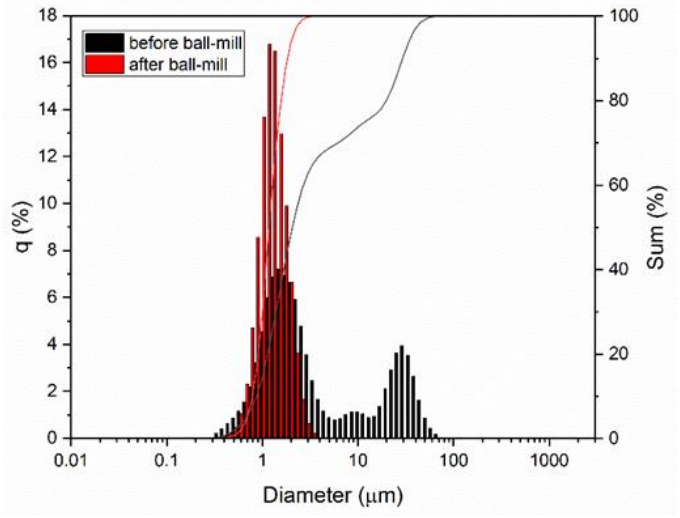

Figure 4.2 PSD of LLZ:AlTa powder before and after ball-milling.

The commercial CMC binder contains sodium, which might have negative effect on the stability of garnets at sintering temperature. In order to investigate the thermal stability of LLZ:AlTa at elevated temperature with the presence of sodium species, Na-doped LLZ:AlTa pellets were prepared by mixing and pressing 0.5 g LLZ:AlTa powder and 0.05 g $Na_2CO_3 \cdot H_2O$, followed by sintering at 1175 °C for 4 hours. The XRD pattern of the sample after sintering (**Figure 4.3**) clearly shows that the sodium species can react with LLZ:AlTa to form several secondary phases. To avoid this uncertain side effect, I choose therefore Na-free MC binder. It is also worth noting that the MC, PEG and glycerol in this aqueous binder system are all non-toxic that are often used as food additives or pharmaceutical applications due to their harmless to humans.[218]

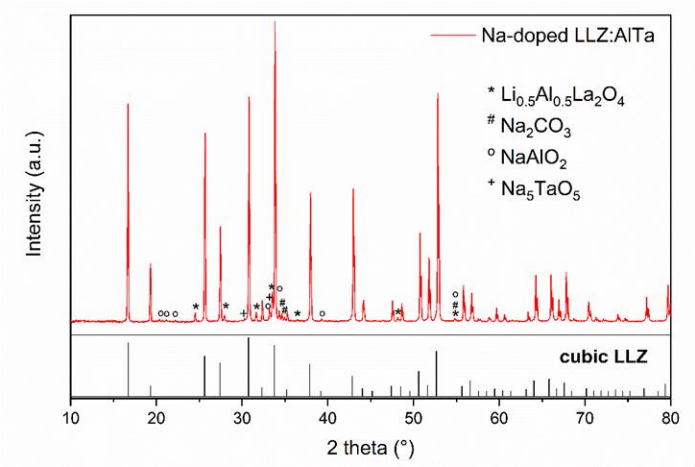

Figure 4.3 XRD pattern of the sintered Na-doped LLZ:AlTa pellet sintered at 1175 °C for 4 hours.

A major advantage of the aqueous slurry preparation presented here is that there is no additional organic dispersant needed, because the water itself is already a good dispersant. Additionally, it is well known that the immersion of LLZO in water triggers a Li^+/H^+ exchange reaction with water according to **Equation 2.3** and results in the increase of pH up to 11-12.[81, 82, 84] A large amount of OH^- anions will be adsorbed on the surface of LLZ:AlTa particle to provide the electrostatic repulsive force, which further stabilizes the suspension. In my case, the pH value of the prepared slurry, due to the high solid loading, reached pH 12.5 directly after mixing LLZ:AlTa powder with the aqueous polymer solution.

The rheological behavior of the prepared slurry was then investigated, which shows a shear thinning behavior (**Figure 4.4**) in the suitable range for tape-casting. The high viscosity of the slurry at low shear rate will prevent the inhomogeneous sedimentation of ceramic particles during the drying step after casting. This is an important point to the process, because the drying of aqueous tapes takes much longer time than ethanol-based ones due to the slower evaporation rate of water. In industrial processing, however, the drying time can be reduced through application of heat below and/or above the tapes.

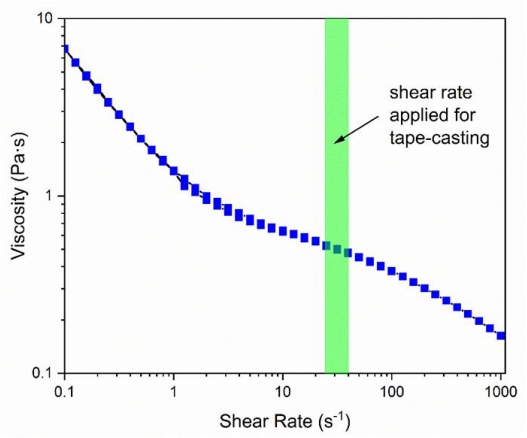

Figure 4.4 Viscosity versus shear rate curve of the prepared slurry for tape-casting.

Afterwards, the concentration of polymer binder and plasticizers was investigated. The weight-ratio of MC:glycerol:PEG=4:2:1 was first used for tape-casting (Entry 1 in **Table 4.1**). As shown in **Figure 4.5a**, a large-area green tape of LLZ:AlTa was formed, meaning that the amount of the binder MC had reached the minimum required value to binding all the ceramic powders in this tape. The weight ratio of ceramic powder LLZ:AlTa to the binder MC was fixed at 15:1 in the case of optimizing the binder/plasticizer-system. However, this dried green tape was rigid and broken in the middle. Meanwhile, it had reverse curling so that the edges of the green tape rolled downwards. These phenomena indicate the shortage of plasticizers in the green tape. There are two plasticizers used in the slurry, one is glycerol and the other is PEG. Glycerol is a single molecule substance that serves as the lubricant here to help the release of the green tape from the substrate after drying. Additionally, glycerol can also help keeping the flexibility of the green tape after long-term storage. In principle, water itself is a lubricant, too. The fresh green tapes are often flexible, but they become rigid after prolonged storage due to the evaporation of water. In this case, glycerol, which is much less volatile than water, is an ideal replacement, so that the shelf life of the green tapes can be extended. The other plasticizer PEG used here is PEG400, which is an oligomer with molar mass ~400 g mol^{-1}, and serves as the softener to make the green tape flexible via the interaction with the binder. Therefore, in the next test, the amounts of both

glycerol and PEG were doubled (Entry 2 in **Table 4.1**), but the result green tape with curling edges was still rigid. Hence, the amounts of plasticizers were further increased (Entry 3 in **Table 4.1**), and a flexible green tape was obtained. However, a lot of long cellulose fibers appeared at the surface of the tape (**Figure 4.5b**), indicating the possible shortage of softener *i.e.* PEG. Thus, more PEG was added in the next trial, giving the weight-ratio of MC:glycerol:PEG reached 1:4:4 (Entry 4 in **Table 4.1**). As a result, a flexible green tape with a smooth surface was obtained as shown in **Figure 4.5c**.

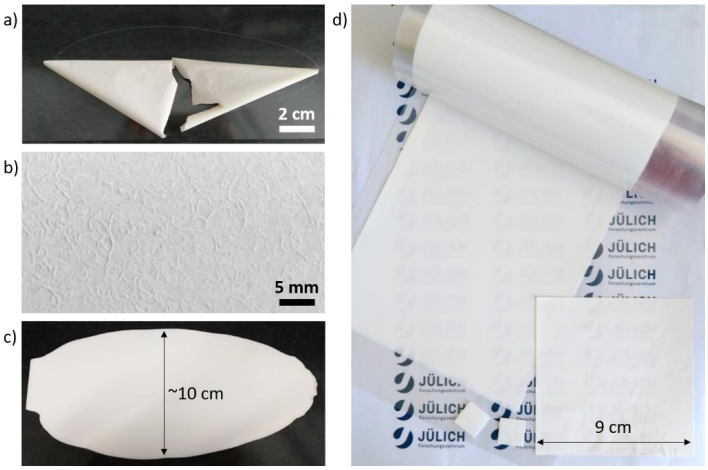

Figure 4.5 Photographs of LLZ:AlTa green tapes with different weight-ratio of MC:glycerol:PEG: a) 1:2:1; b) 1:4:2; c) 1:4:4. And d) photograph of the green tapes (size of the small square tape: 1.5 cm × 1.5 cm; size of the large square tape: 9 cm × 9 cm)

Afterwards, the ceramic loading in the slurry was investigated by fixing the weight-ratio of MC:Gly:PEG at 1:4:4 and stepwise increasing the portion of LLZ:AlTa powder. When the weight-ratio of LLZ:AlTa to MC increased from 15:1 to 120:1 (Entry 4-9 in **Table 4.1**), a flat flexible green tape with smooth surface was always obtained. Until this value reached 140:1 (Entry 10 in **Table 4.1**), the green tape became brittle, and could not be peeled off from the casting substrate entirely, indicating that this high ceramic loading already exceeded the binding ability of the used

MC in the slurry. Therefore, the final optimized slurry composition is (LLZ:AlTa):MC:Glycerol:PEG = 120:1:4:4.

Table 4.1 Optimization of the slurry composition (in weight ratio) for tape-casting LLZ:AlTa

Entry	LLZ:AlTa	MC	Glycerol	PEG	Appearance of Green Tapes
1	15	1	0.5	0.25	Reverse curling; broken in the middle; rigid
2	15	1	1	0.5	Curling; cellulose fibers on the surface; rigid
3	15	1	4	2	Flat; cellulose fibers on the surface; flexible
4	15	1	4	4	Flat; smooth surface; flexible
5	40	1	4	4	Flat; smooth surface; flexible
6	60	1	4	4	Flat; smooth surface; flexible
7	80	1	4	4	Flat; smooth surface; flexible
8	100	1	4	4	Flat; smooth surface; flexible
9	120	1	4	4	Flat; smooth surface; flexible
10	140	1	4	4	Flat; smooth surface; brittle

After the slurry composition was optimized, an up-scaling production of the LLZ:AlTa green tapes was demonstrated. The meter-long green tape with a width of *ca.* 13 cm, as shown in **Figure 4.5d**, was soft and flexible, which can be easily cut into desired sizes and shapes for the subsequent sintering step. Through controlling the height of the doctor blade, the thickness of green tapes can be varied from 60 to 140 μm. Although the slurry was prepared as foam free, the green tapes still exhibit certain porosities created by the evaporation of solvent. Therefore, it is necessary to laminate and compress the green tapes to increase their green density[b].

4.2 Sintering of Garnet Solid Electrolyte Layers

In the TG analysis of the green tape several steps with weight loss were observed (**Figure 4.6**). MS was applied to identify the source of each weight loss step. The MS curves corresponding to H_2O (m/z = 18) and CO_2 (m/z = 44) are presented in **Figure 4.6** as well. The remaining water in the

[b] green density: the volumetric mass density of the ceramic part in a green body. It is defined as the mass of the ceramic part divided by the geometric volume of the green body.

green tapes starts to evaporate at around 50 °C. The weight loss at the temperatures between 150 and 620 °C is about 15%, which is close to the total organic content in the green tapes, indicating that all organic additives (binder and plasticizers) are burned out at this stage (debinding stage). The water peak starts at 400 °C could be related to the extraction of H from the protonated garnets. The CO_2 evolution is observed between 650 and 900 °C, which can be assigned to the decomposition of Li_2CO_3 present on the surface of the LLZ:AlTa powder (as evident from **Figure 4.1**). No further weight loss was observed beyond 900 °C. For the final densification the tapes were sintered at a temperature of 1175 °C with 4 h dwell time, which was shown to be the optimum sintering temperature reported in the previous work.[168]

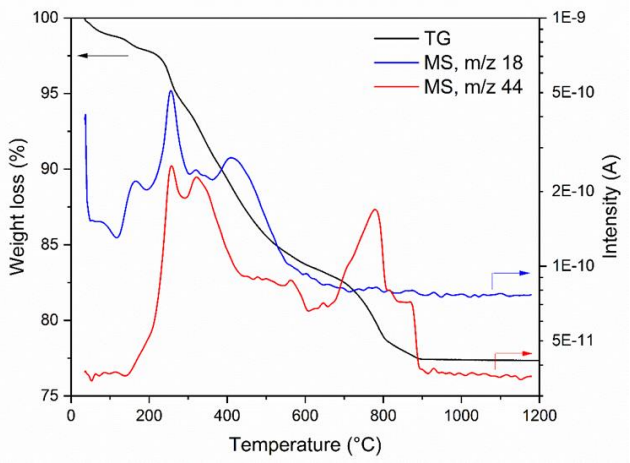

Figure 4.6 Thermal analysis TG-MS of garnet LLZ:AlTa green tapes.

Various substrate materials, including neat MgO plates, sintered garnet pellets, and MgO plates with garnet coating, were tested for sintering the garnet tapes in closed alumina crucibles, as shown in **Figure 4.7**. Due to its good chemical stability with LLZO, MgO is commonly used as substrate or crucible material for sintering garnets.[219] In this case, the MgO plate was placed in an alumina crucible with some LiOH powder on the bottom. LiOH is used here to compensate the Li-loss of LLZ:AlTa during sintering. After a sintering procedure at 1175 °C for 4 h, the white

MgO turned pinkish (**Figure 4.7a**), which could be attributed to the absorption of Li-containing species. Unlike other reports, the prepared garnet tapes stuck on the MgO plate. A possible reason could be that some Li-species condensate below the tapes in the cooling stage. The same result was also obtained when a polished, sintered (1185 °C, 2 h) garnet pellet was employed as sintering substrate. The garnet tapes merged well with the pellet as shown in **Figure 4.7b**. The third attempt was to coat a layer of LLZ:AlTa on the MgO plates, which was subsequently calcined at 1185 °C for 2 h. As the coating layer is porous and not as flat as a polished garnet pellet, the to-be-sintered garnet tapes have only point contact to this coating later, so that the tapes are rarely stuck on this kind of substrate. As shown in **Figure 4.7c**, two of such coated MgO plates were assembled as following: the coated surfaces are facing each other and four small alumina ceramic fragments are placed on the corners playing the role of space holders in order to prevent the upper MgO plate from pressing the tapes in the center.

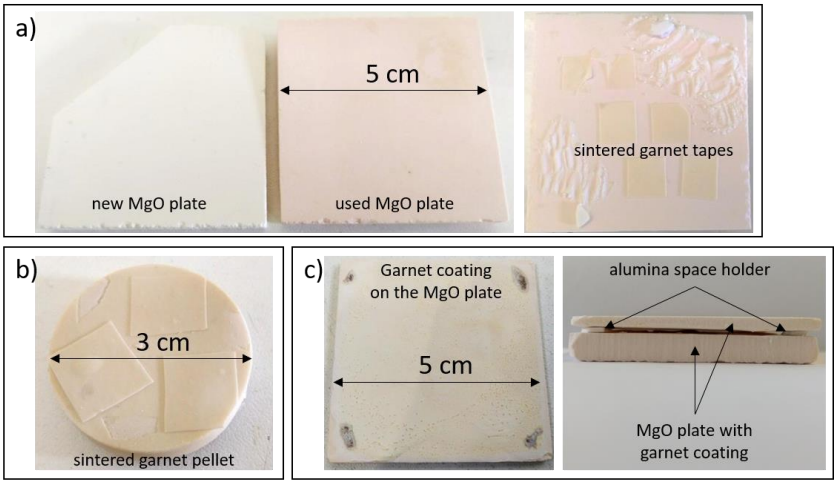

Figure 4.7 Different types of substrates for sintering garnet tapes. a) neat MgO plates; b) sintered garnet pellets; c) MgO plates with garnet coatings, and the set-up for sintering composed of such coated MgO plates and alumina space holders.

The sintering assembly was placed in a closed alumina crucible. Certain amount of LiOH powder was added around the sintering assembly inside the crucible to create a Li_2O atmosphere at high temperature and prevent the Li loss from tapes. The garnet tapes were sintered at 1175 °C for 4 hours. The fresh sintered sheets of LLZ-air show a yellowish color, as shown in the inset of **Figure 4.8a**. The sintered thin sheets have a thickness of ~150 µm the apparent density of approx. 90% (**Figure 4.8c**). The yellowish color of LLZ-air can be attributed to an impurity layer on the surface, which can be seen clearly in the BSE-SEM image (**Figure 4.8a**), showing a phase in dark color. This observation is in agreement with what Li *et al.*[134] was observed. This impurity phase is identified as Li_2CO_3 by XRD showing diffraction peaks at 21° and 24° but with quite low intensity in the pattern (**Figure 4.8d**). A surface sensitive Raman spectroscopy was used to confirm the existing of Li_2CO_3, which is indicated by the strong band at 1090 cm^{-1} originated from the CO_3^{2-} symmetric stretching vibration of Li_2CO_3 (**Figure 4.8e**).[220] Since the Li_2CO_3 in the synthesized powder as well as the one in the green tapes formed during drying has been thermally decomposed during the sintering at elevated temperature according to the TG results, it is reasonable to suggest that this impurity layer was formed during the cooling process in ambient atmosphere.

The presence of the Li_2CO_3 passivation layer on the surface of sintered LLZO sheet is disadvantageous as it is known to increase the interfacial resistance between garnet and lithium metal.[70] Li_2CO_3 layer can be removed by annealing in Ar.[104] After annealing in Ar, the obtained free-standing garnet solid electrolyte LLZ-Ar is partially transparent with color in white (shown in the inset of **Figure 4.8b**), indicating the successful removal of the impurities. SEM image (**Figure 4.8b**) reveals a clean surface of LLZ-Ar, and there are no diffraction peaks in XRD (**Figure 4.8d**) or Raman bands (**Figure 4.8e**) related to Li_2CO_3. ICP-OES reveals the final composition of the solid electrolyte LLZ-Ar close to the stoichiometric composition (**Table 4.1**). It should be noted however that the freshly sintered tapes in the process are carbonate-free and the Li_2CO_3 layer is formed during the cooling step in ambient atmosphere. Therefore, an additional annealing step can be avoided by performing sintering in a dry room or switching the atmosphere during the cooling step.

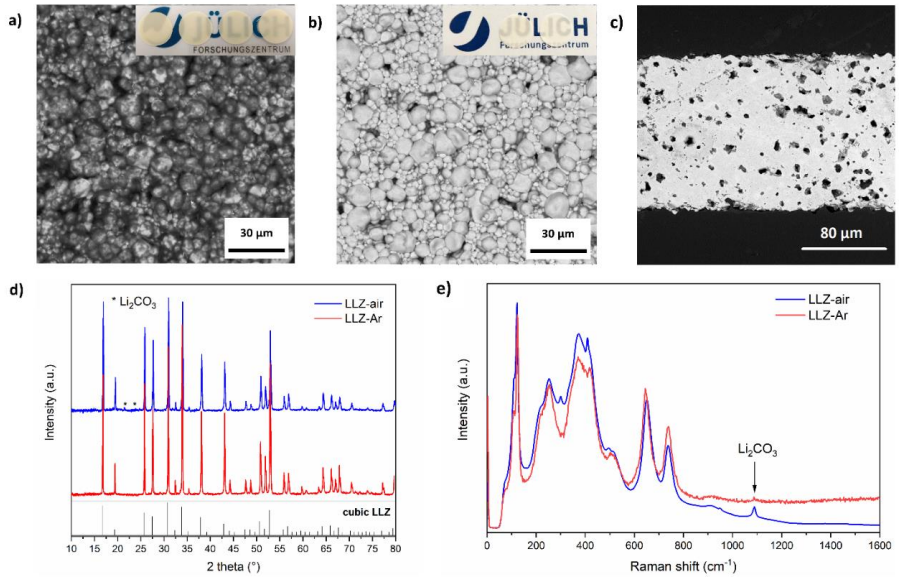

Figure 4.8 a) Surficial SEM image of LLZ-air (inset: photograph of LLZ-air, size: ca. 11 mm in diameter); b) surficial SEM image LLZ-Ar (inset: photograph of LLZ-Ar, size: ca. 11 mm in diameter); c) cross-sectional SEM image of LLZ-air; d) XRD patterns of LLZ-air and LLZ-Ar; e) Raman spectra of LLZ-air and LLZ-Ar.

Some tapes were also sintered with a prolonged dwell time up to 10 hours. The obtained garnet discs show mottled patterns in ivory color through the entire sintered body, while the remaining parts appear translucent as the LLZ-air samples sintered for 4 hours (**Figure 4.9a**). The BSE-SEM images reveal that the mottled patterns are composed of small garnet grains and some side phases (dark regions in **Figure 4.9b**), whereas the translucent parts are mostly large garnet grains with the sizes over 200 µm (bright regions in **Figure 4.9b**). This inhomogeneous grain size distribution exists not only on surface but also in the center of the discs. From the cross-sectional view, we can see that the large-size grains are fully dense, containing only very tiny closed pores (**Figure 4.9c**), while the small grains agglomerate at the boundaries among those large grains and separate them from each other (**Figure 4.9d**). The regions filled with the small grains are obviously not densified, which explains why it is not translucent in these areas. The EDS mappings, both on the surface and the cross-section, indicate high concentration of Mg element around the small

grains (**Figure 4.9e-f**). This Mg element is supposed to come from the MgO substrate. While MgO is unreactive with garnets, its impact on the sintering behavior of garnets is unclear. Huang *et al.* intentionally mixed MgO nanopowder with Ta-substituted LLZO for sintering, and found that the MgO phase locating on the surface of LLZO particles significantly restrained the grain growth of LLZO.[221, 222]

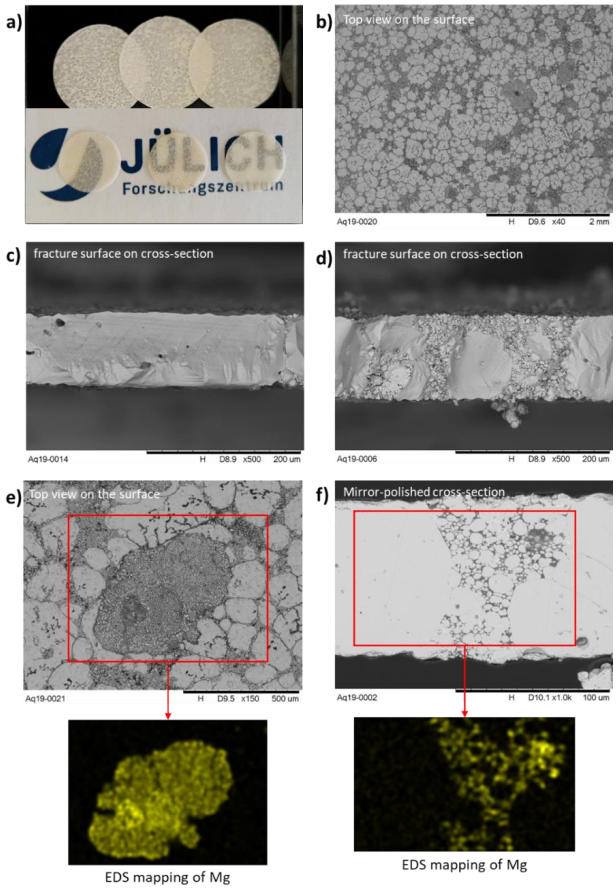

Figure 4.9 Mg diffusion from the substrate into garnet tapes which are sintered at 1175 °C for 10 h. a) Photograph of sintered garnet separators; b) Top-view SEM image on the surface of the garnet separator; c, d) SEM image of the fracture surface of the garnet separator; e) EDS mapping of the surface of the garnet separator; f) EDS mapping of the polished cross-section of the garnet separator.

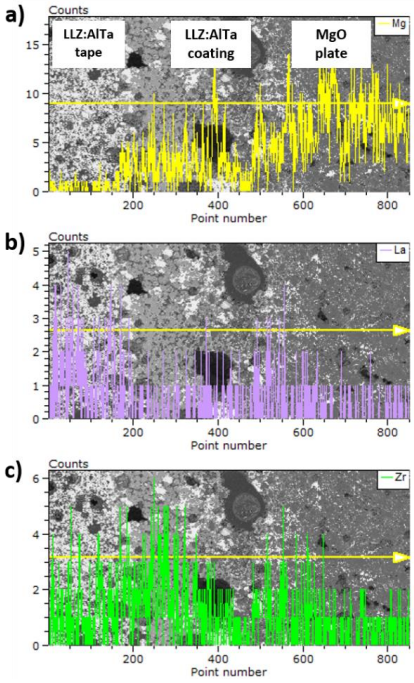

Figure 4.10 EDS line scans of a) Mg, b) La, and c) Zr of a MgO plate with LLZ:AlTa-coating after multiple uses, having a LLZ:AlTa tape merged on the top after sintering. The background is a BSE-SEM image thereof.

After multiple uses, the LLZ:AlTa coating degraded and lost the ability to avoid the adhesion of garnet samples on this substrate. LLZ:AlTa tape can merge with the coating layer as shown in the cross-sectional SEM image (**Figure 4.10**). The LLZ:AlTa tape region appears brighter in the BSE-SEM image because it is a La- and Zr-rich phase which have stronger BSE intensities, while the MgO region shows much darker due to the low BSE intensity of Mg. In between there is a layer with large pores, where the LLZ:AlTa coating layer locates, showing a mixture of bright and dark particles. The EDS line scans show the intensity gradient of Mg, La, and Zr across these three layers (**Figure 4.10a-c**). In the direction from the LLZ:AlTa tape via the LLZ:AlTa coating layer to the MgO plate, the intensity of Mg exhibits a significant increasing trend. Mg can be hardly found in the LLZ:AlTa tape, and has the strongest intensity in the MgO plate as expected, but it also shows weak signals in the LLZ:AlTa coating layers, indicating its diffusion. In contrast, La is mostly found

in the LLZ:AlTa tape and in some minor area of the LLZ:AlTa coating, whereas Zr shows almost the same strong intensities in these two layers. Neither La nor Zr is found in the MgO plate. This means, the diffusion of Mg is an one-way migration, which could be correlated to the decomposition of LLZ:AlTa that losses La perhaps Li as well. These findings suggest that the LLZ:AlTa-coated MgO substrates should be regularly refreshed or replaced with new ones after multiple uses to avoid the migration of Mg into the sintered samples.

4.3 Effect of Water

To fully understand the effect of water in aqueous processing of garnets, the impact of the Li^+/H^+-exchange reaction was investigated. For that, samples were prepared to carry out ICP-OES and XRD measurements on all garnet samples for each step of the fabrication procedure: 1) starting powder “LLZ:AlTa”, 2) solid filtrated from water-based slurry “LLZ-slurry”, 3) the green tape “LLZ-green”, 4) the sintered “LLZ-air” and “LLZ-Ar”. Lattice parameters for cubic LLZ were calculated from Rietveld refinement of the respective XRD data (**Figure 4.11**). The obtained results of elemental compositions from ICP-OES and lattice parameters as well as corresponding phase contents from Rietveld refinement are compiled in **Table 4.2** and **Table 4.3**, respectively.

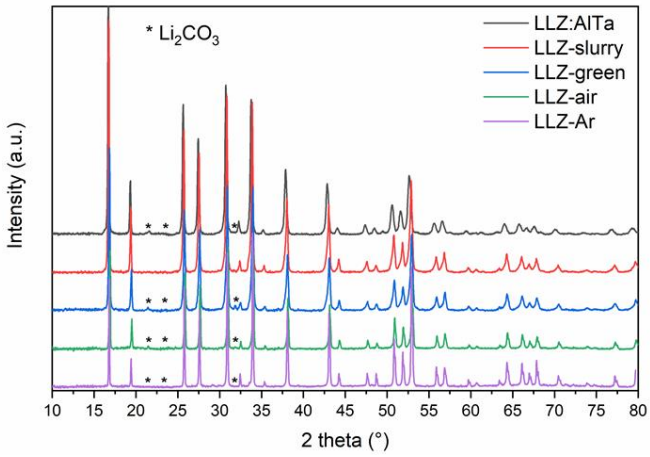

Figure 4.11 XRD patterns of garnet samples from each step of fabrication procedure. The Rietveld refinements were conducted based on these XRD data.

Table 4.2 Elemental analysis of garnet samples from each step of fabrication procedure

	Elemental Content (normalized to La)[a]				
	Li	Al	La	Zr	Ta
LLZ:AlTa	7.56	0.07	3.00	1.53	0.37
LLZ-slurry	4.42	0.07	3.00	1.53	0.37
LLZ-green	7.56	0.08	3.00	1.53	0.37
LLZ-air	6.72	0.08	3.00	1.53	0.37
LLZ-Ar	6.40	0.08	3.00	1.52	0.40

[a] Target composition: $Li_{6.45}Al_{0.05}La_3Zr_{1.6}Ta_{0.4}O_{12}$

Table 4.3 Lattice parameters and phase analysis of garnet samples from each step of fabrication procedure

	Garnet Phase #1		Garnet Phase #2		Li_2CO_3
	Lattice Parameter [Å]	Weight Percentage [%]	Lattice Parameter [Å]	Weight Percentage [%]	Weight Percentage [%]
LLZ:AlTa	12.950(2)	83	12.99(6)	15	2
LLZ-slurry	12.965(3)	58	13.01(2)	42	0
LLZ-green[a]	12.97(1)	34	13.03(1)	62	3
LLZ-air	12.946(2)	92	12.98(9)	6	2
LLZ-Ar[b]	12.944(1)	95	12.98(6)	3	1

[a] rest impurities in "LLZ-green": $La(OH)_3$ (1%); [b] rest impurities in "LLZ-Ar": $La_2Zr_2O_7$ (< 0.5%) and La_2O_3 (< 0.5%).

The elemental analysis reveals severe Li loss for LLZ:AlTa particles in "LLZ-slurry" by nearly one third when compared to the starting powder, indicating strong Li^+/H^+-exchange between garnet powder and the aqueous medium in slurry, which results in the dramatically increasing pH value of the slurry up to 12.5. On the other hand, the Li loss in the sintered samples is related to the expected Li evaporation at high temperature. Li_2CO_3 is hardly to find in "LLZ-slurry" because the carbonate in pristine powder as well as LiOH (the product of Li^+/H^+-exchange) was dissolved in water and left in filtrate. The solid "LLZ-slurry" after such severe Li^+/H^+-exchange could hardly further form new carbonate when exposure to air. It should be mentioned that "LLZ slurry" is not a step involved in the aqueous tape-casting process and is demonstrated here only for the purpose of investigation on Li^+/H^+-exchange. In comparison, I found an increasing portion of Li_2CO_3 in green tapes "LLZ-green", which can be attributed to the Li^+/H^+-exchange. These carbonates provide Li source for the Li-recovery in garnet at elevated temperature that I will discuss later in this section. Interestingly, two cubic phases of garnets were found in all samples

after the Rietveld refinement. One of them has a smaller lattice parameter around 12.95 Å, noted as phase #1, and the other has a relatively larger lattice parameter over 13.00 Å, noted as phase #2. Quantitative phase analysis results at different steps showed that the ratio of phase #1 decreases with the increasing ratio of phase #2 when LLZ:AlTa powder is immersed in water, whereas the phase #2 is almost completely converted into phase #1 upon sintering. Comparing the lattice parameters of both phases with literature data of Ta-substituted LLZO,[81] I can conclude that phase #1 is cubic phase LLZO stabilized by Ta-substitution without proton, while the phase #2 is stabilized by proton, in which the proton substitution leads to a lattice expansion.

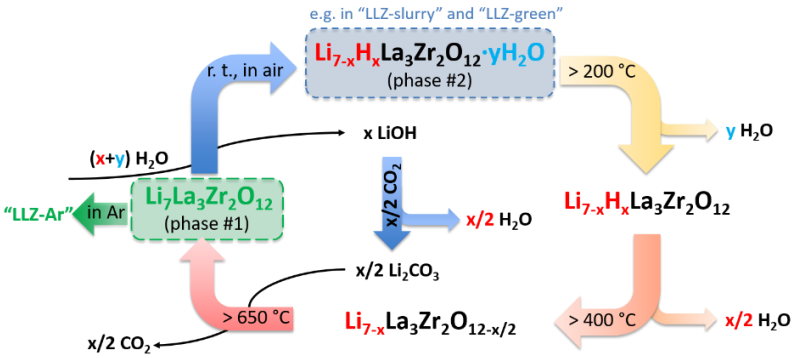

Figure 4.12 Schematic representation of the reversible phase transition mechanism between pure LLZO and hydrated LLZO based on ref. [94]. To simplify the expressions, Al and Ta are removed in this schematic.

The observed reversibility of this phase transition of water-treated LLZO upon heating can be explained by the mechanism proposed by Larraz *et al.*[94] and a schematic representation thereof is shown in **Figure 4.12**. Through the Li^+/H^+-exchange and the insertion of water molecules into LLZO structure, a hydrated cubic garnet is formed, which can be expressed as $Li_{7-x}H_xLa_3Zr_2O_{12}\cdot yH_2O$. This hydrated garnet loses the water of hydration between 200-250 °C to result in the cubic protonated garnet $Li_{7-x}H_xLa_3Zr_2O_{12}$, which further releases water between 400-450 °C, giving rise to a cubic garnet with O-vacancy $Li_{7-x}La_3Zr_2O_{12-x/2}$. The latter reacts with Li_2CO_3 at around 700 °C to form stoichiometric cubic $Li_7La_3Zr_2O_{12}$. The results clearly show that the garnet

stoichiometry is recovered at the end, though it is hydrated and protonated at the beginning. The only two other reported works regarding aqueous processing of LLZO, extra LiOH was intentionally added to suppress the Li^+/H^+-exchange reaction.[121, 123] However, my study clearly demonstrates that even without additional LiOH added to the slurry, the stoichiometric cubic LLZO can still be obtained after final heat treatment. Therefore, the developed water-based processing route is feasible to obtain pure cubic garnet SEs.

4.4 Electrochemical Performance of the Garnet Separator

The ionic conductivity of the "LLZ-Ar" sheets was determined by EIS measurement using a Li|LLZ-Ar|Li symmetric cell. The resulting Nyquist plot and its equivalent circuit are shown in **Figure 4.13a**. In the equivalent circuit, parallel elements of resistor (R) and constant phase element (CPE) are used to fit semicircles, while an inductor (L) is added due to wiring, and the fitting parameters are list in **Table 4.4**. We can see two semicircles that represent the resistances originating from the LLZ-Ar at high frequency (corresponding capacitance 4.93×10^{-10} F) and the LLZ-Ar/Li-interface at low frequency (corresponding capacitance 3.94×10^{-5} F), respectively. The bulk and grain boundary conductivities in polycrystalline ceramics measured by EIS usually exhibit capacitances in 10^{-12} F and 10^{-11}-10^{-8} F range, respectively.[223] Thus for the measurements, I assign the high-frequency semicircle with a capacitance in 10^{-10} F to the grain boundary resistance of LLZ-Ar (R2), while the bulk resistance is presented by the serial resistance R1 at high frequency. Thus, the total ionic conductivity of LLZ-Ar is 0.15 mS cm^{-1} at room temperature, which is comparable with reported garnet SEs fabricated by conventional (non-aqueous) tape-casting (**Table 2.2**). The sample-electrode interface usually exhibits a capacitance in the 10^{-7}-10^{-5} F range. Hence, the low-frequency semicircle with a capacitance in 10^{-5} F was attributed to the interfacial resistance between LLZ-Ar and Li metal.

Table 4.4 Fitting results of the EIS data

Element	*R1* [Ω]	*L1*	*R2* [Ω]	Q_{CPE1} [F]	n_{CPE1}	*R3* [Ω]	Q_{CPE2} [F]	n_{CPE2}
Value	143.5	2.43E-6	113.2	1.45E-9	0.95	248.4	7.89E-4	0.35
Error [%]	4.22	4.56	5.60	13.28	1.35	0.75	1.76	0.93

For application in SSLBs or other advanced battery concepts, the SE must show broad electrochemical stability window. To characterize the electrochemical stability, the LLZ-Ar layers were assembled in a Li|LLZ-Ar|In cell and CV measurements were carried out with a two-electrode set-up using Li as both counter and reference electrode. In the CV shown in **Figure 4.13b**, the reduction peak onset at 0.61 V *vs.* Li^+/Li can be assigned to the formation of Li-In alloy, while the corresponding oxidation peak onset at 0.62 V *vs.* Li^+/Li represents the de-alloying of Li from the formed Li-In alloy.[224] Another reduction peak near 0 V *vs.* Li^+/Li is the Li plating process together with subsequent non-redox Li diffusion into In forming the Li-In alloy. No other redox peaks are observed in the whole scan range, indicating electrochemical stability of the prepared SE. Meanwhile, the wide voltage window of up to 5 V *vs.* Li^+/Li, i.e. 4.4 V *vs.* Li^+/Li-In allows the use of high-voltage cathode materials in SSLBs in the future. Nevertheless, other operando and ex-situ characterization methods are still required to comprehensively determine the electrochemical stability window of the SE separator versus Li metal.[225, 226]

To further practically investigate the Li-conducting behavior of the prepared SE, Li stripping/plating tests were carried out with stepwise increasing current density (from 5 to 30 μA cm^{-2} with increment of 5 μA cm^{-2} per step) first to determine the critical current density and later with a constant one (10 μA cm^{-2}) to study the long-term cycling performance. 80 °C was chosen as the operation temperature because of a faster Li diffusion in SE and a higher ductility of the Li metal anode at this temperature. In the voltage profile under variable current densities (**Figure 4.13c**) it is found that the Li|LLZ-Ar|Li symmetric cell can cycle steadily up to a current density of 15 μA cm^{-2} (with some polarization) whereas increasing the current density further to 20 μA cm^{-2} leads to a short circuit most likely caused by dendrite formation. Although this critical current density value is still far away from practical application and some reports show 1-2 orders of magnitude higher ones,[114, 121] it is still in the range of reported operational current densities of ASSLBs with dense, free sintered garnet SE separators.

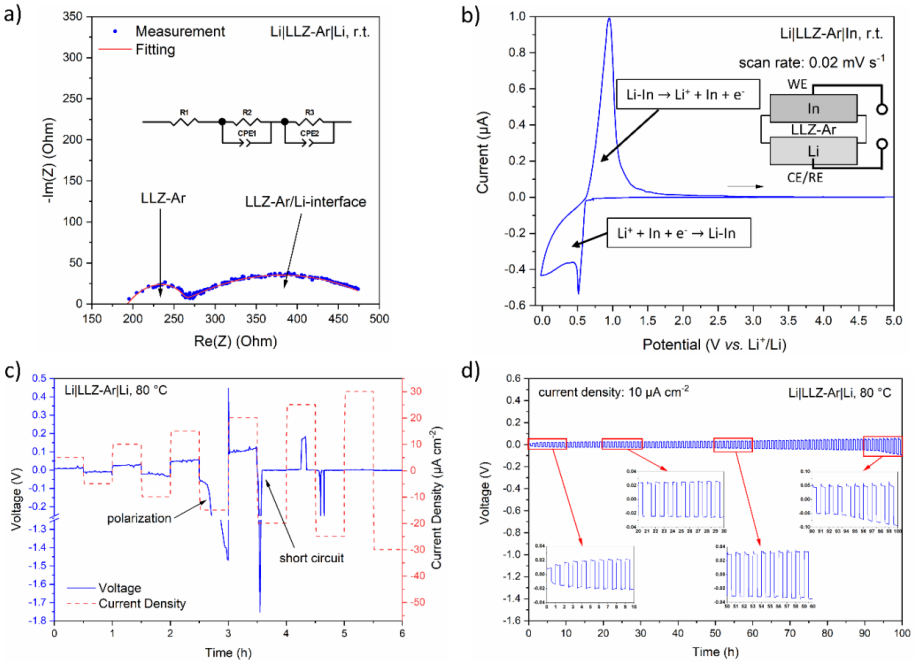

Figure 4.13 a) Nyquist plots of a Li|LLZ-Ar|Li symmetric cell measured at r.t. (inset shows the equivalent circuit for fitting, where R is resistor, L is inductor and CPE is constant phase element); b) CV curve of a Li|LLZ-Ar|In cell measured at room temperature (inset schematically represents the test cell for CV with WE: working electrode, CE: counter electrode and RE: reference electrode); c) Voltage profile of a Li|LLZ-Ar|Li symmetric cell under variable current densities at 80 °C; d) Galvanostatic cycling of a Li|LLZ-Ar|Li symmetric cell at 10 μA cm^{-2} at 80 °C.

It seems that the low Li self-diffusion in the Li metal results in poor contact between garnet and metal anode, leading to fast dendrite formation.[13, 168, 227] Therefore, a safe current density for the prepared SE was set to 10 μA cm^{-2}, which was then applied for the long-term cycling. The obtained cycling profile (**Figure 4.13d**) shows the steady Li-conducting performance over 100 hours without short circuit, though slightly increased voltages after 90 hours is observed as a consequence of increasing Li/SE-interface resistance due to the roughness on the SE surface. Since I did not do any Li/SE-interface modification, the observed critical current density as well as the Li-stripping/plating performance could depend rather on the Li/SE-interface contact than on

the conductivity of SE itself. The Li foils in these demonstrated cells were all attached by hand, which may lead to large difference in the Li/SE-interfacial resistance from one cell to another. To avoid this issue, it would be better to deposit Li onto the SE by for instance an evaporator.

4.5 Summary

In this chapter, a water-based tape-casting process using eco-friendly binders to fabricate thin free-standing garnet SE separator was successfully developed. It is shown that the occurring Li^+/H^+-exchange reaction is completely reversible in this process and enables the formation of stoichiometric Ta- and Al-substituted LLZO with cubic phase. The obtained garnet SEs shows a total ionic conductivity of 0.15 mS cm^{-1} at room temperature and is (electro-)chemically stable against lithium metal within the boundaries of the experiment. Therefore, the developed water-based tape-casting process paves a green way to fabricate free-standing garnet SE separator, which is suitable to be employed in SSLBs with SE-supported configuration or in other advanced Li-battery having Li-metal anodes. Further work needs to be done on modification of SE/Li-interface to achieve a higher applicable current density and better long-term cycling performance.

5 Water-Based Fabrication of $LiFePO_4$ Cathodes for Garnet-Supported Solid-State Lithium Battery

This chapter is based with modification on the publication 'Water-based Fabrication of a $Li|Li_7La_3Zr_2O_{12}|LiFePO_4$ Solid-state Battery – Toward Green Battery Production' by Ye et al. It was published during the thesis and reprinted (adapted) with permission from [228]. Copyright (2022) American Chemical Society

5.1 Impact of Solvents

In conventional electrode manufacturing by tape-casting, hazardous organic solvents are generally used.[229] Alternative sustainable solvents are required for future environmental friendly processing. To investigate the impact of different solvents on PEO, three solvents are chosen: water (H_2O), bio-ethanol (EtOH), and acetonitrile (ACN). ACN is the commonly used organic solvent for PEO preparation in previous reports,[181] while water and bio-ethanol are selected in this study as possible replacement of ACN to allow a sustainable industrial processing. Firstly, PEO was dissolved in these solvents to prepare a 50 g L^{-1} solution. **Figure 5.1** shows that PEO has a lower solubility in EtOH and is only thoroughly dissolved when slightly warmed to approx. 50 °C, while it is well dissolved in both water and ACN at room temperature. According to Ho *et al.*, PEO tends to crystalize into a lamellar structure in EtOH at room temperature but completely dissolve in EtOH only above the melting point.[230]

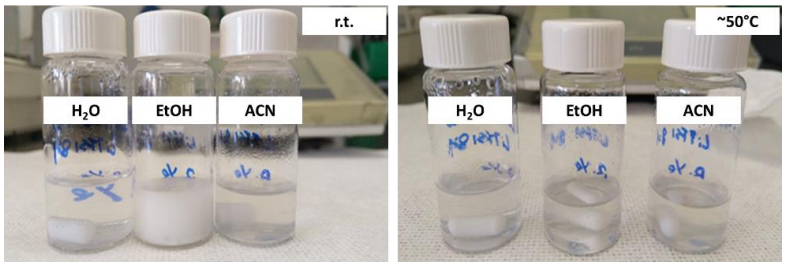

Figure 5.1 Digital photographs of PEO solutions in water, bio-ethanol and acetonitrile at room temperature (left) and at 50 °C (right).

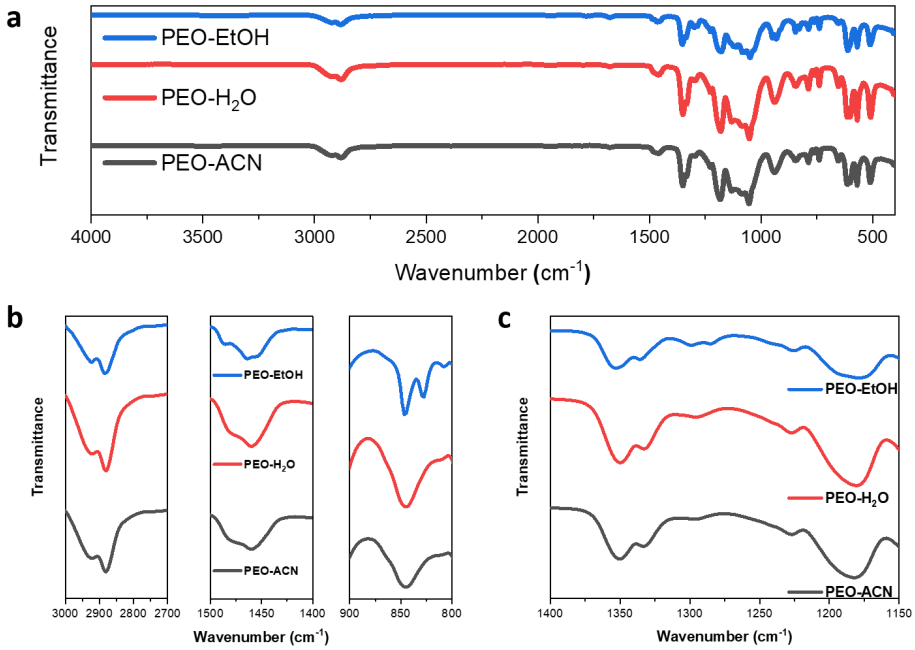

Figure 5.2 ATR-FTIR spectrum of PEO membranes prepared from H_2O-, EtOH- and ACN-based solutions. a) Entire measured spectra; Selected regions of b) C-H bands and c) $TFSI^-$ anion.

The PEO solutions were cast and dried to form membranes. The structure of the PEO membranes prepared from these three solutions were studied by ATR-FTIR. As shown in **Figure 5.2a**, no peak is observed around 3500 cm^{-1} in all three samples, indicating the absence of residual water, which means the vacuum drying removed all traces of water.[184] The strong C-H stretching bands at 2920 and 2880 cm^{-1} are similar in all three samples, but the C-H bending bands at 1470 cm^{-1} and the C-H rocking bands at 840 cm^{-1} are different (**Figure 5.2b**). These two bands show splitting solely in the EtOH sample, whereas the other two samples have only one peak each. Such splitting of C-H bands in the fingerprint region indicates the presence of crystalline phases within PEO in the EtOH sample, which can be attributed to the crystallization behavior of PEO in EtOH.[230] The samples prepared in water and ACN are amorphous, which has usually higher ionic conductivity than the crystalline phase.[231] The band splitting occurs at 1290 and 1180 cm^{-1} again in EtOH

sample, whereas broad single peaks appear in the other two (**Figure 5.2c**). Two splitting peaks represent two forms of LiTFSI in the polymer system: free ion pairs (Li^+TFSI^-) and aggregates. In the case of samples prepared in water and ACN, ion pairs are predominant.[231] The ion pairs have higher mobility than the aggregates in the polar polymer system because the formation of ion pairs reduces the solvent-salt interaction. For the EtOH sample, the occurrence of aggregation lowers the mobility of LiTFSI due to the enlarged sizes and charges.[231] The aggregates should also show twin peaks at 1351 and 1347 cm^{-1}, however, the latter one is hardly distinguished from interfering PEO bands.

Based on these results, EtOH shows inferiority to water and ACN for the application as the solvent in PEO processing. EtOH seems to induce the crystallization of PEO membranes as shown by ATR-FTIR, thus it is not a capable candidate for replacing ACN. In contrast, there is no significant difference between the PEO samples prepared in water and ACN. Therefore, water was chosen for further sustainable fabrication of LFP-PEO cathode in this work.

PSD of the LFP powder was analyzed by laser light diffraction. As shown in **Figure 5.3a**, the PSD exhibit a bimodal curve, giving D_{10} value of 0.27 µm, D_{50} value of 6.97 µm and D_{90} value of 19.1 µm. About 30% of the powder are smaller than 1 µm, and almost half of the powder larger than 10 µm. The morphology of the LFP powder was further investigated by SEM. The SEM image shows three different shapes of the LFP particles (**Figure 5.3b**). The first shape is LFP primary particles, corresponding to the first peak smaller than 1 µm in the PSD measurement. The second shape is the well-designed sphere-like LFP secondary particles, which have broad size distribution from 5 µm to 30 µm as observed in the SEM image. The last type is other non-sphere-like agglomerates ranging from submicrons to several microns. Such various morphology of the particles, especially huge difference in surface area, will strongly affect the interaction between LFP particles and PEO polymers during the cathode tape preparation. Smaller particles have larger specific surface area. Hence, more PEO is needed to cover the surface of the smaller LFP particles, while less PEO already binds large LFP spheres sufficiently.[232] From our own tape-casting experience, the particle size is correlated to the viscosity of the slurry. Normally, finer particles result in higher viscosity. On the other hand, although spherical LFP have higher tapped density than loose particles themselves,[233] large porous volumes between LFP spheres remain, and

filling them consumes a lot of PEO. For the case of the LFP particles with bimodal particle distribution, small LFP particles can fill the pores between large LFP spheres and lead to higher tapped density.

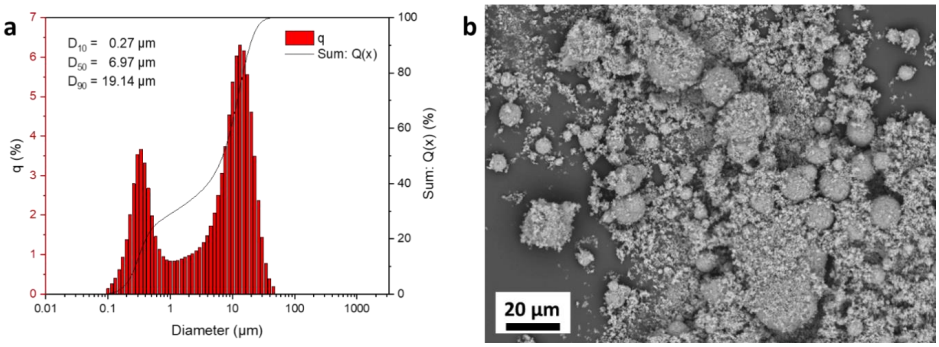

Figure 5.3 a) PSD and b) BSE-SEM image of the received LFP powder.

The influence of water on the phase purity of LFP was studied by XRD (**Figure 5.4**). In the as-received LFP powder, a Li_3PO_4 as secondary phase is found, which is a side product during the synthesis. Exposing the LFP powder to water generated no additional impurities. However, there was actually a thin white layer on the top surface of the dried LFP powder. It might be some amorphous substances un-detectable by XRD. Zaghib *et al.* also reported this phenomenon in water-treated LFP, and they suggested that this white top layer could be LiOH and Li_2CO_3 due to slight delithiation of LFP in water.[38] Nevertheless, these are merely due to the prolonged contact with water. In fact, the water involved in the cathode fabrication is evaporated much faster because of the low thickness of cathode layers and the bottom heating system, so that the contact time of LFP with water can be shortened to one hour or less. Hence, this slight delithiation effect can be neglected in the processing of cathode fabrication.

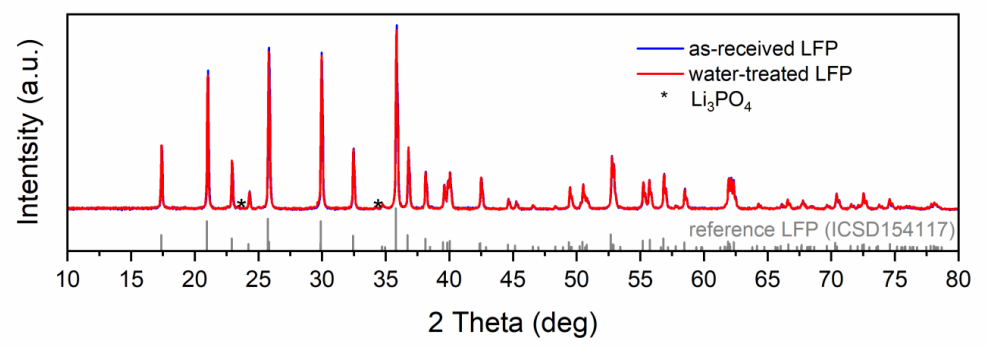

Figure 5.4 XRD patterns of the as-received LFP powder and the water-treated LFP powder.

5.2 Impact of Composition

Cathodes with three different LFP-PEO ratios were prepared: The C1, C2 and C3 cathodes had a LFP-PEO volume ratio of 2:1, 1.5:1, and 1:1, respectively. The slurry for tape-casting shows a gel-like fluid behavior and the dried cathode tape has a homogeneous distribution of the solid contents as shown in **Figure 5.5a**. The SEM images in **Figure 5.5b** show the microstructure of prepared LFP-PEO composite cathodes. The sphere-like LFP particles are distributed and embedded into the PEO polymer matrix. A higher volume ratio of PEO on the surface of the cathode tape is observed, which is beneficial for attaching the LLZO separator for the full cell fabrication. There are, however, many large cracks in the C1 cathode, whereas only a few minor cracks appear in C2 and C3 cathodes. This observation suggests that the amount of PEO in C1 is inadequate to bind LFP and carbon particles. In addition, the exfoliation is observed in C1 cathode, while both C2 and C3 cathodes are well coated on the Al foil. Hence, an LFP:PEO ratio of 1.5:1 or 1:1 is essential to maintain sufficient interfacial contact in the LFP-PEO cathode.

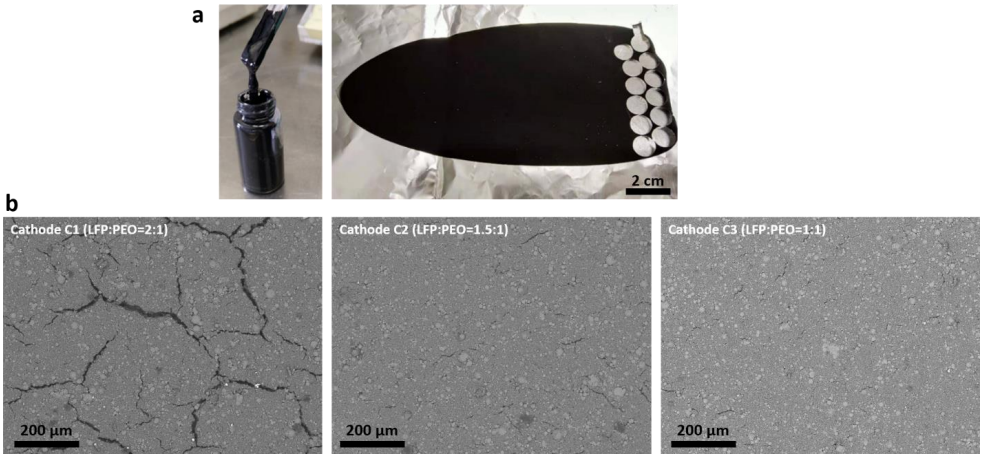

Figure 5.5 a) Photographs of the slurry for LFP-PEO cathode (left) and the dried LFP-PEO cathode C3 with the punched holes having a diameter of 1 cm (right); b) BSE-SEM images of LFP-PEO cathodes with varying LFP:PEO ratio (from left to right: C1, C2 and C3).

5.3 Electrochemical Performance of Li|garnet|$LiFePO_4$ Solid-State Lithium Batteries

The lamellar configuration of the SSLB employing the C3 cathode is exemplarily shown in **Figure 5.6** as SEM cross-section including the Ni current collector, the Li metal anode, the LLZO separator, and the LFP-PEO composite cathode as well as the Al current collector. The total thickness of the cell is about 270 µm, and the volume shares of Li, LLZO, LFP-PEO and Al are 37%, 39%, 17% and 7%, respectively. The Li foil is calendered by hand and the thickness is already reduced from the original 750 µm as purchased down to 100 µm. Since other commercial Li foils with the thickness of 50 µm are available, it is also possible to further lower the thickness of the anode here.[234]

The thin LLZO separator is fabricated by water-based tape-casting, which has an ionic conductivity of 0.15 mS cm^{-1} at room temperature. Compared to the sliced LLZO pellets that usually have a thickness ranging from 300 to 600 µm, this 105-µm-thick LLZO sheet has successfully reduced the thickness by at least two-thirds, which is greatly beneficial for reducing the total volume and

weight of the SSLBs and therefore improving energy density on cell level.[235, 236] Even thinner LLZO separators could further increase the energy density, but might not stop the dendrite formation.[110, 111]

The LFP-PEO composite cathode C3 demonstrated here has a thickness of 45 µm and a comparable LFP-loading with other reports in lab scale (2-3 mg cm^{-2}).[134, 135, 180, 181] The cathode loading, however, has to be increased for commercial applications. Hence, a thick cathode C3t with an LFP-loading of 9-10 mg cm^{-2} is prepared as well.

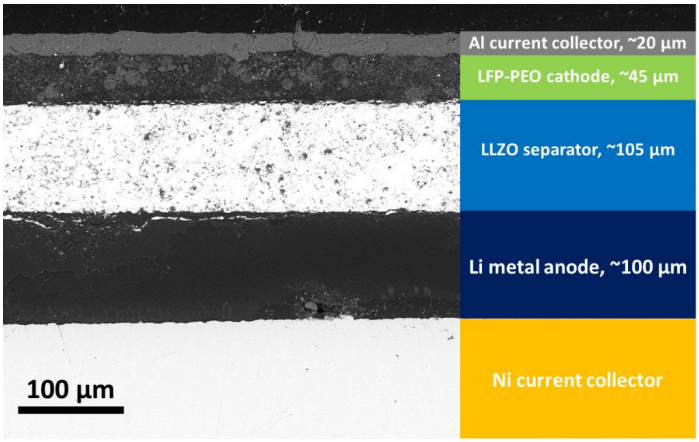

Figure 5.6 Cross-sectional BSE-SEM image of the Li|LLZO|LFP-PEO SSLB with the cathode C3.

Figure 5.7a shows the charge/discharge curves of cathodes C1, C2, and C3 at a current density of 10 µA cm^{-2}. The C2 and C3 cathodes have high specific capacities of 155 mAh g^{-1} and 149 mAh g^{-1}, respectively, whereas the C1 cathode has lower capacity with only 91 mAh g^{-1}. The low capacity of C1 is speculated for lacking of sufficient Li^+-conduction in the cathode due to the low PEO content and the cracks within the cathode that leads to the contact loss in some parts. This difference in PEO content also leads to the electrochemical performance varying greatly when the batteries are operated at higher current density. As shown in **Figure 5.7b**, the C1 cathode can hardly be charged or discharged at 50 µA cm^{-2}, having a large polarization especially for the

discharge and a low specific capacity of 35 mAh g^{-1} in the 1st cycle, followed with a quick decline of the capacity upon further cycling (**Figure 5.7c**). In contrast, both C2 and C3 cathodes exhibit stable cycling behavior with high coulombic efficiency nearly 99% in 50 cycles. The C3 cathode, due to its highest PEO content, achieves higher capacity (0.42 mAh cm^{-2}, *i.e.* 136 mAh g^{-1}) than the C2 cathode (0.31 mAh cm^{-2}, *i.e.* 112 mAh g^{-1}). The average capacity decay for the cathodes C2 and C3 are around 0.73% and 0.54% per cycle, respectively.

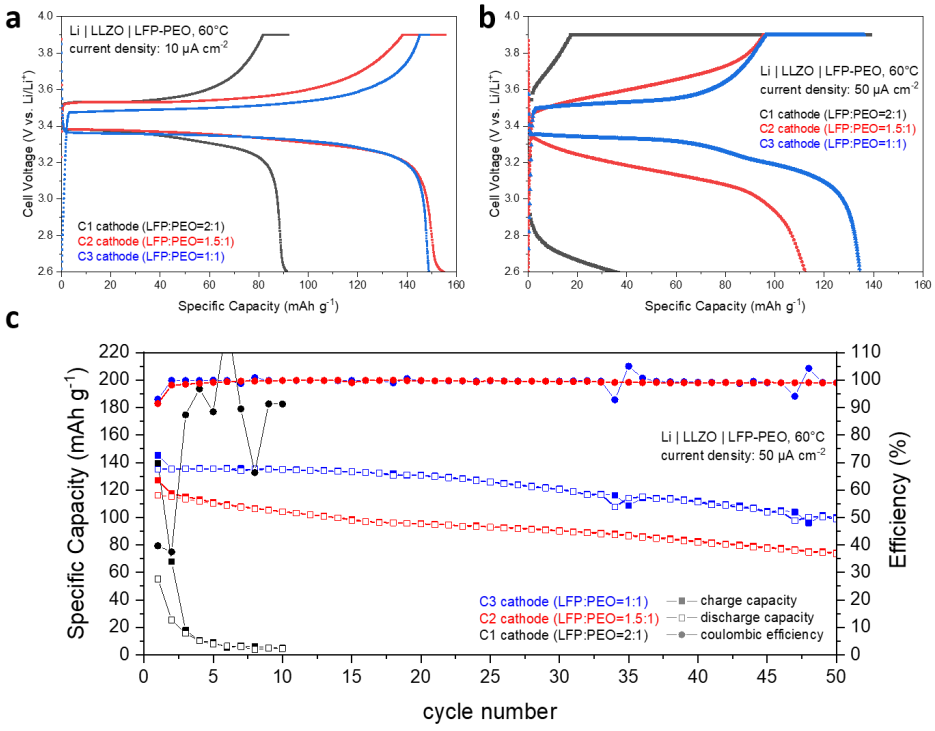

Figure 5.7 The electrochemical performance of SSLBs with LFP-PEO cathodes C1, C2 and C3: Charge-discharge curves at a) 10 μA cm^{-2} and b) 50 μA cm^{-2}; c) Long-term cycling performance at 50 μA cm^{-2}.

When the current density is increased to 100 μA cm^{-2}, the charge/discharge curves show decreasing capacities upon cycling. A short circuit due to Li dendrite growth in the 16th cycle is

observed (**Figure 5.8a**). The capacity decay in the first 4 cycles is small, and the cell provides a capacity around 0.33 mAh cm^{-2}. From the 5th cycle on, a second plateau at much lower discharge voltage appears, giving rise to the increasing polarization and capacity fading.

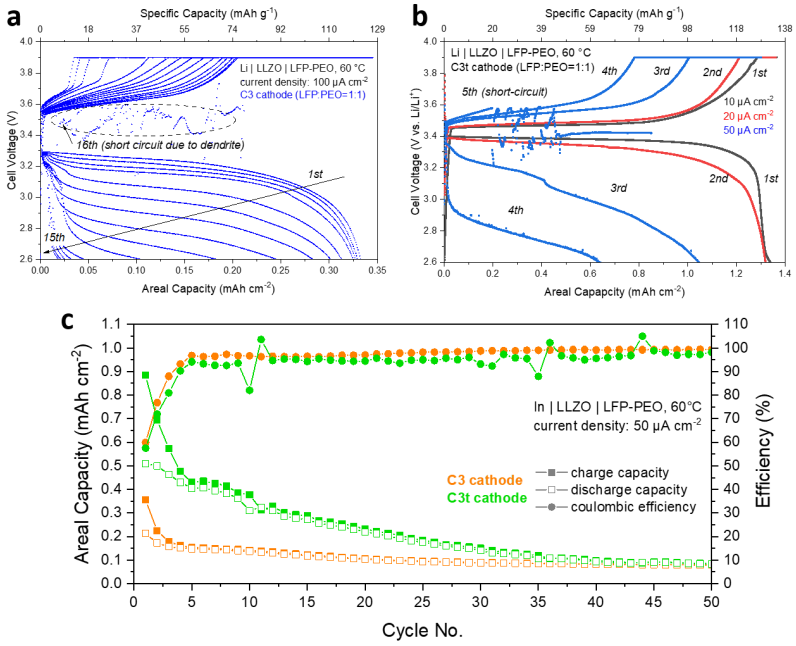

Figure 5.8 a) Charge-discharge curves of SSLBs with Li metal anode and LFP-PEO cathode C3 at the current density of 100 µA cm^{-2}; b) Charge-discharge curves of SSLBs with Li metal anode and LFP-PEO cathode C3t at current densities of 10, 20 and 50 µA cm^{-2}; c) Long-term cycling performance at 50 µA cm^{-2} of SSLBs with In metal anode and LFP-PEO cathode C3 or C3t.

Similar cycling behavior is observed in the SSLB containing the thick C3t cathode with high LFP-loading. As shown in **Figure 5.8b**, the discharge curves show plateaus at 3.4 V *vs.* Li/Li^+ when the SSLB is cycled at 10 and 20 µA cm^{-2}. The areal capacity is 1.34 and 1.32 mAh cm^{-2} for 10 and 20 µA cm^{-2}, respectively, and the specific capacity reaches 131 mAh g^{-1}, which is lower than the one of a thin cathode C3 at 10 µA cm^{-2}. It seems that some parts of the LFP are inaccessible for Li^+ in

the thick cathode (C3t), which is similar to the behavior of thick cathodes with ceramic electrolytes.[237] When the current density is increased to 50 µA cm^{-2}, the battery suffers severe capacity degradation. In the 3rd cycle, the battery is charged as expected for LFP, while the discharge curve shows no plateau anymore but a gradual decrease, indicating that the resistance might increase dramatically during discharging. In the 4th cycle, the charging plateau is higher than that in the 3rd cycle and the voltage reaches 3.9 V much earlier. The corresponding discharge curve shows large polarization, resulting in a much lower discharge voltage and the reduction of capacity from 1.04 mAh cm^{-2} (*i.e.* 102 mAh g^{-1}) to 0.64 mAh cm^{-2} (*i.e.* 63 mAh g^{-1}). In the next charging process, a short circuit occurs due to Li dendrite penetration through the LLZO separator.

With this respect, I hypothesize that this degradation might be related to the inhomogeneous plating/stripping behavior of Li metal anode. The voids at the LLZO/Li interface are expanded during discharging, giving rise to reduced contact area and thus enhanced polarization. When Li^+ is again deposited onto the Li foil during charging, the limited contact area and the low Li self-diffusion restrict the Li distribution so that the Li dendrites form along the LLZO grain boundaries from the contact points towards the cathode until the dendrites penetrate the entire separator and cause a short circuit.[238, 239] This failure occurs at a higher cycle counts in a low-capacity cell at high current densities, because the voids at the interface are not large after discharge and can be thus refilled more easily during charging. In the case of a high-capacity cell, such degradation at the interface is accelerated and intensified.

In order to mitigate the negative effect of Li anode on the long-term performance of the thick cathode, an indium metal anode is employed. Indium forms an alloy with Lithium, in which the lithiation reaction and the charge transfer are relatively faster than in lithium.[224] To evaluate the capability of an indium metal anode, the thin C3 cathode is initially tested as a reference. As shown in **Figure 5.8c**, the coulombic efficiency in the 1st cycle is as low as 60% and slowly increases afterwards to 97% in the following four cycles. The charge capacity drops from 0.36 mAh cm^{-2} for the 1st charge to 0.15 mAh cm^{-2} for the 5th cycle, while the discharge capacity drops from 0.21 mAh cm^{-2} for the 1st cycle to 0.15 mAh cm^{-2} for the 5th cycle. Such initial cycles with low efficiency and decreasing capacities were also observed in the Li-In|LLZO|LCO SSLBs in previous studies.[107, 168, 172, 240] Comparing this performance with the high reversibility of

the cell comprising Li metal anode (**Figure 5.7c**), I preliminarily conclude that there is an irreversible reaction in the formation of the Li-In alloy, which leads to the low efficiency and capacity decay in the initial cycles. The cell with the thick C3t cathode exhibits similar performance in the first 5 cycles: low efficiency and decreasing capacity. The difference is that the cell with C3t cathode continuously loses capacity afterwards and has an overall lower coulombic efficiency than C3 cathode. This dramatic capacity decay and low efficiency could be attributed to the cathode part. The possible cause could be the oxidative decomposition of PEO above 3.8 V *vs.* Li/Li^+ on a carbon-containing composite electrode,[241] which blocks the ionic transport at the cathode/electrolyte interface.[242] Additionally, the corrosion of Al current collector due to LiTFSI could also be the reason.[243] but the impact of the Indium anode should not be excluded at this point as well, for instance the poor wettability of In at the garnet surface[244], which needs further investigation. Nevertheless, the high-capacity cell equipped with an indium metal anode shows improved cyclability without dendrite-induced short circuit comparing to the one with a Li anode. Instead of directly attaching a bulk Indium foil as electrode, an Indium coating might be more suitable for interfacial modification.[139] Various coatings and designed microstructures for the solid electrolyte/anode interfacial modification[245] are under consideration to optimize the cycle stability. Further investigations need to be carried out in this respect.

Cell performances of several SSLBs consisting of ceramic separators and LFP cathodes in lab scale are summarized in **Table 5.1**. The presented environmentally friendly in water processed LFP-PEO composite cathodes reach the performance of conventionally processed ones, and shows the promising aspect of green processing. Moreover, the LLZO thin sheet developed by water-based tape-casting significantly reduces the separator thickness comparing to other ceramic pellets, and only the PEO-containing separators (*e.g.* LLZO-PEO hybrid membrane and neat PEO membrane) are thinner (50-70 µm). Although the $Li_{0.34}La_{0.56}TiO_3$ (LLTO) thin sheet, which is also fabricated by tape-casting, has a low thickness (41 µm) itself, it needs additional PEO membranes on both cathode and anode sides to modify interfaces, giving rise to a much higher total thickness of separator layer and more interfaces that lead to higher resistance and thus reduced electrochemical performance.[180] Furthermore, a proper anode modification is necessary for ceramic separators, especially for LLZO, to enable high current densities.[133]

Table 5.1 Comparison of SSLBs containing LFP-PVdF or LFP-PEO composite cathodes

Cathode (vol.-ratio of LFP:binder)	Solvent	LFP-loading [mg cm^{-2}]	Separator / Thickness [µm]	Anode modification	Current Density [µA cm^{-2}]	Cycles / Temperature	Capacity		Ref.
							Specific [mAh g^{-1}]	Areal [mAh cm^{-2}]	
LFP:PVdF (3.8:1)	NMP	1.2	LLZO / n.a.	none	10	100 / 60 °C	150	0.18	[175]
LFP:PVdF (1.3:1)	NMP	0.42	LLZO / 1000	Si	8	100 / r.t.	120	0.05	[176]
LFP:PVdF (1:1)	DMF	~1	LLZO / 500	LiPxOy	100	400 / 25 °C	122	0.12	[177]
LFP:PVdF (4:1)	IL	~2	LLZO / 1000	HCl	34	150 / 30 °C	143	0.29	[135]
LFP:PVdF:LLZO (1.12:1:1.88)	NMP	n.a.	LLZO-LiTFSI / 3-5	none	0.1C	100 / r.t.	160	n.a.	[247]
LFP:PEO (1:1)	NMP	~2	LLTO / 41	PEO	54	50 / 65 °C	145	0.29	[180]
LFP:PEO (1:1)	ACN	~2	LLZO / 600	Li-Si-N	340	100 / 60 °C	150	0.30	[181]
LFP:PEO (1:1)	DMF	~5	LLZO / 500	CPMEA	170	100 / 65 °C	130	0.65	[163]
LFP:PEO (1:1)	n.a.	3-5	LMZP / 350	none	100	50 / 60 °C	140	0.42-0.70	[182]
LFP:PEO (1:1)	DMF	2-3	LLZO / 300	C	100	50 / 65 °C	143	0.29-0.43	[134]
LFP:PEO (1.6:1)	ACN	70	LLZO-PEO / 70	none	100	10 / 60 °C	152	10.6	[183]
LFP:PEO (3.5:1)	H_2O	3.3	PEO / 50	none	185	210 / 60 °C	155	0.53	[187]
LFP:PEO (1:1)	H_2O	2.7	LLZO / 105	Au	50	30 / 60 °C	136	0.37	This work

CPMEA: cross-linked poly(ethylene glycol) methyl ether acrylate; LMZP: $Li_{1.2}Mg_{0.1}Zr_{1.9}(PO_4)_3$; n.a.: not available; r.t.: room temperature

5.4 Summary

The work in this chapter validates the sustainable and environmentally friendly fabrication of garnet-based SSLBs with LFP cathode. I demonstrated a water-based processing route for Li|LLZO|LFP-PEO SSLBs. Both the LFP-PEO composite cathode and the LLZO separator were fabricated in water, avoiding the harmful organic solvents commonly used in the conventional approach. The volume ratio of LFP:PEO is significant for the electrochemical performance as it controls the limiting Li^+-conductivity. Only for sufficiently high Li^+-conductivity achieved by high PEO loading, a good performance is observed even for 120-µm-thick cathodes. The prepared thin LFP-PEO composite cathode exhibits comparable performance as the ones prepared in organics, having a specific capacity of 136 mAh g^{-1} at the current density of 50 µA cm^{-2} in the first cycles. Moreover, the LLZO separator fabricated by water-based tape-casting significantly reduces the separator thickness so that an enhanced energy density is achieved on the cell level. However, high-rate operation and prolonging cycle life still remains challenging, especially for the thin LLZO separator. Hence, modifications on anode or application of other type anode material such as silicon (Si)[246] as well as an increased electrochemical stability of PEO is necessary to improve the long-term cycling stability and to prepare for commercialization of this 'green' battery type.

6 Water-Based Fabrication of $LiCoO_2$-Garnet Composite Cathodes for Garnet-Supported Solid-State Lithium Battery

This chapter is based with modification on the publication 'Aqueous Processing of $LiCoO_2$-$Li_{6.6}La_3Zr_{1.6}Ta_{0.4}O_{12}$ Composite Cathode for High-Capacity Solid-State Lithium Batteries' by Ye et al. It was published during the thesis and reprinted (adapted) with permission from [248].

6.1 Tape-Casting and Sintering of $LiCoO_2$-Garnet Composite Cathodes

A bulk LCO/garnet composite cathode has been demonstrated by Laptev *et al.* and Ihrig *et al.* using a FAST/SPS process.[107, 171, 172] This advanced sintering technique is a solvent- and additive-free, energy-efficient process. In my work, such free-standing composite cathodes are to be fabricated by water-based tape-casting using biopolymer binder. The benefits of the tape-casting over FAST/SPS is its easy scale-up and common use in industry.

Park *et al.* pointed out that an Al^{3+}/Co^{3+} interchange reaction occurring at the interface between LCO and Al-doped LLZO during the sintering at 700 °C.[169] Ihrig *et al.* also found that this Al^{3+}/Co^{3+} exchange reaction can take place during the electrochemical cycling as well.[240] Although the amount of Al^{3+} is rather low in those garnet phases, the loss of these Al^{3+} could already lead to the garnet phase transition from the high-conductive cubic phase into the low-conductive tetragonal phase at the interface towards LCO. In addition, other Co-containing amorphous layers could be formed between LCO and LLZO. Such undesired thin interlayers could block the Li^+ transfer across the interfaces between LCO and LLZ:AlTa, giving rise to the degradation of the SSLB performance. Therefore, the Al-free Ta-substituted LLZO (LLZ:Ta) was prepared via conventional solid-state reaction and used in my work to fabricate the LCO/LLZ:Ta composite cathode.

The chemical composition of the prepared LLZ:Ta powder was analyzed by means of ICP-OES and the result (**Table 6.1**) shows that the concentration of Al is below the detection limit, indicating that the Al-free LLZ:Ta powder was successfully obtained. It is noteworthy to mention here, that in this setup the Al uptake from the crucible was also mitigated, but not completely prevented. The XRD pattern in **Figure 6.1** shows the cubic garnet phase as the main phase, while only a low

intensity peak corresponding to the tetragonal garnet phase is observed. The presence of the tetragonal phase in the starting powder is acceptable, as it will be converted to cubic phase after the aqueous processing and subsequent sintering due to the reversible LHX as described in Section 2.3.2.

Table 6.1 Chemical composition and the normalized elemental content of the LLZ:Ta powder

Element	Weight Percentage [%]	Standard Deviation	Normalized Elemental Content
Li	5.59	0.04	7.11
Al	< 0.001	-	< 0.0003
La	50.2	0.5	3.19
Zr	16.62	0.18	1.61
Ta	8.03	0.09	0.39

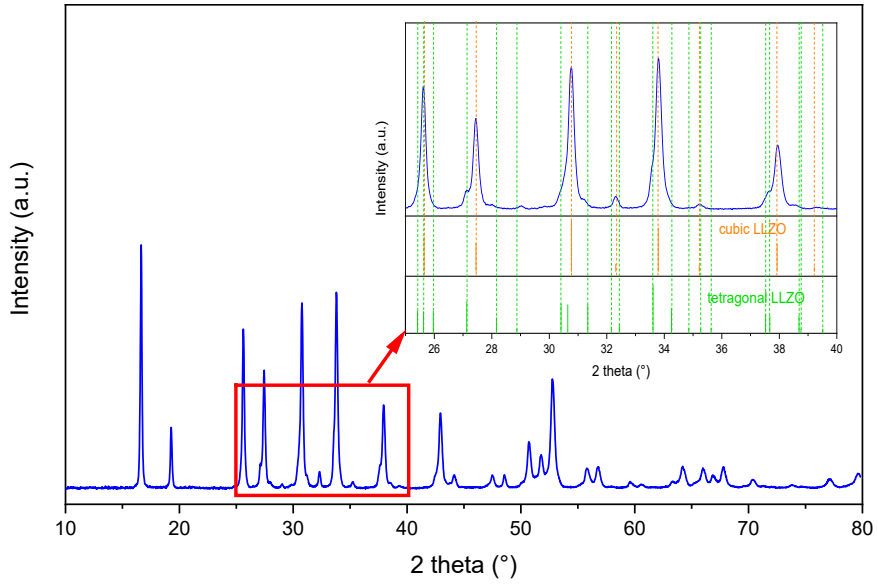

Figure 6.1 XRD pattern of as-synthesized LLZ:Ta powder.

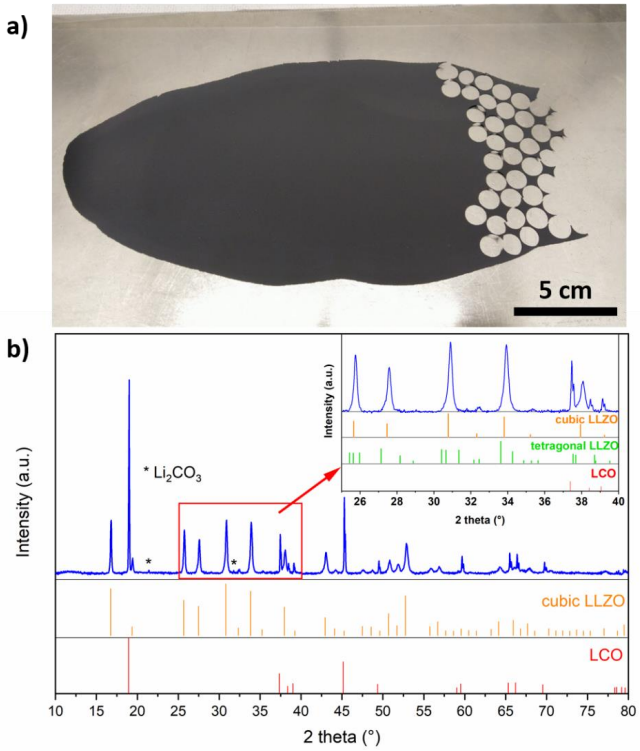

Figure 6.2 a) Digital photograph of a LCO-LLZ:Ta composite cathode green tape fabricated by aqueous tape-casting. The tape has punched holes with a diameter of 1 cm in the right part. b) XRD pattern of the LCO-LLZ:Ta composite cathode green tape. Reference patterns ICSD29225, ICSD182312, and ICSD246816 are used for LCO, cubic LLZO, and tetragonal LLZO, respectively.

The slurry recipe for tape-casting described in Chapter 4 was taken for the tape-casting of LCO-LLZ:Ta composite cathode tapes, since the solid loading and the ratio of methylcellulose binder and the PEG-glycerol plasticizers have been optimized. For the case of LCO-garnet composite cathode, half of the LLZ:AlTa in the recipe was replaced by LCO and the other half by LLZ:Ta. The high volume ratio of LLZ:Ta in the cathode is chosen here to ensure the Li^+ percolation in the composite cathode.[168] The resulted green tape had a homogeneous distribution of these two solids, and was flat, flexible and easy to use for subsequent processing, *e.g.* shaping and lamination (**Figure 6.2a**). As shown in **Figure 6.2b**, both cubic garnet phase and rhombohedral

LCO phase were present as main phases in the XRD pattern of the green tape. The amount of tetragonal LLZO phase was significantly reduced, because it has been partially converted to H-stabilized cubic phase due to the LHX. The exchanged Li^+ was presented in the form of Li_2CO_3 in the tape as a result of its reaction with CO_2 in air. The Li_2CO_3 serves as Li source in the following sintering step to recover the Li content in protonated garnet phase.

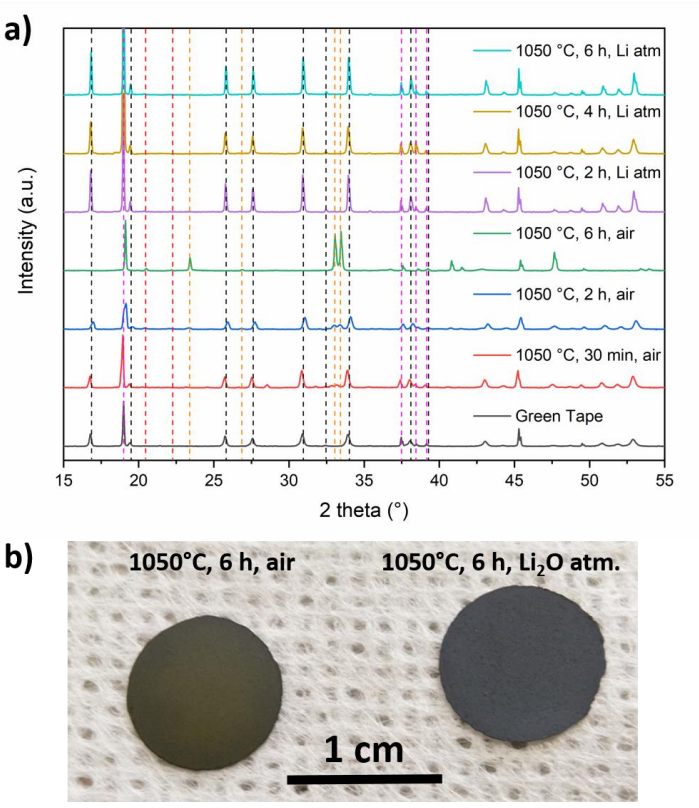

Figure 6.3 a) XRD patterns of LCO-LLZ:Ta composite cathode tapes sintered at 1050 °C with various dwell time in open air or in a closed crucible filled with Li_2O-rich atmosphere (Li atm). The vertical dash lines indicate the main reflections of cubic LLZ:Ta (black), LCO (pink), Li_2ZrO_3 (red) and $LaCoO_3$ (orange). b) Digital photograph of LCO-LLZ:Ta composite cathode tapes sintered at 1050 °C for 6 h in open air or in a closed crucible filled with Li_2O-rich atmosphere. The former one shows yellowish color, indicating the occurring of decomposition, while the latter one keeps the black color like the green tapes.

The co-sintering step of the tape-cast mixed cathode is essential for good electrochemical performance. In practice, the LCO-LLZO mixture is considered thermally stable up to 1085 °C due to the slow kinetics of the decomposition at 700 °C.[249] However, when the aqueous LCO-LLZ:Ta tapes were sintered in an open crucible at 1050 °C, there was decomposition occurring, resulting the formation of Li_2ZrO_3 and $LaCoO_3$, as seen in the XRD patterns (**Figure 6.3a**). When the dwell time extends to 6 h, the garnet phase was completely consumed. This indicates that the protonated LLZO has much lower thermal stability compared with the LLZO with desired stoichiometry. The possible reaction between LCO and protonated LLZO can be described as following:

$$2\ Li_{7-x}H_xLa_3Zr_2O_{12} + 6\ LiCoO_2 \rightarrow 4\ Li_2ZrO_3 + 6\ LaCoO_3 + (3-x)\ Li_2O + x\ H_2O \qquad \text{(Equation 6.1)}$$

The $LaCoO_3$ is a common decomposition product, which was also reported by Ren *et al.*[166] and Vardar *et al.*[250] Besides, other main decomposition product Vardar *et al.* observed, when annealing the LCO-LLZO half cell at 500 °C after thin-film deposition, is $La_2Zr_2O_7$, as expressed by the reaction: [250]

$$Li_7La_3Zr_2O_{12} + LiCoO_2 \rightarrow La_2Zr_2O_7 + LaCoO_3 + 4\ Li_2O \qquad \text{(Equation 6.2)}$$

However, Ren et al. did not observe the presence of La2Zr2O7 after sintering LCO-LLZO composite cathode at 900 °C. [166] Huang *et al.* suggested that $La_2Zr_2O_7$ could react with Li_2O to recover LLZO according to the following equation:[251, 252]

$$3\ La_2Zr_2O_7 + 9\ Li_2O \rightarrow 2\ Li_7La_3Zr_2O_{12} + 2\ Li_2ZrO_3 \qquad \text{(Equation 6.3)}$$

This might help explain the observed Li_2ZrO_3 phase in my experiment instead of $La_2Zr_2O_7$. The decomposition in my case might still occur according to **Equation 6.2** at lower temperature as well, but the product $La_2Zr_2O_7$ was converted to LLZO after the reaction with Li_2O at higher temperature (~900 °C) according to **Equation 6.3**. This recovery step can be accomplished fast, as there was no $La_2Zr_2O_7$ phase observed in the samples sintered even in a quite short time (*e.g.* 30 min).

Other reports suggest La_2CoO_4 as major decomposition product,[253, 254] which is not the case in my sintered samples. The presence of either $LaCoO_3$ or La_2CoO_4 that are poor Li-conducting

compounds will block the Li^+ transfer across the interface of LCO and LLZO, and thus impede the ionic conduction inside the composite cathode and consequently impair the electrochemical performance of the cell. Hence, this side reaction has to be suppressed.

The Li_2O on the right side of either **Equation 6.1** or **Equation 6.2** hints that a Li_2O atmosphere can be created in a closed crucible to suppress these decomposition reactions. Even though some parts of LLZ:Ta decompose to $La_2Zr_2O_7$, the high Li_2O-pressure in the closed crucible can still help recovering the LLZ:Ta according to **Equation 6.3**. Therefore, a certain amount of LiOH powder was intentionally added in the crucible, which can release Li_2O at 924°C (given by the chemical supplier Alfa Aesar). As a result, there were less decomposition products in the samples sintered in the Li_2O-rich atmosphere (**Figure 6.3a**). LCO and LLZ:Ta retain the main phases. Within the garnet LLZ:Ta phase, only cubic phase is observed. This confirms the possibility to convert the tetragonal phase in the starting powder in to cubic phase by the reversible LHX. The photo in **Figure 6.3b** shows the color change from black to yellowish of the sample sintered in open air, while the sample sintered in Li_2O atmosphere remains the black color, indicating no secondary phases formed due to decomposition.

The compaction of the green tapes is a key step to obtain dense cathode after sintering and thus good electrochemical performance. The green tapes were densified by means of warm pressing at 80 °C by an applied mechanical pressure of 250 MPa and 500 MPa, respectively. The SEM images in **Figure 6.4** show the microstructures of the fracture cross-section of the sintered composite cathodes that were warm-pressed with 250 MPa and 500 MPa prior to sintering. The tapes pressed by 250 MPa exhibit porous microstructures after sintering (**Figure 6.4a-b**). Although both LLZ:Ta and LCO formed their individual percolation networks for ions and electrons, the contact between these two components were insufficient, which could lead to impaired charge transfer in this cathode or rapid fracturing during cycling. In contrast, the tapes compacted at 500 MPa are denser after sintering (**Figure 6.4c-d**), giving more contact areas between LCO and LLZ:Ta and thus more percolation paths for Li^+ and electrons to reach the cathode active materials, which is important to the battery performance.

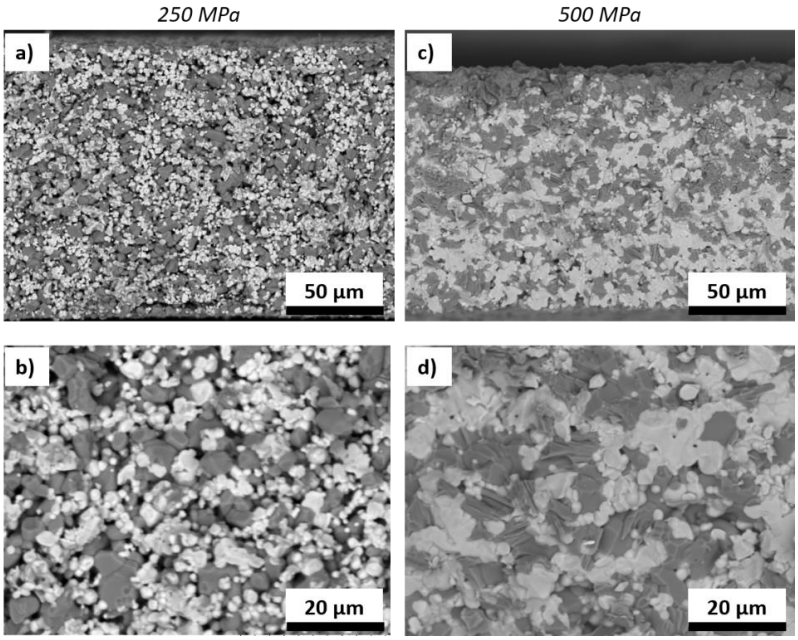

Figure 6.4 Cross-sectional BSE-SEM images of sintered LCO-LLZ:Ta composite cathodes that were compacted at 80 °C under a, b) 250 MPa and c, d) 500 MPa prior to the sintering. The sintering was performed at 1050 °C for 6 h. In these images, the dark and bright phases represent LCO and LLZ:Ta, respectively.

The composite cathode compacted at 500 MPa and subsequently sintered at 1050 °C for 6 h was analyzed by EDS for its elemental distribution. As shown in **Figure 6.5**, Al was found in the sample. The mapping of Al is overlapped with the mapping of Co, and indicates the Al^{3+} diffusion in LCO. Since no Al was in the initial LLZ:Ta phase, the only possible Al-source was the alumina sintering substrate. The areas of the alumina substrate under the cathodes were found dark brownish, indicating the significant Al^{3+}/Co^{3+} exchange. This Al^{3+}-diffusion is not limited to the surface, but through the entire cathode, which is consistent with the observation by Park *et al.* in the co-sintered LCO and Al-doped LLZO.[169] Beside the Al^{3+}-diffusion, also a minor cross-diffusion of Co into LLZO and Zr/La into LCO was observed. Such minor cross-diffusion might take place in my composite cathode as well, as dots of Co appeared in the LLZ:Ta regions and dots of Zr/La in LCO regions. As no coherent layers were formed, it is estimated that the cross-diffusion of these

elements is not significantly impacting the electrochemical properties. Moreover, the BSE-SEM image showed clear phase boundaries between LCO and LLZ:Ta, and no secondary phase at the interfaces, indicating that the Co-diffusion from LCO into LLZ:Ta and the Zr/La-diffusion from LLZ:Ta into LCO were below the detection limit. On the other hand, spots of Al were also found in LLZ:Ta phase but with less density. Unlike extracting Al from Al-doped LLZO that leads to low-conducting tetragonal garnet phase, the uptake of Al in the LLZ:Ta in my composite cathode might help to stabilize the high-conductive cubic garnet phase. Therefore, an improved electrochemical performance of this LCO-LLZ:Ta composite cathode can be expected. The LCO-LLZ:Ta cathode that was compacted under 500 MPa and sintered at 1050 °C for 6 h in the Li-rich atmosphere was further investigated in the full cell later.

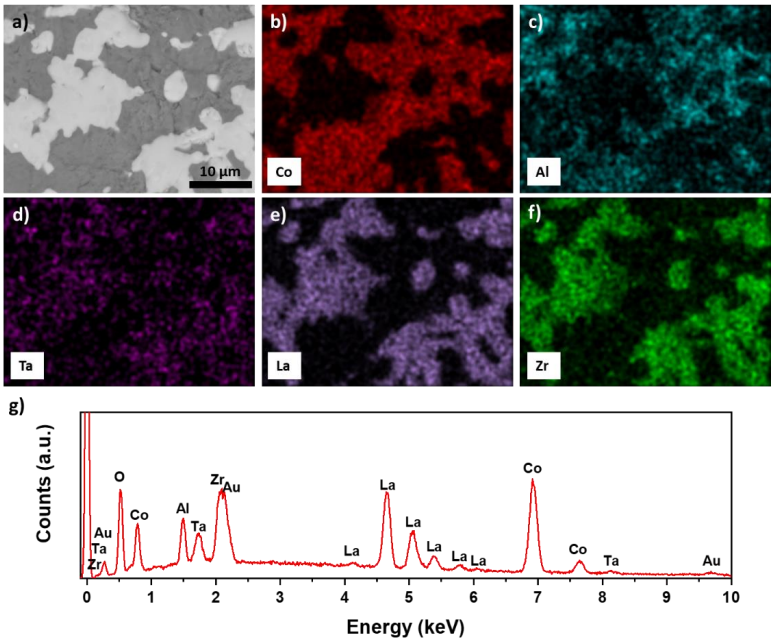

Figure 6.5 EDS measurement on the polished cross-section of LCO-LLZ:Ta composite cathode that was compacted at 80 °C under 500 MPa and subsequently sintered at 1050 °C for 6 h. a) BSE-SEM image of the detected area. b-f) EDS mapping of the elements Co, Al, Ta, La, and Zr. g) the overall spectrum of the detected area. A Au layer was sputtered onto the sample to provide sufficient electronic conductivity and explains the Au signal seen in g).

6.2 Preparation and Electrochemical Stability of Modified Solid Polymer Membranes

The LCO-LLZ:Ta composite cathode is prepared at a sintering temperature of 1050 °C, while the LLZ:AlTa separator requires a sintering temperature of 1175 °C to obtain high relative density (> 90%) (see Section 4.2). This large difference in processing temperature hinders the fabrication of cathodic half cells in one step, *i.e.* laminate the cathode tapes and separator tapes together for co-sintering. Therefore, these two ceramic components have to be prepared separately. When these two ceramic components are brought to contact, the rigid interface without chemical bonding raises large resistances for ionic transportation, and the cells composed of them will have low to no electrochemical performance. Therefore, the interface between the cathode and the separator needs modification. To establish a good contact at the interface, an interlayer consisting of the Li^+-conductive SPE was employed. The flexibility of the SPE helps enlarging the contact area, thus providing sufficient pathways for ionic transport across the interface between the two ceramic components.[255]

PEO is a popular SPE material in solid-state batteries.[256] Although its room-temperature conductivity is far below the required level, a slight increase of the operation temperature to 50-60 °C ensures a good performance of the SSLBs equipped with PEO-based SPE. The main drawback of PEO is its narrow electrochemical stability window, leading to the incompatibility with 4V-cathode materials such as LCO and NMC.[241] Yang *et al.* found that the oxidative limit of PEO comes from the terminal –OH group of the polymer chains, which starts oxidation at 4.05 V *vs.* Li/Li^+, while the breakdown of the main chains occurs only over 4.3 V *vs.* Li/Li^+.[187] This suggests that the modification on the terminal –OH group can prevent the undesired oxidation below 4.3 V *vs.* Li/Li^+, thus adapting the PEO for 4V-cathode materials.

Lin *et al.* developed a strategy to modify the PEO chains by *in-situ* synthesis of SiO_2 nanoparticles.[191] TEOS is a typical Si-precursor for the sol-gel synthesis of SiO_2 nanoparticles.[257] As shown in **Figure 6.6a**, TEOS can undergo hydrolysis and condensation reactions in aqueous solution to form the SiO_x networks. The reaction rate of hydrolysis and condensation and the resulting morphology of the SiO_x networks can be controlled by adjusting

the pH value of the solution.[257] In the case of a pH 10.5-11, as in this work, the SiO_x networks tend to assemble nanospheres.[191] At the surface of these SiO_x nanospheres locate free -OH groups, which can adsorb PEO chains, preferably with the terminal -OH groups of the PEO chains, via hydrogen bonding.[192, 258] Upon drying, the dehydration could take place between the surficial –OH groups of SiO_x nanoparticles and the terminal –OH groups of PEO chains, giving rise to the Si-O-C bonds, so that PEO chains are connected to SiO_x nanospheres. In this way, the terminal –OH groups of PEO chains can be removed, and the oxidation stability of PEO can be improved.

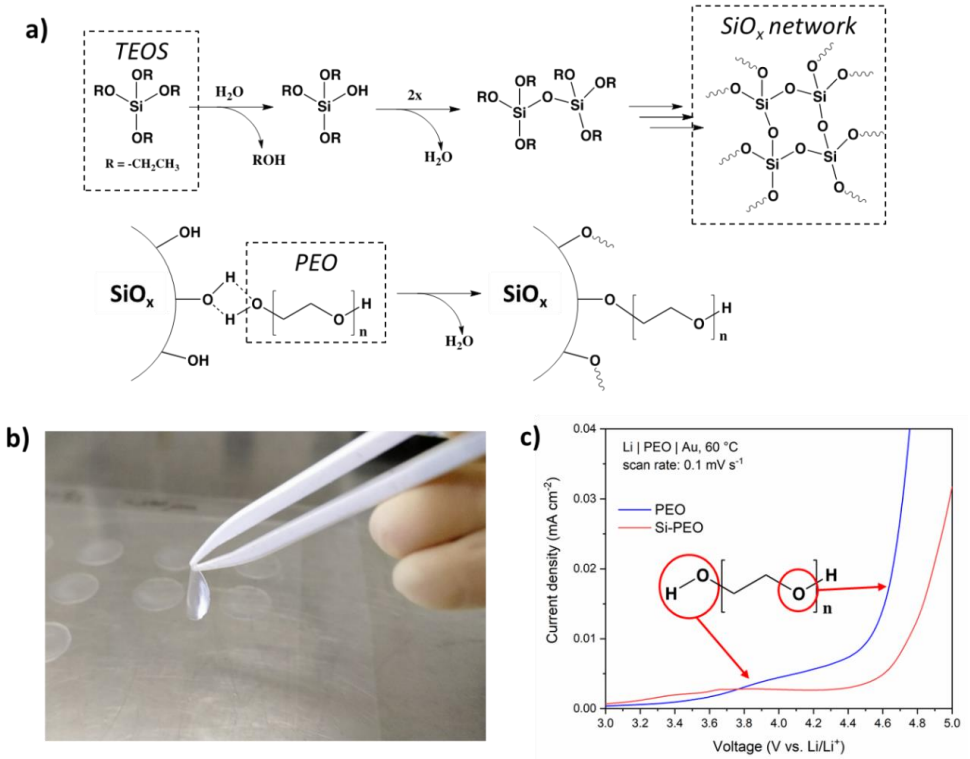

Figure 6.6 a) Scheme of the synthesis mechanism of the Si-PEO membrane. b) Digital photograph of the freestanding Si-PEO membranes (diameter: 12 mm). c) Electrochemical stability of the Si-PEO membrane determined by LSV comparing to the unmodified PEO membrane.

Figure 6.6b shows the freestanding Si-PEO membranes prepared according to Lin *et al.* [191] in this study. These membranes exhibit improved mechanical strength in comparison with unmodified PEO membranes perhaps due to the hydrogen bonding interaction between SiO_x nanospheres and PEO chains[192]. The oxidation stability of the Si-PEO membranes were tested by means of LSV under the increasing potential with a constant rate of 0.1 mV s^{-1} (**Figure 6.6c**). The Si-PEO membrane was sandwiched between a gold WE and a Li metal CE/RE. The anodic response of Si-PEO occurred after 4.3 V *vs.* Li/Li^+, which exactly corresponds to the oxidation of the ether oxygen in the PEO main chains. In comparison, the unmodified PEO membrane measured in the same testing set-up had an anodic response as early as 3.8-3.9 V *vs.* Li/Li^+, which can be attributed to the oxidation of the terminal –OH group on the PEO chains. This means that the modification on the terminal of the PEO was successful, and the upper limit of the electrochemical stability window of the PEO-based SPE has been enlarged to 4.3 V *vs.* Li/Li^+, which is suitable for the application in the SSLB with the prepared LCO-LLZ:Ta composite cathode. The ionic conductivity of the prepared Si-PEO was, however, not measurable, because the thickness of the Si-PEO membrane cannot be determined accurately during the measurement due to the pressure loading (10 N) in the Swagelok test cell. Nevertheless, according to Lin *et al.* and Wang *et al.*, the SiO_x nanospheres can reduce the crystallinity of the PEO segments and thus increase the ionic conductivity to about 1 mS cm^{-1} at 60 °C.[191, 192]

6.3 Electrochemical Performance of Li|garnet|$LiCoO_2$ Solid-State Lithium Batteries

The garnet-supported LCO-based SSLB was assembled layer by layer. The freestanding garnet thin sheet LLZ-Ar fabricated by water-based tape-casting described in Chapter 4 was employed as the separator in the SSLB. After coating a thin Au layer on one side of the garnet separator, a metallic indium foil was brought onto it to act as anode. The purpose of using indium is to avoid lithium dendrite formation, especially for a high-capacity battery as discussed in Section 5.3. Afterwards, the prepared Si-PEO membrane was attached onto the other side of the garnet separator, followed by placing the sintered LCO-LLZ:Ta composited cathode on the top. Due to the strong

hydrogen bonding, the Si-PEO interlayer exhibited good adhesive ability so that the cathode and the separator were bonded tightly.

The electrochemical performance of the SSLB was evaluated by galvanostatic cycling at 60 °C. The slightly increased temperature was required to obtain a good ionic conductivity of the Si-PEO interlayer. A formation cycle was conducted with a constant current density of 50 μA cm^{-2} between 3.6 and 2.8 V *vs.* Li-In/Li^+, *i.e.* 4.2 and 3.4 V *vs.* Li/Li^+ (red curves in **Figure 6.7a**). The coulombic efficiency of the formation cycle was 61.6%, which could be attributed to the irreversible reaction involved in the Li-In alloy formation, as discussed in Section 5.3.

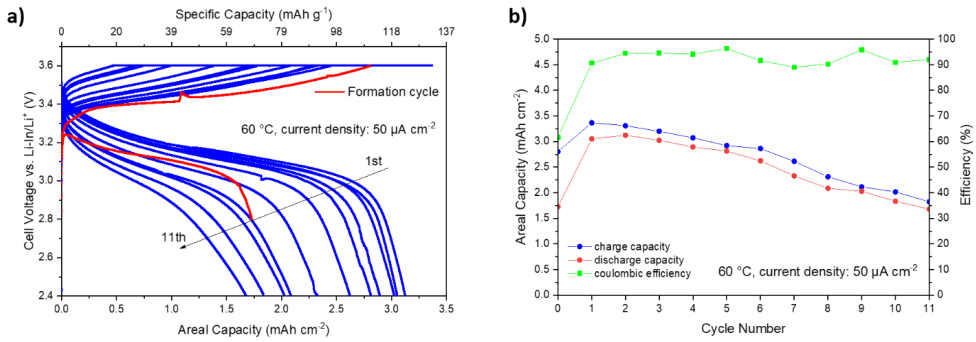

Figure 6.7 Electrochemical performance of the Li-In|LLZ-Ar|Si-PEO|LCO-LLZ:Ta SSLB tested under the current density of 50 μA cm^{-2} at 60 °C: a) charge/discharge curves (the formation cycle is drawn in red); b) cycling performance (the formation cycle is labelled as Cycle 0).

The cell was further cycled with a CC-CV process for charging and a CC process for discharging between 3.6 and 2.4 V *vs.* Li-In/Li^+, *i.e.* 4.2 and 3.0 V *vs.* Li/Li^+ (blue curves in **Figure 6.7a**). The CV process allows to charge more active materials and provide a higher capacity. The cell was charged to 3.6 V *vs.* Li-In/Li^+ with a constant current density of 50 μA cm^{-2}, and the voltage was held until the current density dropped to 5 μA cm^{-2}. The theoretical areal capacity of the LCO-LLZ:Ta composite cathode was calculated by its mass after sintering, since the LCO and LLZ:Ta has a weight ratio of 1:1 in this cathode. A typical LCO-loading in the prepared cathode was about 25.5 mg cm^{-2}, corresponding to 3.49 mAh cm^{-2} (The theoretical specific capacity of 137 mAh g^{-1},

corresponding to half of the Li removed from $LiCoO_2$). The first charge reached a high areal capacity of 3.37 mAh cm^{-2}, indicating a high utilization of the LCO up to 96%. The first discharge at 50 µA cm^{-2} delivered also high capacity over 3 mAh cm^{-2}, and the 2nd discharge reached the highest capacity of 3.12 mAh cm^{-2}, equal to 122 mAh g^{-1} and 89% LCO-utilization. The cell showed degradation in the following cycles, and the capacity dropped to 1.68 mAh cm^{-2} at the 11th discharge (**Figure 6.7b**). The average capacity decay was 5.1% per cycle. The coulombic efficiencies of all 11 cycles were over 90%, and most of them were around 94%. The ageing mechanism behind this degradation is still not clear, and thus needs further investigation.

As discussed in Section 6.1, a degraded LCO-LLZO interface due to the thermal-treatment induced Al/Co cross-diffusion could be excluded in this composite cathode. This degradation mechanism proposed by Park *et al.* describes that the extraction of Al from LLZO leads to the disordering of cubic LLZO to tetragonal.[169] In my composite cathode, the LLZ:Ta itself has no Al, and the Al^{3+}-diffusion into LCO solely comes from the alumina substrate during sintering. Meanwhile no tetragonal LLZ:Ta phase was detected in the sintered cathode. In addition, the SSLB with this blocking interface had a specific capacity of only 35 mAh g^{-1} (entry 3 in **Table 6.2**),[169] while the SSLB demonstrated here exhibited a much higher specific capacity (122 mAh g^{-1}). Even when Li_3BO_3 or $Li_{2.3}C_{0.7}B_{0.3}O_3$ was used as sintering additives to prevent the formation of such highly resistive interface, the maximum specific capacity reached was merely around 100 mAh g^{-1} due to the poor ionic conductivity of these additives (entries 1-8 in **Table 6.2**).[169, 170, 259-262] Alternative to prevent Al/Co cross-diffusion is to avoid the Al substitution in the garnet LLZ:Ta. As a result, the thermal-induced transformation of cubic LLZ:Ta into tetragonal phase is prevented, and high-conductive interfaces are obtained. Therefore, the use of Al-free LLZ:Ta demonstrated in this work enables the sintering without interfacial modification, and achieves the specific capacity as high as a thin-film SSLB[263] (129 mAh g^{-1}, entry 11 in **Table 6.2**) while having more than 100-times higher LCO loading.

Among bulk-type SSLBs (for instance > 1 mAh cm^{-2}), the cell made by Tsai *et al.* via co-sintering LCO-LLZ:Ta also exhibited similar high specific capacity of 117 mAh g^{-1} (entry 13 in **Table 6.2**).[168] A capacity decay of 2.3% per cycle based on first 10 cycles was observed in their cells. They found

the formation of the micro-cracks due to the volume change of LCO during cycling, which they related to the degradation.[264]

Another degradation mechanism is proposed by Ihrig *et al.* recently, that an electrochemically driven Al/Co cross-diffusion during cycling causes the formation of an amorphous secondary phase at the interface between LCO and LLZ:AlTa.[240] The as-sintered composite cathode fabricated by FAST/SPS did not show any Al/Co cross-diffusion, but Al was found in LCO after the electrochemical cycling. The capacity decay per cycle in the initial 5 cycles was 8.1%, 9.4% and 13.5% for the cathode with areal capacities of 0.9, 1.2 and 3.8 mAh cm^{-2}, respectively (entries 14 and 15 in **Table 6.2**).[107, 240] Similarly, the cathode prepared by Rosen *et al.* using the same materials via conventional sintering also showed an average capacity decay of 10.8% per cycle in the initial 5 cycles with the areal capacity of 3 mAh cm^{-2} (entry 16 in **Table 6.2**),[265] which could have the same degradation mechanism. In contrary, the LCO-LLZ:Ta cathode developed in this work had an improved cycling stability with a lower capacity decay of 5.1% per cycle when the high capacity over 3 mAh cm^{-2} was achieved. Since no Al can be extracted from the LLZ:Ta phase in the cathode, this electrochemically driven degradation could be excluded. As there is in fact Al (diffused from alumina substrate) existing in the LCO phase of the cathode, the impact of Al on the battery performance requires further investigation. With this regard, additional experiments by sintering on different substrates can be done for a comparison to evaluate the effect of Al-doping in LCO for the LCO/garnet-type cathodes.[266]

Other degradation contribution could relate to the anode. As shown in Section 5.3, the coulombic efficiency of the LFP-based SSLBs with indium anode was 96-98%, while the one of SSLBs with Li anode was 99%. This means the irreversible reaction during the Li-In alloying brings 1-3% capacity loss. Moreover, the metallic indium has poor wettability at the surface of garnets, giving rise to large resistance.[244]

The degradation could also relate to the decomposition of the Si-PEO interlayer. Although the LSV measurement shows the improved stability of this solid polymer membrane, it might still form certain cathode-electrolyte interfaces due to the continuous decomposition of the polymer and the lithium salt at the high voltage (> 4 V *vs.* Li/Li^+),[267] which needs further investigation. The impedance of this polymer interlayer is hard to precisely distinguish from the impedance of the

cathode side by a simple EIS technique.[172] With this regard, advanced characterization methods and test set-ups are necessary to investigate the influence of Li-In alloying process on the electrochemical performance of the garnet-based SSLBs.[224, 268-270]

Table 6.2 List of LCO cathodes for SSLBs with garnet separators and their test conditions

Entry	Cathode Composition	LCO Loading [mg cm^{-2}]	Operation Temperature [°C]	Current Density [µA cm^{-2}]	Areal Capacity [mAh cm^{-2}]	Specific Capacity [mAh g^{-1}]	Cycles	Ref.
1	LCO-Li_3BO_3	2.35	25	10	0.2	85	5	[259]
2	LCO-Li_3BO_3-LLZO	-	r.t.	1 µA g^{-1}	-	78	1	[260]
3	LCO	-	50	C/5	-	35	10	[169]
4	LCO-Li_3BO_3	-	50	C/5	-	67.2	10	[169]
5	LCO-Li_3BO_3-LLZ:Ta	-	100	100	1.4	-	50	[271]
6	LCO-Li_3BO_3-$In_{2(1-x)}Sn_{2x}O_3$	2.96	r.t.	5	0.056	13.9	6	[261]
7	LCO-Li_3BO_3-$In_{2(1-x)}Sn_{2x}O_3$	1.9	r.t.	5	0.19	101.3	5	[262]
8	LCO-Li_2CO_3-LLZO-$Li_{2.3}C_{0.7}B_{0.3}O_3$	1	100	5.75	0.106	106	40	[170]
			25	5.75	0.094	94	100	
9	LCO	-	-	2	0.015	-	3	[272]
10	LCO	1.52	r.t.	1	-	-	20	[273]
11	LCO	0.203	25	3.5	0.035	129	100	[263]
12	LCO with Nb coating	0.12	r.t.	1-10	0.01	80	25	[254]
13	LCO-LLZ:Ta	12.6	50	50	1.6	117	100	[168]
14	LCO-LLZ:AlTa	16	80	50	1.2	75	5	[107]
15	LCO-LLZ:AlTa	-	80	50	0.9	-	60	[240]
		-	80	50	3.8	-	5	
16	LCO-LLZ:AlTa	-	80	25	2.8	-	20	[265]
17	LCO-LLZ:AlTa	2	60	25	0.27	100	6	[274]
18	LCO-LLZ:BiTa	4.38	60	12	0.54	124	3	[275]
19	LCO-LLZ:AlTa	6	60	50	0.63	105	100	[264]
20	LCO-LLZ:Ta	25.5	60	50	3.12	122	11	This work

6.4 Summary

In this chapter, a LCO-LLZ:Ta composited cathode was successfully fabricated by water-based tape-casting. An aqueous slurry formulation originally developed for garnet-based separators was adopted here to prepare the LCO-LLZ:Ta cathode tapes. The pre-densification pressure and sintering atmosphere were studied, and the optimized processing condition was first to densify

the tape at 500 MPa, and then to sinter it in a Li_2O-rich atmosphere at 1050 °C for 6 h. The obtained cathode had no secondary phase produced by side reactions, and showed high relative density. To enable the use of this cathode in a garnet-supported SSLB, the ceramic separator and the ceramic cathode were bonded by a modified solid polymer membrane Si-PEO, which was prepared from TEOS and PEO in aqueous solution. The Si-PEO membrane exhibited enhanced electrochemical stability over 4 V *vs.* Li/Li^+, and was thus compatible with the prepared cathode for the application in SSLBs. The assembled SSLB delivered a high areal capacity of 3.12 mAh cm^{-2}, corresponding to a specific capacity of 122 mAh g^{-1}, at the current density of 50 µA cm^{-2}. Due to the use of Al-free LLZ:Ta in the starting powder, any degradation related to either thermally induced or electrochemically driven Al/Co cross-diffusion was prevented. Hence, this SSLB exhibited better cycling stability (lower capacity decay) comparing to other bulk-type SSLBs with LCO-LLZ:AlTa cathodes. The coulombic efficiency with around 94% of this SSLB can be attributed to other degradation mechanisms, such as micro-cracks formation, the irreversible reaction in Li-In alloying, and the decomposition of the Si-PEO membrane.

7 Conclusion and Outlook

7.1 Conclusion

This doctoral thesis demonstrated a sustainable fabrication route of garnet solid electrolyte separators and SSLBs thereof.

A water-based tape-casting process using environmental friendly binders to fabricate thin free-standing garnet solid electrolyte separators was successfully developed for the first time. After optimizing the slurry composition and sintering conditions, the obtained garnet solid electrolyte shows a promising total ionic conductivity of 0.15 mS cm^{-1} at room temperature and is (electro-)chemically stable against lithium metal. The garnet-based separator was employed in SSLBs with a separator-supported configuration.

The interaction of garnets with water involved in this developed process was investigated by XRD and TG-MS. It is shown that the occurring Li^+/H^+-exchange reaction is completely reversible in this process and thus enables the formation of stoichiometric Ta- and Al-substituted LLZO with cubic phase.

The cell concept of SSLBs with the separator-supported configuration using the aqueous tape-cast garnet solid electrolyte was validated. The LFP/PEO composite cathode was also fabricated by water-based processing, avoiding the harmful organic solvents commonly used in the conventional production. The LFP:PEO volume ratio is crucial for the electrochemical performance of batteries. With sufficiently high PEO-loading, high-capacity composite cathodes show high Coulombic efficiency (> 99%) and high specific capacity (136 mAh g^{-1}). The electrochemical performance of the “sustainable” cathodes is as high as of conventional cathodes. On the full cell level, the performance even exceeds its conventional counterpart as thinner LLZ:AlTa separators are realized and the energy density is increased.

The water-based tape-casting process is successfully transferred for LCO/LLZ:Ta cathode manufacturing. The LCO/LLZ:Ta composite cathode is dense and phase pure after sintering. Although a half cell process requires further optimization, the composite cathode can be assembled into the full cell by attaching it to the separator with a SiO_x-stabilized PEO membrane.

This membrane has enhanced electrochemical stability over 4 V *vs.* Li/Li$^+$ as required for cathodes like LCO. The Li-In|garnet|Si-PEO|LCO/LLZ:Ta full cell is functional and provides one of the highest areal capacities observed for SSLBs (3.12 mAh cm^{-2}) and is only exceeded by commercial liquid-based cells. While their cycle stability is increased compared to other LCO/LLZO-based SSLBs, even higher cycle stabilities are essential.

7.2 Outlook

The focus of this work was to develop a water-based tape-casting process and enable the sustainable fabrication of garnet-based SSLBs. For this different SSLB set-ups were presented and their functionality were shown. The focus of upcoming work is now to analyze the obtained SSLBs, to understand the cycling degradation mechanisms in detail, and to find the solutions or measures that can improve the cycling stability.

First of all, high-rate operation and prolonging cycle life still remains challenging, especially for the thin garnet separator. Further modification of garnet/Li-interface to achieve a higher applicable current density and better long-term cycling performance of the green batteries is required. Alternative anode materials such as indium and silicon are interesting to be investigated.

Secondly, the Li-In alloy anode seems promising, but the irreversible reaction involved in the alloying process, especially for the initial cycles, prevents the stable cycling. In addition, its interfacial resistance at garnet surface also needs improvement. With this regard, future work can be focused on how to pre-lithiate the indium metal, and how to design and construct an interlayer between Li-In and garnet to reduce the interfacial resistance.

Thirdly, the degradation mechanism is not yet clarified for the SSLB Li-In|garnet|Si-PEO|LCO/LLZ:Ta. Post-mortem analysis should be conducted to figure out the failure causes, which will also help improving the battery design and fabrication in future.

Last but not least, the utilization of water should not be limited in the fabrication stage as demonstrated in this work, but also other stages in the value chain of garnet-based batteries. At the beginning, garnet powder in nano- to submicron-sizes can be synthesized by aqueous sol-gel

process. Once strategies to prevent the Li^+/H^+ exchange are developed, garnet-based separators can thus be employed in aqueous Li-air batteries as future high-energy density storage systems. At the end of the battery life, the spontaneous Li^+/H^+ exchange could be used in future recycling strategies, as it could easily leach the Li from garnet materials in batteries properly designed and prepared for recycling. In this way, a sustainable life cycle for future batteries, from materials preparation over cell design and manufacturing all the way to end-of-life and recycling, can help to shape a greener future.

8 Appendix

8.1 Acknowledgement

This work is completed under the project 'Grüne Elektrochemische Energiespeicher (GrEEn)' (project number: 313-W044B) sponsored by the Ministry of Economic Affairs, Innovation, Digitalization and Energy of the state North-Rhine Westphalia. This financial support is gratefully acknowledged.

I would like to express gratitude to my 'Doktorvater' Prof. Dr. Egbert Figgemeier, who offers me this opportunity to pursuit the doctoral degree, and leads my way into the scientific career.

I would also like to appreciate Dr. Martin Finsterbusch for his direct guidance in daily lab works, all the suggestions and advices in my research, and lots of correction and revision of my manuscripts, meeting abstracts, work reports and project reports. Prof. Dr. Olivier Guillon and Prof. Dr. Dina Fattakhova-Rohlfing are also acknowledged here for their suggestions and advices in my work reports.

It is my great honor to have Prof. Dr. Dr. h.c. Rolf Hempelmann as the second reviewer of my dissertation.

Colleagues at IEK-1 are gratefully acknowledged for their daily co-works and helps. I would like to thank Volker Bader, who has performed calcination and sintering of thousands of my samples. Without him and his expertise in thermal treatments, I could not accomplish my work. I also thank Philipp Hecker, Grit Häuschen, Dr. Qianli Ma, Dr. Tu Lan, and Dr. Apurv Dash for their helps in operating furnaces when Volker is not there (mostly because I prepare the samples too late…). During the 4-year working time, I have discussed a lot with Dr. Qianli Ma, Dr. Tu Lan, and Dr. Martin Ihrig as well as Dr. Chih-Long Tsai from theoretical to practical aspects of material synthesis and processing, electrochemistry and battery operation. In addition, I have learned a lot from Dr. Enkhtsetseg Dashjav and Dr. Monika Bhardwaj in tape-casting and sintering of tapes, and their experiences help me solving many problems occurring in my research work. Also, thanks are given to Ralf Kauert, who gives me the first knowledge about aqueous tape-casting, and is in charge of the maintenance of the Thinky mixer and the tape-casting bench. Without these properly running devices I could not do my work.

I am grateful to those who help me a lot in experiments: Philipp Hecker (ordering chemicals and lab tools), Grit Häuschen (LLZO synthesis), Dr. Yoo-Jung Sohn (XRD and Rietveld refinement), Andrea Hilgers (PSD and rheology tests), Marie-Theres Gerhards (thermal analysis), Mark Kappertz (metallograpy) and Dr. Volker Nischwitz from ZEA-3 (ICP-OES) as well as Dr. Tim Van Gestel (2-person rules). Also, many thanks to Dr. Sven Uhlenbruck, Dr. Sandra Lobe, Dr. Christian Dellen, Frank Vondahlen and Dr. Markus Mann for the maintenance of key equipment and devices

including gloveboxes, biologic potentiostats, sputter-coaters, Hitachi SEM and Raman spectroscopy. In addition, administrative personals are also acknowledged here.

On the Aachen side, I would like to thank Christina Birke, who establishes my close contact to Aachen, dealing with all my project-related paperwork; and to Niloofar Hamzelui, who measures ART-FTIR for my samples, and prepares new samples in our collaboration which are really challenging and time-consuming.

On the Münster side, I would like to thank Dr. Simon Dühnen and Jens Wrogemann for their excellent coordination and organization within the GrEEn project. Thanks are given to Dr. Placke, Dr. Schmuch, Dr. Cekic-Laskovic, Dr. Paillard, Dr. Kungl, Dr. Finsterbusch, Prof. Dr. Sauer, Prof. Dr. Moerschbacher, Prof. Dr. Prüfer, and Prof. Dr. Hippler for their informative lectures about green batteries.

Thanks are given to all team members for nice office atmosphere, summer BBQ and Christmas party. Also to Dapeng, Aikai, Huiyu, Yuan, Yuning and Runze for every lunch time; to Serkan, Younas, Ranjith, Martin I., Liang-Yin, Shiho, Ting, Wei and Ying for our weekend gathering, dinners, board games, and hiking, giving me wonderful memories out of laboratory.

Special thanks are given to doctors at St. Elisabeth Hospital in Jülich, who saved my life in emergency. Without their great efforts, I would have no chance to still live in this world.

My sincere thanks are given to my parents, parents-in-law, and other family members including grandma, uncles and aunties, who are always supporting my study and life abroad.

My best thanks and heartfelt love are given to my wife Dr. Xiaochen Zhang for her love, understanding, caring and supporting. By giving up her colorful life in Shanghai and in Berlin, she moves to Jülich to accompany me. I deeply appreciate her great dedication to our family life when I was busy with works.

8.2 List of Figures

8.3 List of Tables

8.4 List of Abbreviations

ACN	acetonitrile
ALB	aqueous lithium metal battery
ART-FTIR	attenuated total reflection Fourier transform infrared spectroscopy
BSE	back-scattered electron
CAM	cathode active material
CC-CV	constant-current-constant-voltage
CE	counter electrode
CPE	constant phase element
CV	cyclic voltammetry
EDS	energy-dispersive X-ray spectroscopy
EIS	electrochemical impedance spectroscopy
FAST/SPS	field-assisted sintering / spark plasma sintering
ICP-OES	inductively coupled plasma optical emission spectroscopy
IPA	*iso*-propanol
LCO	$LiCoO_2$
LFP	$LiFePO_4$
LHX	Li^+/H^+ exchange
LIB	lithium ion battery
LiTFSI	lithium bis(trifluoromethanesulfonyl)imide
LLZ:AlTa	$Li_{6.45}Al_{0.05}La_3Zr_{1.6}Ta_{0.4}O_{12}$
LLZ:Ta	$Li_{6.6}La_3Zr_{1.6}Ta_{0.4}O_{12}$
LLZO	$Li_7La_3Zr_2O_{12}$
LMO	$LiMn_2O_4$
LSV	linear scan voltammetry, or linear sweep voltammetry
MC	methylcellulose
n.a.	not available
NCA	$LiNi_xCo_yAl_{1-x-y}O$

NMC	$LiNi_xMn_yCo_{1-x-y}O$
NMP	N-methyl-2-pyrrolidione
PEG	polyethylene glycol
PEO	polyethylene oxide
PVdF	polyvinylidene fluoride
r.t.	room temperature
RE	reference electrode
SE	Solid electrolyte
SEM	scanning electron microscope
SHE	standard hydrogen electrode
SG	space group
Si-PEO	SiO_x-modified polyethylene oxide
SSLB	solid-state lithium battery
TEOS	tetraethyl orthosilicate
TG-MS	thermogravimetry coupling with mass spectrometry
WE	working electrode
XRD	X-ray diffraction

8.5 Publications

Within the course of this scientific work, several publications have been prepared which are listed below. Content from these publications is used for this thesis. This is in line with the rules for dissertation of the Faculty for Electrical Engineering and Information Technology at RWTH Aachen University, and has been agreed with Prof. Egbert Figgemeier, the major supervisor of this thesis. Text elements, graphs, pictures or tables from these publications are not explicitly cited within the thesis, as far as they are mainly created by me. If such elements in the listed publications are mainly created by the co-authors, a direct link to the publication is given.

Journal articles:

1. **R. Ye**, C.-L. Tsai, M. Ihrig, S. Sevinc, M. Rosen, E. Dashjav, Y. J. Sohn, E. Figgemeier,* and M. Finsterbusch*, 'Water-based fabrication of garnet-based solid electrolyte separators for solid-state lithium batteries', *Green Chem.*, **2020**, 22, 4952-4961.
2. **R. Ye**, M. Ihrig, N. Imanishi, M. Finsterbusch,* and E. Figgemeier*, 'A Review on Li^+/H^+ Exchange in Garnet Solid Electrolytes: From Instability against Humidity to Sustainable Processing in Water', *ChemSusChem*, **2021**, 14, 4397-4407. (Cover Feature)
3. **R. Ye**, N. Hamzelui, M. Ihrig, M. Finsterbusch,* and E. Figgemeier, 'Water-Based Fabrication of a $Li|Li_7La_3Zr_2O_{12}|LiFePO_4$ Solid-State Battery - Towards Green Battery Production', *ACS Sustainable Chem. Eng.,* **2022**, 10 (23), 7613-7624.
4. **R. Ye**,* M. Ihrig, E. Figgemeier, D. Fattakhova-Rohlfing, and M. Finsterbusch, 'Aqueous Processing of $LiCoO_2$-$Li_{6.6}La_3Zr_{1.6}Ta_{0.4}O_{12}$ Composite Cathode for High-Capacity Solid-State Lithium Batteries', *ACS Sustainable Chem. Eng.,* **2023**, DOI: 10.1021/acssuschemeng.2c07556.

Conference contribution:

5. **R. Ye**,* M. Finsterbusch, and E. Figgemeier, 'Free-standing Garnet-Type Solid Electrolyte Fabricated by Water-Based Tape-Casting', poster on Conference *PRiME 2020*, **2020**, online.
6. **R. Ye**,* M. Ihrig, M. Finsterbusch, and E. Figgemeier, 'Sustainable Fabrication of Garnet-based Solid-state Lithium Battery', oral talk on Conference *72nd Annual Meeting of International Society of Electrochemistry (ISE)*, **2021**, Jeju, Korea.
7. **R. Ye**,* M. Finsterbusch, and E. Figgemeier, 'Aqueous Processing of Garnet-Type Li-Ion Conductors Enabled by Reversible Li^+/H^+ Exchange', oral talk on Conference *ACerS Pan American Ceramics Congress 2022 (PACC '22)*, **2022**, Panama City, Panama.

During the doctoral study, I have taken part in other scientific works, and several publications have been prepared which are listed below. Content from these publications are not used for this thesis.

8. M. Ihrig, M. Finsterbusch,* C.-L. Tsai, A. Laptev, C.-h. Tu, M. Bram, Y. J. Sohn, **R. Ye**, S. Sevinc, S.-k. Lin, D. Fattakhova-Rohlfing, and O. Guillon, 'Low temperature sintering of fully inorganic all-solid-state batteries – Impact of interfaces on full cell performance', *J. Power Sources*, **2021**, 482, 228905
9. M. Ihrig,* **R. Ye**, A. Laptev, D. Grüner, R. Guerdelli, W. S. Scheld, M. Finsterbusch, H.-D-Wiemhöfer, D. Fattakhova-Rohlfing, and O. Guillon, 'Polymer–Ceramic Composite Cathode with Enhanced Storage Capacity Manufactured by Field-Assisted Sintering and Infiltration', *ACS Appl. Energy Mater.*, **2021**, 4(10), 10428-10432.
10. M. Rosen, **R. Ye**, M. Mann, S. Lobe, M. Finsterbusch,* O. Guillon, and D. Fattakhova-Rohlfing *et al.*, 'Controlling the lithium proton exchange of LLZO to enable reproducible processing and performance optimization', *J. Mater. Chem. A*, **2021**, 9, 4831-4840.
11. A. Yang, **R. Ye**, X. Li, Q. Lu, H. Song, D. Grüner, Q. Ma,* F. Tietz, D. Fattakhova-Rohlfing, and O. Guillon, 'Fabrication of thin sheets of the sodium superionic conductor $Na_5YSi_4O_{12}$ with tape-casting', *Chem. Eng. J.*, **2022**, 435(1), 134774.
12. M. Ihrig,* M. Finsterbusch,* A. Laptev, C.-h. Tu, N. T. T. Tran, C.-a. Lin, L.-Y. Kuo, **R. Ye**, Z. J. Sohn, P. Kaghazchi, S.-k. Lin, D. Fattakhova-Rohlfing, and O. Guillon, 'Study of $LiCoO_2$/$Li_7La_3Zr_2O_{12}$:Ta Interface Degradation in All-Solid-State Lithium Batteries', *ACS Appl. Mater. Interfaces*, **2022**, 14, 11288-11299.
13. M. Ihrig,* E. Dashjav, A. Laptev, **R. Ye**, D. Grüner. M. Ziegner, P. Odenwald, M. Finsterbusch, F. Tietz, D. Fattakhova-Rohlfing, and O. Guillon, 'Increasing the performance of all-solid-state Li batteries by infiltration of Li-ion conducting polymer into LFP-LATP composite cathode', *J. Power Sources*, **2022**, 543, 231822.
14. M. Ihrig,* L.-Y. Kuo, S. Lobe, A. Laptev, C.-a. Lin, C.-h. Tu, **R. Ye**, P. Kaghazchi, L. Cressa, S. Eswara, S.-k. Lin, O. Guillon, D. Fattakhova-Rohlfing,* and M. Finsterbusch*, 'Thermal Recovery of the Electrochemically Degraded $LiCoO_2$/$Li_7La_3Zr_2O_{12}$:AlTa Interface in an All-Solid-State Lithium Battery', *ACS Appl. Mater. Interfaces*, **2023**, 15, 4101-4112.

8.6 References

1. Poizot, P. and Dolhem, F., *Clean energy new deal for a sustainable world: from non-CO2 generating energy sources to greener electrochemical storage devices.* Energy & Environmental Science, 2011. **4**(6): p. 2003-2019.
2. Yang, Z.G., Zhang, J.L., Kintner-Meyer, M.C.W., Lu, X.C., Choi, D.W., Lemmon, J.P., and Liu, J., *Electrochemical Energy Storage for Green Grid.* Chemical Reviews, 2011. **111**(5): p. 3577-3613.
3. Larcher, D. and Tarascon, J.M., *Towards greener and more sustainable batteries for electrical energy storage.* Nature Chemistry, 2015. **7**(1): p. 19-29.
4. Placke, T., Kloepsch, R., Dühnen, S., and Winter, M., *Lithium ion, lithium metal, and alternative rechargeable battery technologies: the odyssey for high energy density.* Journal of Solid State Electrochemistry, 2017. **21**(7): p. 1939-1964.
5. Ding, Y., Cano, Z.P., Yu, A., Lu, J., and Chen, Z., *Automotive Li-Ion Batteries: Current Status and Future Perspectives.* Electrochemical Energy Reviews, 2019. **2**(1): p. 1-28.
6. Etacheri, V., Marom, R., Elazari, R., Salitra, G., and Aurbach, D., *Challenges in the development of advanced Li-ion batteries: a review.* Energy & Environmental Science, 2011. **4**(9): p. 3243-3262.
7. Armand, M. and Tarascon, J.M., *Building better batteries.* Nature, 2008. **451**(7179): p. 652-657.
8. Dunn, B., Kamath, H., and Tarascon, J.M., *Electrical Energy Storage for the Grid: A Battery of Choices.* Science, 2011. **334**(6058): p. 928-935.
9. Figgener, J., Stenzel, P., Kairies, K.-P., Linßen, J., Haberschusz, D., Wessels, O., Robinius, M., Stolten, D., and Sauer, D.U., *The development of stationary battery storage systems in Germany – status 2020.* Journal of Energy Storage, 2021. **33**: p. 101982.
10. Janek, J. and Zeier, W.G., *A solid future for battery development.* Nature Energy, 2016. **1**: p. 16141.
11. Manthiram, A., Yu, X.W., and Wang, S.F., *Lithium battery chemistries enabled by solid-state electrolytes.* Nature Reviews Materials, 2017. **2**(4): p. 16103.
12. Dühnen, S., Betz, J., Kolek, M., Schmuch, R., Winter, M., and Placke, T., *Toward Green Battery Cells: Perspective on Materials and Technologies.* Small Methods, 2020. **4**(7): p. 2000039.
13. Wang, C., Fu, K., Kammampata, S.P., McOwen, D.W., Samson, A.J., Zhang, L., Hitz, G.T., Nolan, A.M., Wachsman, E.D., Mo, Y., Thangadurai, V., and Hu, L., *Garnet-Type Solid-State Electrolytes: Materials, Interfaces, and Batteries.* Chemical Reviews, 2020. **120**(10): p. 4257-4300.
14. Ye, R., Ihrig, M., Imanishi, N., Finsterbusch, M., and Figgemeier, E., *A Review on Li+/H+ Exchange in Garnet Solid Electrolytes: From Instability against Humidity to Sustainable Processing in Water.* ChemSusChem, 2021. **14**(20): p. 4397-4407.
15. Takehara, Z.-i., *On the reaction in the lead–acid battery (as the special review-article by the 2005' Gaston Planté Medal recipient).* Journal of Power Sources, 2006. **158**(2): p. 825-830.
16. Judez, X., Eshetu, G.G., Li, C., Rodriguez-Martinez, L.M., Zhang, H., and Armand, M., *Opportunities for Rechargeable Solid-State Batteries Based on Li-Intercalation Cathodes.* Joule, 2018. **2**(11): p. 2208-2224.
17. Doeff, M., *Batteries: Overview of Battery Cathodes*. 2012. p. 709-739.
18. Zeng, X., Li, M., Abd El-Hady, D., Alshitari, W., Al-Bogami, A.S., Lu, J., and Amine, K., *Commercialization of Lithium Battery Technologies for Electric Vehicles.* Advanced Energy Materials, 2019. **9**(27): p. 1900161.
19. Mizushima, K., Jones, P.C., Wiseman, P.J., and Goodenough, J.B., *LixCoO2 (0<x<-1): A new cathode material for batteries of high energy density.* Materials Research Bulletin, 1980. **15**(6): p. 783-789.
20. Eshetu, G.G., Zhang, H., Judez, X., Adenusi, H., Armand, M., Passerini, S., and Figgemeier, E., *Production of high-energy Li-ion batteries comprising silicon-containing anodes and insertion-type cathodes.* Nature Communications, 2021. **12**(1): p. 5459.

21. Thackeray, M.M., David, W.I.F., Bruce, P.G., and Goodenough, J.B., *Lithium insertion into manganese spinels.* Materials Research Bulletin, 1983. **18**(4): p. 461-472.
22. Wang, Y., He, P., and Zhou, H., *Olivine LiFePO4: development and future.* Energy & Environmental Science, 2011. **4**(3): p. 805-817.
23. Yuan, L.-X., Wang, Z.-H., Zhang, W.-X., Hu, X.-L., Chen, J.-T., Huang, Y.-H., and Goodenough, J.B., *Development and challenges of LiFePO4 cathode material for lithium-ion batteries.* Energy & Environmental Science, 2011. **4**(2): p. 269-284.
24. Padhi, A.K., Nanjundaswamy, K.S., and Goodenough, J.B., *Phospho‐olivines as Positive‐Electrode Materials for Rechargeable Lithium Batteries.* Journal of The Electrochemical Society, 1997. **144**(4): p. 1188-1194.
25. Guerfi, A., Kaneko, M., Petitclerc, M., Mori, M., and Zaghib, K., *LiFePO4 water-soluble binder electrode for Li-ion batteries.* Journal of Power Sources, 2007. **163**(2): p. 1047-1052.
26. Cai, Z.P., Liang, Y., Li, W.S., Xing, L.D., and Liao, Y.H., *Preparation and performances of LiFePO4 cathode in aqueous solvent with polyacrylic acid as a binder.* Journal of Power Sources, 2009. **189**(1): p. 547-551.
27. Porcher, W., Lestriez, B., Jouanneau, S., and Guyomard, D., *Design of Aqueous Processed Thick LiFePO4 Composite Electrodes for High-Energy Lithium Battery.* Journal of The Electrochemical Society, 2009. **156**(3): p. A133-A144.
28. Li, C.-C. and Lin, Y.-S., *Interactions between organic additives and active powders in water-based lithium iron phosphate electrode slurries.* Journal of Power Sources, 2012. **220**: p. 413-421.
29. Li, J., Armstrong, B.L., Daniel, C., Kiggans, J., and Wood, D.L., *Optimization of multicomponent aqueous suspensions of lithium iron phosphate (LiFePO4) nanoparticles and carbon black for lithium-ion battery cathodes.* Journal of Colloid and Interface Science, 2013. **405**: p. 118-124.
30. Li, J.L., Armstrong, B.L., Kiggans, J., Daniel, C., and Wood, D.L., *Lithium Ion Cell Performance Enhancement Using Aqueous LiFePO4 Cathode Dispersions and Polyethyleneimine Dispersant.* Journal of the Electrochemical Society, 2013. **160**(2): p. A201-A206.
31. Tsai, J.-C., Tsai, F.-Y., Tung, C.-A., Hsieh, H.-W., and Li, C.-C., *Gelation or dispersion of LiFePO4 in water-based slurry?* Journal of Power Sources, 2013. **241**: p. 400-403.
32. Tsai, F.-Y., Jhang, J.-H., Hsieh, H.-W., and Li, C.-C., *Dispersion, agglomeration, and gelation of LiFePO4 in water-based slurry.* Journal of Power Sources, 2016. **310**: p. 47-53.
33. Kvasha, A., Urdampilleta, I., de Meatza, I., Bengoechea, M., Blázquez, J.A., Yate, L., Miguel, O., and Grande, H.-J., *Towards high durable lithium ion batteries with waterborne LiFePO4 electrodes.* Electrochimica Acta, 2016. **215**: p. 238-246.
34. Li, C.-C., Chen, C.-A., and Chen, M.-F., *Gelation mechanism of organic additives with LiFePO4 in the water-based cathode slurries.* Ceramics International, 2017. **43**: p. S765-S770.
35. Aguiló-Aguayo, N., Hubmann, D., Khan, F.U., Arzbacher, S., and Bechtold, T., *Water-based slurries for high-energy LiFePO4 batteries using embroidered current collectors.* Scientific Reports, 2020. **10**(1): p. 5565.
36. Gordon, R., Kassar, M., and Willenbacher, N., *Effect of Polymeric Binders on Dispersion of Active Particles in Aqueous LiFePO4-Based Cathode Slurries as well as on Mechanical and Electrical Properties of Corresponding Dry Layers.* ACS Omega, 2020. **5**(20): p. 11455-11465.
37. Porcher, W., Moreau, P., Lestriez, B., Jouanneau, S., Le Cras, F., and Guyomard, D., *Stability of LiFePO4 in water and consequence on the Li battery behaviour.* Ionics, 2008. **14**(6): p. 583-587.
38. Zaghib, K., Dontigny, M., Charest, P., Labrecque, J.F., Guerfi, A., Kopec, M., Mauger, A., Gendron, F., and Julien, C.M., *Aging of LiFePO4 upon exposure to H2O.* Journal of Power Sources, 2008. **185**(2): p. 698-710.

39. Cuisinier, M., Martin, J.-F., Dupré, N., Kanno, R., and Guyomard, D., *Elucidating the LiFePO4 air aging mechanism to predict its electrochemical performance.* Journal of Materials Chemistry, 2011. **21**(46): p. 18575-18583.
40. Cuisinier, M., Martin, J.-F., Dupré, N., Yamada, A., Kanno, R., and Guyomard, D., *Moisture driven aging mechanism of LiFePO4 subjected to air exposure.* Electrochemistry Communications, 2010. **12**(2): p. 238-241.
41. Geng, L., Foley, S.B., Dong, H., and Koenig Jr., G.M., *LiFePO4-Accelerated Change in Surface and Electrochemical Properties in Aqueous Systems Induced by Mechanical Agitation.* Energy Technology, 2019. **7**(3): p. 1801116.
42. Mohri, M., Yanagisawa, N., Tajima, Y., Tanaka, H., Mitate, T., Nakajima, S., Yoshida, M., Yoshimoto, Y., Suzuki, T., and Wada, H., *Rechargeable lithium battery based on pyrolytic carbon as a negative electrode.* Journal of Power Sources, 1989. **26**(3): p. 545-551.
43. Asenbauer, J., Eisenmann, T., Kuenzel, M., Kazzazi, A., Chen, Z., and Bresser, D., *The success story of graphite as a lithium-ion anode material – fundamentals, remaining challenges, and recent developments including silicon (oxide) composites.* Sustainable Energy & Fuels, 2020. **4**(11): p. 5387-5416.
44. Li, H., *A High Capacity Nano-Si Composite Anode Material for Lithium Rechargeable Batteries.* Electrochemical and Solid-State Letters, 1999. **2**(11): p. 547.
45. Derrien, G., Hassoun, J., Panero, S., and Scrosati, B., *Nanostructured Sn–C Composite as an Advanced Anode Material in High-Performance Lithium-Ion Batteries.* Advanced Materials, 2007. **19**(17): p. 2336-2340.
46. Li, N. and Martin, C.R., *A High-Rate, High-Capacity, Nanostructured Sn-Based Anode Prepared Using Sol-Gel Template Synthesis.* Journal of The Electrochemical Society, 2001. **148**(2): p. A164.
47. Ferg, E., Gummow, R.J., de Kock, A., and Thackeray, M.M., *Spinel Anodes for Lithium-Ion Batteries.* Journal of The Electrochemical Society, 1994. **141**(11): p. L147-L150.
48. Armstrong, G., Armstrong, A.R., Bruce, P.G., Reale, P., and Scrosati, B., *TiO2(B) Nanowires as an Improved Anode Material for Lithium-Ion Batteries Containing LiFePO4 or LiNi0.5Mn1.5O4 Cathodes and a Polymer Electrolyte.* Advanced Materials, 2006. **18**(19): p. 2597-2600.
49. Ramakumar, S., Deviannapoorani, C., Dhivya, L., Shankar, L.S., and Murugan, R., *Lithium garnets: Synthesis, structure, Li+ conductivity, Li+ dynamics and applications.* Progress in Materials Science, 2017. **88**: p. 325-411.
50. Inaguma, Y., Liquan, C., Itoh, M., Nakamura, T., Uchida, T., Ikuta, H., and Wakihara, M., *High ionic conductivity in lithium lanthanum titanate.* Solid State Communications, 1993. **86**(10): p. 689-693.
51. Morimoto, H., Awano, H., Terashima, J., Shindo, Y., Nakanishi, S., Ito, N., Ishikawa, K., and Tobishima, S.-i., *Preparation of lithium ion conducting solid electrolyte of NASICON-type Li1+xAlxTi2−x(PO4)3 (x = 0.3) obtained by using the mechanochemical method and its application as surface modification materials of LiCoO2 cathode for lithium cell.* Journal of Power Sources, 2013. **240**: p. 636-643.
52. Hong, H.Y.P., *Crystal structure and ionic conductivity of Li14Zn(GeO4)4 and other new Li+ superionic conductors.* Materials Research Bulletin, 1978. **13**(2): p. 117-124.
53. Knauth, P., *Inorganic solid Li ion conductors: An overview.* Solid State Ionics, 2009. **180**(14): p. 911-916.
54. Murugan, R., Thangadurai, V., and Weppner, W., *Fast Lithium Ion Conduction in Garnet-Type Li7La3Zr2O12.* Angewandte Chemie International Edition, 2007. **46**(41): p. 7778-7781.
55. Kennedy, J.H., Sahami, S., Shea, S.W., and Zhang, Z., *Preparation and conductivity measurements of SiS2 Li2S glasses doped with LiBr and LiCl.* Solid State Ionics, 1986. **18-19**: p. 368-371.
56. Lau, J., DeBlock, R.H., Butts, D.M., Ashby, D.S., Choi, C.S., and Dunn, B.S., *Sulfide Solid Electrolytes for Lithium Battery Applications.* Advanced Energy Materials, 2018. **8**(27): p. 1800933.

57. Ryoji, K., Yasuo, T., Masashi, M., and Osamu, Y., *Ionic Conductivity and Structure of Double Chloride Li2ZnCl4 in the LiCl–ZnCl2 System.* Chemistry Letters, 1989. **18**(2): p. 223-226.
58. Zhao, Y. and Daemen, L.L., *Superionic Conductivity in Lithium-Rich Anti-Perovskites.* Journal of the American Chemical Society, 2012. **134**(36): p. 15042-15047.
59. Li, X., Liang, J., Yang, X., Adair, K.R., Wang, C., Zhao, F., and Sun, X., *Progress and perspectives on halide lithium conductors for all-solid-state lithium batteries.* Energy & Environmental Science, 2020. **13**(5): p. 1429-1461.
60. Meyer, W.H., *Polymer Electrolytes for Lithium-Ion Batteries.* Advanced Materials, 1998. **10**(6): p. 439-448.
61. Zhao, Y., Wang, L., Zhou, Y., Liang, Z., Tavajohi, N., Li, B., and Li, T., *Solid Polymer Electrolytes with High Conductivity and Transference Number of Li Ions for Li-Based Rechargeable Batteries.* Advanced Science, 2021. **8**(7): p. 2003675.
62. Thangadurai, V., Kaack, H., and Weppner, W.J.F., *Novel Fast Lithium Ion Conduction in Garnet-Type Li5La3M2O12 (M = Nb, Ta).* Journal of the American Ceramic Society, 2003. **86**(3): p. 437-440.
63. Thangadurai, V. and Weppner, W., *Li6ALa2Ta2O12 (A = Sr, Ba): Novel Garnet-Like Oxides for Fast Lithium Ion Conduction.* Advanced Functional Materials, 2005. **15**(1): p. 107-112.
64. Thangadurai, V., Narayanan, S., and Pinzaru, D., *Garnet-type solid-state fast Li ion conductors for Li batteries: critical review.* Chemical Society Reviews, 2014. **43**(13): p. 4714-4727.
65. Samson, A.J., Hofstetter, K., Bag, S., and Thangadurai, V., *A bird's-eye view of Li-stuffed garnet-type Li7La3Zr2O12 ceramic electrolytes for advanced all-solid-state Li batteries.* Energy & Environmental Science, 2019. **12**(10): p. 2957-2975.
66. Li, Y., Han, J.-T., Wang, C.-A., Xie, H., and Goodenough, J.B., *Optimizing Li+ conductivity in a garnet framework.* Journal of Materials Chemistry, 2012. **22**(30): p. 15357-15361.
67. Sharafi, A., Kazyak, E., Davis, A.L., Yu, S., Thompson, T., Siegel, D.J., Dasgupta, N.P., and Sakamoto, J., *Surface Chemistry Mechanism of Ultra-Low Interfacial Resistance in the Solid-State Electrolyte Li7La3Zr2O12.* Chemistry of Materials, 2017. **29**(18): p. 7961-7968.
68. Sharafi, A., Yu, S., Naguib, M., Lee, M., Ma, C., Meyer, H.M., Nanda, J., Chi, M., Siegel, D.J., and Sakamoto, J., *Impact of air exposure and surface chemistry on Li–Li7La3Zr2O12 interfacial resistance.* Journal of Materials Chemistry A, 2017. **5**(26): p. 13475-13487.
69. Cheng, L., Wu, C.H., Jarry, A., Chen, W., Ye, Y., Zhu, J., Kostecki, R., Persson, K., Guo, J., Salmeron, M., Chen, G., and Doeff, M., *Interrelationships among Grain Size, Surface Composition, Air Stability, and Interfacial Resistance of Al-Substituted Li7La3Zr2O12 Solid Electrolytes.* ACS Applied Materials & Interfaces, 2015. **7**(32): p. 17649-17655.
70. Cheng, L., Crumlin, E.J., Chen, W., Qiao, R., Hou, H., Franz Lux, S., Zorba, V., Russo, R., Kostecki, R., Liu, Z., Persson, K., Yang, W., Cabana, J., Richardson, T., Chen, G., and Doeff, M., *The origin of high electrolyte–electrode interfacial resistances in lithium cells containing garnet type solid electrolytes.* Physical Chemistry Chemical Physics, 2014. **16**(34): p. 18294-18300.
71. Cheng, L., Park, J.S., Hou, H.M., Zorba, V., Chen, G.Y., Richardson, T., Cabana, J., Russo, R., and Doeff, M., *Effect of microstructure and surface impurity segregation on the electrical and electrochemical properties of dense Al-substituted Li7La3Zr2O12.* Journal of Materials Chemistry A, 2014. **2**(1): p. 172-181.
72. Xia, W., Xu, B., Duan, H., Guo, Y., Kang, H., Li, H., and Liu, H., *Ionic Conductivity and Air Stability of Al-Doped Li7La3Zr2O12 Sintered in Alumina and Pt Crucibles.* ACS Applied Materials & Interfaces, 2016. **8**(8): p. 5335-5342.
73. Xia, W., Xu, B., Duan, H., Tang, X., Guo, Y., Kang, H., Li, H., and Liu, H., *Reaction mechanisms of lithium garnet pellets in ambient air: The effect of humidity and CO2.* Journal of the American Ceramic Society, 2017. **100**(7): p. 2832-2839.

74. Nyman, M., Alam, T.M., McIntyre, S.K., Bleier, G.C., and Ingersoll, D., *Alternative Approach to Increasing Li Mobility in Li-La-Nb/Ta Garnet Electrolytes.* Chemistry of Materials, 2010. **22**(19): p. 5401-5410.
75. Galven, C., Dittmer, J., Suard, E., Le Berre, F., and Crosnier-Lopez, M.-P., *Instability of Lithium Garnets against Moisture. Structural Characterization and Dynamics of Li7-xHxLa3Sn2O12 and Li5-xHxLa3Nb2O12.* Chemistry of Materials, 2012. **24**(17): p. 3335-3345.
76. Truong, L., Colter, J., and Thangadurai, V., *Chemical stability of Li-stuffed garnet-type Li5+xBaxLa3-xTa2O12 (x=0, 0.5, 1) in water: a comparative analysis with the Nb analogue.* Solid State Ionics, 2013. **247**: p. 1-7.
77. Nemori, H., Matsuda, Y., Mitsuoka, S., Matsui, M., Yamamoto, O., Takeda, Y., and Imanishi, N., *Stability of garnet-type solid electrolyte LixLa3A2-yByO12 (A=Nb or Ta, B=Sc or Zr).* Solid State Ionics, 2015. **282**: p. 7-12.
78. Truong, L. and Thangadurai, V., *First Total H+/Li+ Ion Exchange in Garnet-Type Li5La3Nb2O12 Using Organic Acids and Studies on the Effect of Li Stuffing.* Inorganic Chemistry, 2012. **51**(3): p. 1222-1224.
79. Galven, C., Suard, E., Mounier, D., Crosnier-Lopez, M.-P., and Le Berre, F., *Structural characterization of a new acentric protonated garnet: Li6–xHxCaLa2Nb2O12.* Journal of Materials Research, 2013. **28**(16): p. 2147-2153.
80. Hofstetter, K., Samson, A.J., and Thangadurai, V., *Characterization of lithium-rich garnet-type Li6.5La2.5Ba0.5ZrTaO12 for beyond intercalation chemistry-based lithium-ion batteries.* Solid State Ionics, 2018. **318**: p. 71-81.
81. Yow, Z.F., Oh, Y.L., Gu, W.Y., Rao, R.P., and Adams, S., *Effect of Li+/H+ exchange in water treated Ta-doped Li7La3Zr2O12.* Solid State Ionics, 2016. **292**: p. 122-129.
82. Liu, C., Rui, K., Shen, C., Badding, M.E., Zhang, G.X., and Wen, Z.Y., *Reversible ion exchange and structural stability of garnet-type Nb-doped Li7La3Zr2O12 in water for applications in lithium batteries.* Journal of Power Sources, 2015. **282**: p. 286-293.
83. Galven, C., Fourquet, J.-L., Crosnier-Lopez, M.-P., and Le Berre, F., *Instability of the Lithium Garnet Li7La3Sn2O12: Li+/H+ Exchange and Structural Study.* Chemistry of Materials, 2011. **23**(7): p. 1892-1900.
84. Ma, C., Rangasamy, E., Liang, C., Sakamoto, J., More, K.L., and Chi, M., *Excellent Stability of a Lithium-Ion-Conducting Solid Electrolyte upon Reversible Li+/H+ Exchange in Aqueous Solutions (vol 54, pg 129, 2015).* Angewandte Chemie-International Edition, 2015. **54**(4): p. 1063-1063.
85. Orera, A., Larraz, G., Rodríguez-Velamazán, J.A., Campo, J., and Sanjuán, M.L., *Influence of Li+ and H+ Distribution on the Crystal Structure of Li7−xHxLa3Zr2O12 (0 ⩽ x ⩽ 5) Garnets.* Inorganic Chemistry, 2016. **55**(3): p. 1324-1332.
86. Li, Y., Han, J.-T., Vogel, S.C., and Wang, C.-A., *The reaction of Li6.5La3Zr1.5Ta0.5O12 with water.* Solid State Ionics, 2015. **269**: p. 57-61.
87. Hiebl, C., Young, D., Wagner, R., Wilkening, H.M.R., Redhammer, G.J., and Rettenwander, D., *Proton Bulk Diffusion in Cubic Li7La3Zr2O12 Garnets as Probed by Single X-ray Diffraction.* The Journal of Physical Chemistry C, 2019. **123**(2): p. 1094-1098.
88. Gam, F., Galven, C., Bulou, A., Le Berre, F., and Crosnier-Lopez, M.-P., *Reinvestigation of the Total Li+/H+ Ion Exchange on the Garnet-Type Li5La3Nb2O12.* Inorganic Chemistry, 2014. **53**(2): p. 931-934.
89. Kun, R., Langer, F., Delle Piane, M., Ohno, S., Zeier, W.G., Gockeln, M., Ciacchi, L.C., Busse, M., and Fekete, I., *Structural and Computational Assessment of the Influence of Wet-Chemical Post-Processing of the Al-Substituted Cubic Li7La3Zr2O12.* Acs Applied Materials & Interfaces, 2018. **10**(43): p. 37188-37197.

90. Truong, L. and Thangadurai, V., *Soft-Chemistry of Garnet-Type Li5+xBaxLa3-xNb2O12 (x=0, 0.5, 1): Reversible H+ <-> Li+ Ion-Exchange Reaction and Their X-ray, Li-7 MAS NMR, IR, and AC Impedance Spectroscopy Characterization.* Chemistry of Materials, 2011. **23**(17): p. 3970-3977.
91. Redhammer, G.J., Badami, P., Meven, M., Ganschow, S., Berendts, S., Tippelt, G., and Rettenwander, D., *Wet-Environment-Induced Structural Alterations in Single- and Polycrystalline LLZTO Solid Electrolytes Studied by Diffraction Techniques.* ACS Applied Materials & Interfaces, 2020. **13**(1): p. 350-359.
92. Liu, X.M., Chen, Y., Hood, Z.D., Ma, C., Yu, S.H., Sharafi, A., Wang, H., An, K., Sakamoto, J., Siegel, D.J., Cheng, Y.Q., Jalarvo, N.H., and Chi, M.F., *Elucidating the mobility of H+ and Li+ ions in (Li6.25-xHxAl0.25)La(3)Zr(2)O(12)via correlative neutron and electron spectroscopy.* Energy & Environmental Science, 2019. **12**(3): p. 945-951.
93. Sanjuán, M.L., Orera, A., Sobrados, I., Fuentes, A.F., and Sanz, J., *Structural transition in orthorhombic Li5−xHxLa3Nb2O12 garnets induced by a concerted lithium and proton diffusion mechanism.* Journal of Materials Chemistry A, 2018. **6**(6): p. 2708-2720.
94. Larraz, G., Orera, A., and Sanjuan, M.L., *Cubic phases of garnet-type Li7La3Zr2O12: the role of hydration.* Journal of Materials Chemistry A, 2013. **1**(37): p. 11419-11428.
95. Matsui, M., Takahashi, K., Sakamoto, K., Hirano, A., Takeda, Y., Yamamoto, O., and Imanishi, N., *Phase stability of a garnet-type lithium ion conductor Li7La3Zr2O12.* Dalton Transactions, 2014. **43**(3): p. 1019-1024.
96. Toda, S., Ishiguro, K., Shimonishi, Y., Hirano, A., Takeda, Y., Yamamoto, O., and Imanishi, N., *Low temperature cubic garnet-type CO2-doped Li7La3Zr2O12.* Solid State Ionics, 2013. **233**: p. 102-106.
97. Quinzeni, I., Capsoni, D., Berbenni, V., Mustarelli, P., Sturini, M., and Bini, M., *Stability of low-temperature Li7La3Zr2O12 cubic phase: The role of temperature and atmosphere.* Materials Chemistry and Physics, 2017. **185**: p. 55-64.
98. Ye, R., Tsai, C.-L., Ihrig, M., Sevinc, S., Rosen, M., Dashjav, E., Sohn, Y.J., Figgemeier, E., and Finsterbusch, M., *Water-based fabrication of garnet-based solid electrolyte separators for solid-state lithium batteries.* Green Chemistry, 2020. **22**: p. 4952-4961.
99. Uhlenbruck, S., Dellen, C., Moller, S., Lobe, S., Tsai, C.L., Finsterbusch, M., Bram, M., and Guillon, O., *Reactions of garnet-based solid-state lithium electrolytes with water - A depth-resolved study.* Solid State Ionics, 2018. **320**: p. 259-265.
100. Shimonishi, Y., Toda, A., Zhang, T., Hirano, A., Imanishi, N., Yamamoto, O., and Takeda, Y., *Synthesis of garnet-type Li7-xLa3Zr2O12-1/2x and its stability in aqueous solutions.* Solid State Ionics, 2011. **183**(1): p. 48-53.
101. Ishiguro, K., Nemori, H., Sunahiro, S., Nakata, Y., Sudo, R., Matsui, M., Takeda, Y., Yamamoto, O., and Imanishi, N., *Ta-Doped Li7La3Zr2O12 for Water-Stable Lithium Electrode of Lithium-Air Batteries.* Journal of the Electrochemical Society, 2014. **161**(5): p. A668-A674.
102. Narayanan, S., Ramezanipour, F., and Thangadurai, V., *Dopant Concentration−Porosity−Li-Ion Conductivity Relationship in Garnet-Type Li5+2xLa3Ta2−xYxO12 ($0.05 \leqslant x \leqslant 0.75$) and Their Stability in Water and 1 M LiCl.* Inorganic Chemistry, 2015. **54**(14): p. 6968-6977.
103. Li, Y., Prabhu, A.M., Choksi, T., and Canepa, P., *H2O and CO2 Surface Contamination of the Lithium-Stuffed Garnet.* Journal of Materials Chemistry A, 2022. **10**: p. 4960-4973.
104. Cheng, L., Liu, M., Mehta, A., Xin, H., Lin, F., Persson, K., Chen, G., Crumlin, E.J., and Doeff, M., *Garnet Electrolyte Surface Degradation and Recovery.* ACS Applied Energy Materials, 2018. **1**(12): p. 7244-7252.
105. Cai, J., Polzin, B., Fan, L., Yin, L., Liang, Y., Li, X., Liu, Q., Trask, S.E., Liu, Y., Ren, Y., Meng, X., and Chen, Z., *Stoichiometric Irreversibility of Aged Garnet Electrolytes.* Materials Today Energy, 2021: p. 100669.

106. Ohta, S., Kawakami, M., Nozaki, H., Yada, C., Saito, T., and Iba, H., *Li+ conducting garnet-type oxide sintering triggered by an H+/Li+ ion-exchange reaction.* Journal of Materials Chemistry A, 2020. **8**(18): p. 8989-8996.
107. Ihrig, M., Finsterbusch, M., Tsai, C.-L., Laptev, A.M., Tu, C.-h., Bram, M., Sohn, Y.J., Ye, R., Sevinc, S., Lin, S.-k., Fattakhova-Rohlfing, D., and Guillon, O., *Low temperature sintering of fully inorganic all-solid-state batteries – Impact of interfaces on full cell performance.* Journal of Power Sources, 2021. **482**: p. 228905.
108. Tsai, C.-L., Roddatis, V., Chandran, C.V., Ma, Q., Uhlenbruck, S., Bram, M., Heitjans, P., and Guillon, O., *Li7La3Zr2O12 Interface Modification for Li Dendrite Prevention.* ACS Applied Materials & Interfaces, 2016. **8**(16): p. 10617-10626.
109. Ihrig, M., Mishra, T.P., Scheld, W.S., Häuschen, G., Rheinheimer, W., Bram, M., Finsterbusch, M., and Guillon, O., *Li7La3Zr2O12 solid electrolyte sintered by the ultrafast high-temperature method.* Journal of the European Ceramic Society, 2021. **41**(12): p. 6075-6079.
110. Yi, E.Y., Wang, W.M., Kieffer, J., and Laine, R.M., *Flame made nanoparticles permit processing of dense, flexible, Li+ conducting ceramic electrolyte thin films of cubic-Li7La3Zr2O12 (c-LLZO).* Journal of Materials Chemistry A, 2016. **4**(33): p. 12947-12954.
111. Yi, E.Y., Wang, W.M., Kieffer, J., and Laine, R.M., *Key parameters governing the densification of cubic-Li7La3Zr2O12 Li+ conductors.* Journal of Power Sources, 2017. **352**: p. 156-164.
112. Fu, K., Gong, Y.H., Hitz, G.T., McOwen, D.W., Li, Y.J., Xu, S.M., Wen, Y., Zhang, L., Wang, C.W., Pastel, G., Dai, J.Q., Liu, B.Y., Xie, H., Yao, Y.G., Wachsman, E.D., and Hu, L.B., *Three-dimensional bilayer garnet solid electrolyte based high energy density lithium metal-sulfur batteries.* Energy & Environmental Science, 2017. **10**(7): p. 1568-1575.
113. Liu, B., Zhang, L., Xu, S., McOwen, D.W., Gong, Y., Yang, C., Pastel, G.R., Xie, H., Fu, K., Dai, J., Chen, C., Wachsman, E.D., and Hu, L., *3D lithium metal anodes hosted in asymmetric garnet frameworks toward high energy density batteries.* Energy Storage Materials, 2018. **14**: p. 376-382.
114. Hitz, G.T., McOwen, D.W., Zhang, L., Ma, Z.H., Fu, Z.Z., Wen, Y., Gong, Y.H., Dai, J.Q., Hamann, T.R., Hu, L.B., and Wachsman, E.D., *High-rate lithium cycling in a scalable trilayer Li-garnet-electrolyte architecture.* Materials Today, 2019. **22**: p. 50-57.
115. Jonson, R.A. and McGinn, P.J., *Tape casting and sintering of Li7La3Zr1.75Nb0.25Al0.1O12 with Li3BO3 additions.* Solid State Ionics, 2018. **323**: p. 49-55.
116. Hanc, E., Zajac, W., Lu, L., Yan, B.G., Kotobuki, M., Ziabka, M., and Molenda, J., *On fabrication procedures of Li-ion conducting garnets.* Journal of Solid State Chemistry, 2017. **248**: p. 51-60.
117. Cheng, L.S.J., CA, US), Iyer, Sriram (San Jose, CA, US), Gardner, Will (San Jose, CA, US), Holme, Tim (San Jose, CA, US), Li, Shuang (San Jose, CA, US), Chao, Cheng-chieh (San Jose, CA, US), Donnelly, Niall (San Jose, CA, US), Allenic, Arnold (San Jose, CA, US), *Annealed garnet electrolyte separators*. 2018, QuantumScape Corporation (San Jose, CA, US): United States.
118. Gao, K.N., He, M.H., Li, Y.Q., Zhang, Y.P., Gao, J., Li, X.X., Cui, Z.H., Zhan, Z.L., and Zhang, T., *Preparation of high-density garnet thin sheet electrolytes for all-solid-state Li-Metal batteries by tape-casting technique.* Journal of Alloys and Compounds, 2019. **791**: p. 923-928.
119. Badding, M.E.C., NY, US), Chen, Yinghong (Painted Post, NY, US), Huang, Xiao (Shanghai, CN), Liu, Cai (Suzhou-Si, CN), Liu, Xinyuan (Painted Post, NY, US), Lu, Yanxia Ann (Painted Post, NY, US), Song, Zhen (Painted Post, NY, US), Wen, Zhaoyin (Shanghai, CN), Xiu, Tongping (Shanghai, CN), Zink, Nathan Michael (Painted Post, NY, US), *LITHIUM-GARNET SOLID ELECTROLYTE COMPOSITE, TAPE ARTICLES, AND METHODS THEREOF*. 2018, CORNING INCORPORATED (CORNING, NY, US),SHANGHAI INSTITUTE OF CERAMICS, CHINESE ACADEMY OF SCIENCES (SHANGHAI, CN): United States.
120. Jin, Y. and McGinn, P.J., *Li7La3Zr2O12 electrolyte stability in air and fabrication of a Li/Li7La3Zr2O12/Cu0.1V2O5 solid-state battery.* Journal of Power Sources, 2013. **239**: p. 326-331.

121. Peng, X., Zhang, X.K., Huang, K., Song, S.P., and Xiang, Y., *A Novel Aqueous-based Gelcasting Process to Fabricate Li6.4La3Zr1.4Ta0.6O12 Solid Electrolytes.* Chemelectrochem, 2019. **6**(11): p. 2945-2948.
122. Wood, M., Gao, X., Shi, R., Heo, T.W., Espitia, J.A., Duoss, E.B., Wood, B.C., and Ye, J., *Exploring the relationship between solvent-assisted ball milling, particle size, and sintering temperature in garnet-type solid electrolytes.* Journal of Power Sources, 2021. **484**: p. 229252.
123. Huang, X., Lu, Y., Tin, J., Gu, S., Xiu, T.P., Song, Z., Badding, M.E., and Wen, Z.Y., *Method Using Water-Based Solvent to Prepare Li7La3Zr2O12 Solid Electrolytes.* Acs Applied Materials & Interfaces, 2018. **10**(20): p. 17147-17155.
124. Buannic, L., Naviroj, M., Miller, S.M., Zagorski, J., Faber, K.T., and Llordes, A., *Dense freeze-cast Li7La3Zr2O12 solid electrolytes with oriented open porosity and contiguous ceramic scaffold.* Journal of the American Ceramic Society, 2019. **102**(3): p. 1021-1029.
125. Shen, H., Yi, E., Amores, M., Cheng, L., Tamura, N., Parkinson, D.Y., Chen, G., Chen, K., and Doeff, M., *Oriented porous LLZO 3D structures obtained by freeze casting for battery applications.* Journal of Materials Chemistry A, 2019. **7**(36): p. 20861-20870.
126. Shen, F., Guo, W., Zeng, D., Sun, Z., Gao, J., Li, J., Zhao, B., He, B., and Han, X., *A Simple and Highly Efficient Method toward High-Density Garnet-Type LLZTO Solid-State Electrolyte.* ACS Applied Materials & Interfaces, 2020. **12**(27): p. 30313-30319.
127. Yi, E., Shen, H., Heywood, S., Alvarado, J., Parkinson, D.Y., Chen, G., Sofie, S.W., and Doeff, M.M., *All-Solid-State Batteries Using Rationally Designed Garnet Electrolyte Frameworks.* ACS Applied Energy Materials, 2020. **3**(1): p. 170-175.
128. Miara, L., Windmuller, A., Tsai, C.L., Richards, W.D., Ma, Q.L., Uhlenbruck, S., Guillon, O., and Ceder, G., *About the Compatibility between High Voltage Spinel Cathode Materials and Solid Oxide Electrolytes as a Function of Temperature.* Acs Applied Materials & Interfaces, 2016. **8**(40): p. 26842-26850.
129. Miara, L.J., Richards, W.D., Wang, Y.E., and Ceder, G., *First-Principles Studies on Cation Dopants and Electrolyte|Cathode Interphases for Lithium Garnets.* Chemistry of Materials, 2015. **27**(11): p. 4040-4047.
130. Wang, X., Wang, J., Li, F., Zhu, F., and Ma, C., *Influence of cold sintering process on the structure and properties of garnet-type solid electrolytes.* Ceramics International, 2020. **46**(11, Part B): p. 18544-18550.
131. Tsai, C.-L., Yu, S., Tempel, H., Kungl, H., and Eichel, R.-A., *All-ceramic Li batteries based on garnet structured Li7La3Zr2O12.* Materials Technology, 2020. **35**(9-10): p. 656-674.
132. Huo, H., Luo, J., Thangadurai, V., Guo, X., Nan, C.-W., and Sun, X., *Li2CO3: A Critical Issue for Developing Solid Garnet Batteries.* ACS Energy Letters, 2020. **5**(1): p. 252-262.
133. Yang, L., Lu, Z., Qin, Y., Wu, C., Fu, C., Gao, Y., Liu, J., Jiang, L., Du, Z., Xie, Z., Li, Z., Kong, F., and Yin, G., *Interrelated interfacial issues between a Li7La3Zr2O12-based garnet electrolyte and Li anode in the solid-state lithium battery: a review.* Journal of Materials Chemistry A, 2021. **9**(10): p. 5952-5979.
134. Li, Y., Chen, X., Dolocan, A., Cui, Z., Xin, S., Xue, L., Xu, H., Park, K., and Goodenough, J.B., *Garnet Electrolyte with an Ultralow Interfacial Resistance for Li-Metal Batteries.* Journal of the American Chemical Society, 2018. **140**(20): p. 6448-6455.
135. Huo, H., Chen, Y., Zhao, N., Lin, X., Luo, J., Yang, X., Liu, Y., Guo, X., and Sun, X., *In-situ formed Li2CO3-free garnet/Li interface by rapid acid treatment for dendrite-free solid-state batteries.* Nano Energy, 2019. **61**: p. 119-125.
136. Ruan, Y.D., Lu, Y., Huang, X., Su, J.M., Sun, C.Z., Jin, J., and Wen, Z.Y., *Acid induced conversion towards a robust and lithiophilic interface for Li-Li7La3Zr2O12 solid-state batteries.* Journal of Materials Chemistry A, 2019. **7**(24): p. 14565-14574.

137. Duan, H., Chen, W.-P., Fan, M., Wang, W.-P., Yu, L., Tan, S.-J., Chen, X., Zhang, Q., Xin, S., Wan, L.-J., and Guo, Y.-G., *Building an Air Stable and Lithium Deposition Regulable Garnet Interface from Moderate-Temperature Conversion Chemistry.* Angewandte Chemie International Edition, 2020. **59**(29): p. 12069-12075.
138. Ruan, Y., Lu, Y., Li, Y., Zheng, C., Su, J., Jin, J., Xiu, T., Song, Z., Badding, M.E., and Wen, Z., *A 3D Cross-Linking Lithiophilic and Electronically Insulating Interfacial Engineering for Garnet-Type Solid-State Lithium Batteries.* Advanced Functional Materials, 2021. **31**(5): p. 2007815.
139. Nagao, M., Hayashi, A., and Tatsumisago, M., *Bulk-Type Lithium Metal Secondary Battery with Indium Thin Layer at Interface between Li Electrode and Li2S-P2S5 Solid Electrolyte.* Electrochemistry, 2012. **80**(10): p. 734-736.
140. Feng, W., Dong, X., Li, P., Wang, Y., and Xia, Y., *Interfacial modification of Li/Garnet electrolyte by a lithiophilic and breathing interlayer.* Journal of Power Sources, 2019. **419**: p. 91-98.
141. Fu, K., Gong, Y., Fu, Z., Xie, H., Yao, Y., Liu, B., Carter, M., Wachsman, E., and Hu, L., *Transient Behavior of the Metal Interface in Lithium Metal–Garnet Batteries.* Angewandte Chemie International Edition, 2017. **56**(47): p. 14942-14947.
142. Fu, K.K., Gong, Y.H., Liu, B.Y., Zhu, Y.Z., Xu, S.M., Yao, Y.G., Luo, W., Wang, C.W., Lacey, S.D., Dai, J.Q., Chen, Y.N., Mo, Y.F., Wachsman, E., and Hu, L.B., *Toward garnet electrolyte-based Li metal batteries: An ultrathin, highly effective, artificial solid-state electrolyte/metallic Li interface.* Science Advances, 2017. **3**(4): p. e1601659.
143. He, M., Cui, Z., Chen, C., Li, Y., and Guo, X., *Formation of self-limited, stable and conductive interfaces between garnet electrolytes and lithium anodes for reversible lithium cycling in solid-state batteries.* Journal of Materials Chemistry A, 2018. **6**(24): p. 11463-11470.
144. Luo, W., Gong, Y.H., Zhu, Y.Z., Li, Y.J., Yao, Y.G., Zhang, Y., Fu, K., Pastel, G., Lin, C.F., Mo, Y.F., Wachsman, E.D., and Hu, L.B., *Reducing Interfacial Resistance between Garnet-Structured Solid-State Electrolyte and Li-Metal Anode by a Germanium Layer.* Advanced Materials, 2017. **29**(22).
145. Luo, W., Gong, Y., Zhu, Y., Fu, K.K., Dai, J., Lacey, S.D., Wang, C., Liu, B., Han, X., Mo, Y., Wachsman, E.D., and Hu, L., *Transition from Superlithiophobicity to Superlithiophilicity of Garnet Solid-State Electrolyte.* Journal of the American Chemical Society, 2016. **138**(37): p. 12258-12262.
146. Shao, Y., Wang, H., Gong, Z., Wang, D., Zheng, B., Zhu, J., Lu, Y., Hu, Y.-S., Guo, X., Li, H., Huang, X., Yang, Y., Nan, C.-W., and Chen, L., *Drawing a Soft Interface: An Effective Interfacial Modification Strategy for Garnet-Type Solid-State Li Batteries.* ACS Energy Letters, 2018. **3**(6): p. 1212-1218.
147. Alexander, G.V., Indu, M.S., Kamakshy, S., and Murugan, R., *Development of stable and conductive interface between garnet structured solid electrolyte and lithium metal anode for high performance solid-state battery.* Electrochimica Acta, 2020. **332**: p. 135511.
148. Han, X., Gong, Y., Fu, K., He, X., Hitz, G.T., Dai, J., Pearse, A., Liu, B., Wang, H., Rubloff, G., Mo, Y., Thangadurai, V., Wachsman, E.D., and Hu, L., *Negating interfacial impedance in garnet-based solid-state Li metal batteries.* Nature Materials, 2017. **16**(5): p. 572-579.
149. Liu, K., Zhang, R., Wu, M., Jiang, H., and Zhao, T., *Ultra-stable lithium plating/stripping in garnet-based lithium-metal batteries enabled by a SnO2 nanolayer.* Journal of Power Sources, 2019. **433**: p. 226691.
150. Li, Y., Li, Y., Yang, Y., Cui, Z., Wang, J., and Zhang, T., *Conversion inorganic interlayer of a LiF/graphene composite in all-solid-state lithium batteries.* Chemical Communications, 2020. **56**(11): p. 1725-1728.
151. Wang, C., Gong, Y., Liu, B., Fu, K., Yao, Y., Hitz, E., Li, Y., Dai, J., Xu, S., Luo, W., Wachsman, E.D., and Hu, L., *Conformal, Nanoscale ZnO Surface Modification of Garnet-Based Solid-State Electrolyte for Lithium Metal Anodes.* Nano Letters, 2017. **17**(1): p. 565-571.

152. Zhang, L., Yang, J., Jing, K., Li, C., Gao, Y., Wang, X., and Fang, Q., *Thickness-Dependent Beneficial Effect of the ZnO Layer on Tailoring the Li/Li7La3Zr2O12 Interface.* ACS Applied Materials & Interfaces, 2020. **12**(12): p. 13836-13841.
153. Lou, J., Wang, G., Xia, Y., Liang, C., Huang, H., Gan, Y., Tao, X., Zhang, J., and Zhang, W., *Achieving efficient and stable interface between metallic lithium and garnet-type solid electrolyte through a thin indium tin oxide interlayer.* Journal of Power Sources, 2020. **448**: p. 227440.
154. Xu, H., Li, Y., Zhou, A., Wu, N., Xin, S., Li, Z., and Goodenough, J.B., *Li3N-Modified Garnet Electrolyte for All-Solid-State Lithium Metal Batteries Operated at 40 °C.* Nano Letters, 2018. **18**(11): p. 7414-7418.
155. Huo, H., Chen, Y., Li, R., Zhao, N., Luo, J., Pereira da Silva, J.G., Mücke, R., Kaghazchi, P., Guo, X., and Sun, X., *Design of a mixed conductive garnet/Li interface for dendrite-free solid lithium metal batteries.* Energy & Environmental Science, 2020. **13**(1): p. 127-134.
156. Huang, Y., Chen, B., Duan, J., Yang, F., Wang, T., Wang, Z., Yang, W., Hu, C., Luo, W., and Huang, Y., *Graphitic Carbon Nitride (g-C3N4): An Interface Enabler for Solid-State Lithium Metal Batteries.* Angewandte Chemie International Edition, 2020. **59**(9): p. 3699-3704.
157. Fu, J., Yu, P., Zhang, N., Ren, G., Zheng, S., Huang, W., Long, X., Li, H., and Liu, X., *In situ formation of a bifunctional interlayer enabled by a conversion reaction to initiatively prevent lithium dendrites in a garnet solid electrolyte.* Energy & Environmental Science, 2019. **12**(4): p. 1404-1412.
158. Lapp, T., Skaarup, S., and Hooper, A., *Ionic conductivity of pure and doped Li3N.* Solid State Ionics, 1983. **11**(2): p. 97-103.
159. Park, K. and Goodenough, J.B., *Dendrite-Suppressed Lithium Plating from a Liquid Electrolyte via Wetting of Li3N.* Advanced Energy Materials, 2017. **7**(19): p. 1700732.
160. Li, W., Wu, G., Araújo, C.M., Scheicher, R.H., Blomqvist, A., Ahuja, R., Xiong, Z., Feng, Y., and Chen, P., *Li+ ion conductivity and diffusion mechanism in α-Li3N and ß-Li3N.* Energy & Environmental Science, 2010. **3**(10): p. 1524-1530.
161. Li, Y., Sun, Y., Pei, A., Chen, K., Vailionis, A., Li, Y., Zheng, G., Sun, J., and Cui, Y., *Robust Pinhole-free Li3N Solid Electrolyte Grown from Molten Lithium.* ACS Central Science, 2018. **4**(1): p. 97-104.
162. Ma, X., Xu, Y., Zhang, B., Xue, X., Wang, C., He, S., Lin, J., and Yang, L., *Garnet Si–Li7La3Zr2O12 electrolyte with a durable, low resistance interface layer for all-solid-state lithium metal batteries.* Journal of Power Sources, 2020. **453**: p. 227881.
163. Zhou, W., Wang, S., Li, Y., Xin, S., Manthiram, A., and Goodenough, J.B., *Plating a Dendrite-Free Lithium Anode with a Polymer/Ceramic/Polymer Sandwich Electrolyte.* Journal of the American Chemical Society, 2016. **138**(30): p. 9385-9388.
164. Zhou, W., Zhu, Y., Grundish, N., Sen, X., Wang, S., You, Y., Wu, N., Gao, J., Cui, Z., Li, Y., and Goodenough, J.B., *Polymer lithium-garnet interphase for an all-solid-state rechargeable battery.* Nano Energy, 2018. **53**: p. 926-931.
165. Chen, L., Huang, Z., Pang, W., Jin, Z., Li, Y., and Wang, C.-A., *Dual interface layers for solid-state Li metal battery with low interfacial resistance and small polarization based on garnet electrolyte.* Electrochimica Acta, 2020. **330**: p. 135352.
166. Ren, Y., Liu, T., Shen, Y., Lin, Y., and Nan, C.-W., *Chemical compatibility between garnet-like solid state electrolyte Li6.75La3Zr1.75Ta0.25O12 and major commercial lithium battery cathode materials.* Journal of Materiomics, 2016. **2**(3): p. 256-264.
167. Wakasugi, J., Munakata, H., and Kanamura, K., *Thermal Stability of Various Cathode Materials against Li6.25Al0.25La3Zr2O12 Electrolyte.* Electrochemistry, 2017. **85**(2): p. 77-81.
168. Tsai, C.-L., Ma, Q., Dellen, C., Lobe, S., Vondahlen, F., Windmüller, A., Grüner, D., Zheng, H., Uhlenbruck, S., Finsterbusch, M., Tietz, F., Fattakhova-Rohlfing, D., Buchkremer, H.P., and Guillon, O., *A garnet structure-based all-solid-state Li battery without interface modification: resolving incompatibility issues on positive electrodes.* Sustainable Energy & Fuels, 2019. **3**(1): p. 280-291.

169. Park, K., Yu, B.-C., Jung, J.-W., Li, Y., Zhou, W., Gao, H., Son, S., and Goodenough, J.B., *Electrochemical Nature of the Cathode Interface for a Solid-State Lithium-Ion Battery: Interface between LiCoO2 and Garnet-Li7La3Zr2O12.* Chemistry of Materials, 2016. **28**(21): p. 8051-8059.
170. Han, F., Yue, J., Chen, C., Zhao, N., Fan, X., Ma, Z., Gao, T., Wang, F., Guo, X., and Wang, C., *Interphase Engineering Enabled All-Ceramic Lithium Battery*. Joule, 2018. **2**(3): p. 497-508.
171. Laptev, A.M., Zheng, H., Bram, M., Finsterbusch, M., and Guillon, O., *High-pressure field assisted sintering of half-cell for all-solid-state battery.* Materials Letters, 2019. **247**: p. 155-158.
172. Ihrig, M., Ye, R., Laptev, A.M., Grüner, D., Guerdelli, R., Scheld, W.S., Finsterbusch, M., Wiemhöfer, H.-D., Fattakhova-Rohlfing, D., and Guillon, O., *Polymer–Ceramic Composite Cathode with Enhanced Storage Capacity Manufactured by Field-Assisted Sintering and Infiltration.* ACS Applied Energy Materials, 2021. **4**(10): p. 10428-10432.
173. Ren, Y., Liu, T., Shen, Y., Lin, Y., and Nan, C.-W., *Garnet-type oxide electrolyte with novel porous-dense bilayer configuration for rechargeable all-solid-state lithium batteries.* Ionics, 2017. **23**(9): p. 2521-2527.
174. Kim, K. and Rupp, J.L.M., *All Ceramic Cathode Composite Design and Manufacturing towards Low Interfacial Resistance for Garnet-Based Solid-State Batteries.* Energy & Environmental Science, 2020. **13**: p. 4930-4945.
175. Du, F., Zhao, N., Li, Y., Chen, C., Liu, Z., and Guo, X., *All solid state lithium batteries based on lamellar garnet-type ceramic electrolytes.* Journal of Power Sources, 2015. **300**: p. 24-28.
176. Chen, C., Li, Q., Li, Y., Cui, Z., Guo, X., and Li, H., *Sustainable Interfaces between Si Anodes and Garnet Electrolytes for Room-Temperature Solid-State Batteries.* ACS Applied Materials & Interfaces, 2018. **10**(2): p. 2185-2190.
177. Deng, T., Ji, X., Zhao, Y., Cao, L., Li, S., Hwang, S., Luo, C., Wang, P., Jia, H., Fan, X., Lu, X., Su, D., Sun, X., Wang, C., and Zhang, J.-G., *Tuning the Anode–Electrolyte Interface Chemistry for Garnet-Based Solid-State Li Metal Batteries.* Advanced Materials, 2020. **32**(23): p. 2000030.
178. Lei, Z., Chen, B., Koo, Y.-M., and MacFarlane, D.R., *Introduction: Ionic Liquids.* Chemical Reviews, 2017. **117**(10): p. 6633-6635.
179. Watanabe, M., Thomas, M.L., Zhang, S., Ueno, K., Yasuda, T., and Dokko, K., *Application of Ionic Liquids to Energy Storage and Conversion Materials and Devices.* Chemical Reviews, 2017. **117**(10): p. 7190-7239.
180. Jiang, Z., Wang, S., Chen, X., Yang, W., Yao, X., Hu, X., Han, Q., and Wang, H., *Tape-Casting Li0.34La0.56TiO3 Ceramic Electrolyte Films Permit High Energy Density of Lithium-Metal Batteries.* Advanced Materials, 2020. **32**(6): p. 1906221.
181. Du, M., Sun, Y., Liu, B., Chen, B., Liao, K., Ran, R., Cai, R., Zhou, W., and Shao, Z., *Smart Construction of an Intimate Lithium | Garnet Interface for All-Solid-State Batteries by Tuning the Tension of Molten Lithium.* Advanced Functional Materials, 2021. **31**: p. 2101556.
182. Zhou, Q., Xu, B., Chien, P.-H., Li, Y., Huang, B., Wu, N., Xu, H., Grundish, N.S., Hu, Y.-Y., and Goodenough, J.B., *NASICON Li1.2Mg0.1Zr1.9(PO4)3 Solid Electrolyte for an All-Solid-State Li-Metal Battery*. Small Methods, 2020. 4: p. 2000764.
183. Chen, R.-J., Zhang, Y.-B., Liu, T., Xu, B.-Q., Lin, Y.-H., Nan, C.-W., and Shen, Y., *Addressing the Interface Issues in All-Solid-State Bulk-Type Lithium Ion Battery via an All-Composite Approach.* ACS Applied Materials & Interfaces, 2017. **9**(11): p. 9654-9661.
184. Kitano, H., Ichikawa, K., Ide, M., Fukuda, M., and Mizuno, W., *Fourier Transform Infrared Study on the State of Water Sorbed to Poly(ethylene glycol) Films.* Langmuir, 2001. **17**(6): p. 1889-1895.
185. Hammouda, B., Ho, D.L., and Kline, S., *Insight into Clustering in Poly(ethylene oxide) Solutions.* Macromolecules, 2004. **37**(18): p. 6932-6937.
186. Hammouda, B., *Solvation characteristics of a model water-soluble polymer.* Journal of Polymer Science Part B: Polymer Physics, 2006. **44**(22): p. 3195-3199.

187. Yang, X., Jiang, M., Gao, X., Bao, D., Sun, Q., Holmes, N., Duan, H., Mukherjee, S., Adair, K., Zhao, C., Liang, J., Li, W., Li, J., Liu, Y., Huang, H., Zhang, L., Lu, S., Lu, Q., Li, R., Singh, C.V., and Sun, X., *Determining the limiting factor of the electrochemical stability window for PEO-based solid polymer electrolytes: main chain or terminal –OH group?* Energy & Environmental Science, 2020. **13**(5): p. 1318-1325.
188. Hotza, D. and Greil, P., *Review: aqueous tape casting of ceramic powders.* Materials Science and Engineering: A, 1995. **202**(1): p. 206-217.
189. Jabbari, M., Bulatova, R., Tok, A.I.Y., Bahl, C.R.H., Mitsoulis, E., and Hattel, J.H., *Ceramic tape casting: A review of current methods and trends with emphasis on rheological behaviour and flow analysis.* Materials Science and Engineering: B, 2016. **212**: p. 39-61.
190. Nishihora, R.K., Rachadel, P.L., Quadri, M.G.N., and Hotza, D., *Manufacturing porous ceramic materials by tape casting—A review.* Journal of the European Ceramic Society, 2018. **38**(4): p. 988-1001.
191. Lin, D., Liu, W., Liu, Y., Lee, H.R., Hsu, P.-C., Liu, K., and Cui, Y., *High Ionic Conductivity of Composite Solid Polymer Electrolyte via In Situ Synthesis of Monodispersed SiO2 Nanospheres in Poly(ethylene oxide).* Nano Letters, 2016. **16**(1): p. 459-465.
192. Wang, C., Yang, T., Zhang, W., Huang, H., Gan, Y., Xia, Y., He, X., and Zhang, J., *Hydrogen bonding enhanced SiO2/PEO composite electrolytes for solid-state lithium batteries.* Journal of Materials Chemistry A, 2022.
193. Rahaman, M.H., *Ceramic Processing and Sintering*. 2nd ed. 2003: CRC Press.
194. Merkus, H.G., *Laser Diffraction*, in *Particle Size Measurements: Fundamentals, Practice, Quality*, H.G. Merkus, Editor. 2009, Springer Netherlands: Dordrecht. p. 259-285.
195. Mie, G., *Beiträge zur Optik trüber Medien, speziell kolloidaler Metallösungen.* Annalen der Physik, 1908. **330**(3): p. 377-445.
196. Mewis, J., *Rheology of Suspensions*, in *Rheology: Volume 1: Principles*, G. Astarita, G. Marrucci, and L. Nicolais, Editors. 1980, Springer US: Boston, MA. p. 149-168.
197. Malkin, A.Y. and Isayev, A.I., *5 - RHEOMETRY EXPERIMENTAL METHODS*, in *Rheology Concepts, Methods, and Applications (Second Edition)*, A.Y. Malkin and A.I. Isayev, Editors. 2012, Elsevier: Oxford. p. 255-364.
198. Waseda, Y., Matsubara, E., and Shinoda, K., *Scattering and Diffraction*, in *X-Ray Diffraction Crystallography: Introduction, Examples and Solved Problems*, Y. Waseda, E. Matsubara, and K. Shinoda, Editors. 2011, Springer Berlin Heidelberg: Berlin, Heidelberg. p. 67-106.
199. Bragg, W.H. and Bragg, W.L., *The reflection of X-rays by crystals.* Proceedings of the Royal Society of London. Series A, Containing Papers of a Mathematical and Physical Character, 1913. **88**(605): p. 428-438.
200. Waseda, Y., Matsubara, E., and Shinoda, K., *Diffraction from Polycrystalline Samples and Determination of Crystal Structure*, in *X-Ray Diffraction Crystallography: Introduction, Examples and Solved Problems*, Y. Waseda, E. Matsubara, and K. Shinoda, Editors. 2011, Springer Berlin Heidelberg: Berlin, Heidelberg. p. 107-167.
201. Rietveld, H., *A profile refinement method for nuclear and magnetic structures.* Journal of Applied Crystallography, 1969. **2**(2): p. 65-71.
202. Ul-Hamid, A., *Contrast Formation in the SEM*, in *A Beginners' Guide to Scanning Electron Microscopy*, A. Ul-Hamid, Editor. 2018, Springer International Publishing: Cham. p. 77-128.
203. Ul-Hamid, A., *Characteristics of X-Rays*, in *A Beginners' Guide to Scanning Electron Microscopy*, A. Ul-Hamid, Editor. 2018, Springer International Publishing: Cham. p. 233-264.
204. Thompson, M. and Walsh, J.N., *Introduction*, in *Handbook of Inductively Coupled Plasma Spectrometry*, M. Thompson and J.N. Walsh, Editors. 1989, Springer US: Boston, MA. p. 1-15.

205. Haines, P.J., *Thermogravimetry*, in *Thermal Methods of Analysis: Principles, Applications and Problems*, P.J. Haines, Editor. 1995, Springer Netherlands: Dordrecht. p. 22-62.
206. Haines, P.J., *Simultaneous techniques and product analysis*, in *Thermal Methods of Analysis: Principles, Applications and Problems*, P.J. Haines, Editor. 1995, Springer Netherlands: Dordrecht. p. 161-205.
207. Gardiner, D.J., *Introduction to Raman Scattering*, in *Practical Raman Spectroscopy*, D.J. Gardiner and P.R. Graves, Editors. 1989, Springer Berlin Heidelberg: Berlin, Heidelberg. p. 1-12.
208. Woodward, L.A., *Vibrational Rules of Selection and Polarization: Their Practical Uses and Limitations*, in *Raman Spectroscopy: Theory and Practice*, H.A. Szymanski, Editor. 1970, Springer US: Boston, MA. p. 1-31.
209. Abidi, N., *Introduction to FTIR Microspectroscopy*, in *FTIR Microspectroscopy : Selected Emerging Applications*, N. Abidi, Editor. 2021, Springer International Publishing: Cham. p. 1-12.
210. Lasia, A., *Definition of Impedance and Impedance of Electrical Circuits*, in *Electrochemical Impedance Spectroscopy and its Applications*, A. Lasia, Editor. 2014, Springer New York: New York, NY. p. 7-66.
211. Vivier, V. and Orazem, M.E., *Impedance Analysis of Electrochemical Systems.* Chemical Reviews, 2022. **122**(12): p. 11131-11168.
212. Wang, S., Zhang, J., Gharbi, O., Vivier, V., Gao, M., and Orazem, M.E., *Electrochemical impedance spectroscopy.* Nature Reviews Methods Primers, 2021. **1**(1): p. 41.
213. Irvine, J.T.S., Sinclair, D.C., and West, A.R., *Electroceramics: Characterization by Impedance Spectroscopy.* Advanced Materials, 1990. **2**(3): p. 132-138.
214. Elgrishi, N., Rountree, K.J., McCarthy, B.D., Rountree, E.S., Eisenhart, T.T., and Dempsey, J.L., *A Practical Beginner's Guide to Cyclic Voltammetry.* Journal of Chemical Education, 2018. **95**(2): p. 197-206.
215. Scholz, F., *Voltammetric techniques of analysis: the essentials.* ChemTexts, 2015. **1**(4): p. 17.
216. Holze, R., *Experimental Electrochemistry: A Laboratory Textbook*. 2019: Wiley.
217. Geiger, C.A., Alekseev, E., Lazic, B., Fisch, M., Armbruster, T., Langner, R., Fechtelkord, M., Kim, N., Pettke, T., and Weppner, W., *Crystal Chemistry and Stability of "Li7La3Zr2O12" Garnet: A Fast Lithium-Ion Conductor.* Inorganic Chemistry, 2011. **50**(3): p. 1089-1097.
218. Nasatto, P.L., Pignon, F., Silveira, J.L.M., Duarte, M.E.R., Noseda, M.D., and Rinaudo, M., *Methylcellulose, a Cellulose Derivative with Original Physical Properties and Extended Applications.* Polymers, 2015. **7**(5): p. 777-803.
219. Weller, J.M., Whetten, J.A., and Chan, C.K., *Nonaqueous Polymer Combustion Synthesis of Cubic Li7La3Zr2O12 Nanopowders.* ACS Applied Materials & Interfaces, 2020. **12**(1): p. 953-962.
220. Pasierb, P., Komornicki, S., Rokita, M., and Rękas, M., *Structural properties of Li2CO3–BaCO3 system derived from IR and Raman spectroscopy.* Journal of Molecular Structure, 2001. **596**(1): p. 151-156.
221. Huang, X., Liu, C., Lu, Y., Xiu, T., Jin, J., Badding, M.E., and Wen, Z., *A Li-Garnet composite ceramic electrolyte and its solid-state Li-S battery.* Journal of Power Sources, 2018. **382**: p. 190-197.
222. Huang, X., Lu, Y., Song, Z., Xiu, T., Badding, M.E., and Wen, Z., *Preparation of dense Ta-LLZO/MgO composite Li-ion solid electrolyte: Sintering, microstructure, performance and the role of MgO.* Journal of Energy Chemistry, 2019. **39**: p. 8-16.
223. Hodge, I.M., Ingram, M.D., and West, A.R., *Impedance and modulus spectroscopy of polycrystalline solid electrolytes.* Journal of Electroanalytical Chemistry and Interfacial Electrochemistry, 1976. **74**(2): p. 125-143.
224. Santhosha, A.L., Medenbach, L., Buchheim, J.R., and Adelhelm, P., *The Indium–Lithium Electrode in Solid-State Lithium-Ion Batteries: Phase Formation, Redox Potentials, and Interface Stability.* Batteries & Supercaps, 2019. **2**(6): p. 524-529.

225. Han, F., Zhu, Y., He, X., Mo, Y., and Wang, C., *Electrochemical Stability of Li10GeP2S12 and Li7La3Zr2O12 Solid Electrolytes.* Advanced Energy Materials, 2016. **6**(8): p. 1501590.
226. Thompson, T., Yu, S., Williams, L., Schmidt, R.D., Garcia-Mendez, R., Wolfenstine, J., Allen, J.L., Kioupakis, E., Siegel, D.J., and Sakamoto, J., *Electrochemical Window of the Li-Ion Solid Electrolyte Li7La3Zr2O12.* ACS Energy Letters, 2017. **2**(2): p. 462-468.
227. Krauskopf, T., Hartmann, H., Zeier, W.G., and Janek, J., *Toward a Fundamental Understanding of the Lithium Metal Anode in Solid-State Batteries—An Electrochemo-Mechanical Study on the Garnet-Type Solid Electrolyte Li6.25Al0.25La3Zr2O12.* ACS Applied Materials & Interfaces, 2019. **11**(15): p. 14463-14477.
228. Ye, R., Hamzelui, N., Ihrig, M., Finsterbusch, M., and Figgemeier, E., *Water-Based Fabrication of a Li|Li7La3Zr2O12|LiFePO4 Solid-State Battery—Toward Green Battery Production.* ACS Sustainable Chemistry & Engineering, 2022. **10**(23): p. 7613-7624.
229. Bresser, D., Buchholz, D., Moretti, A., Varzi, A., and Passerini, S., *Alternative binders for sustainable electrochemical energy storage - the transition to aqueous electrode processing and bio-derived polymers.* Energy & Environmental Science, 2018. **11**(11): p. 3096-3127.
230. Ho, D.L., Hammouda, B., Kline, S.R., and Chen, W.-R., *Unusual phase behavior in mixtures of poly(ethylene oxide) and ethyl alcohol.* Journal of Polymer Science Part B: Polymer Physics, 2006. **44**(3): p. 557-564.
231. Wen, S.J., Richardson, T.J., Ghantous, D.I., Striebel, K.A., Ross, P.N., and Cairns, E.J., *FTIR characterization of PEO + LiN(CF3SO2)2 electrolytes.* Journal of Electroanalytical Chemistry, 1996. **408**(1): p. 113-118.
232. Huang, B., Zheng, X., Jia, D., and Lu, M., *Design and synthesis of high-rate micron-sized, spherical LiFePO4/C composites containing clusters of nano/microspheres.* Electrochimica Acta, 2010. **55**(3): p. 1227-1231.
233. Wu, L., Zhong, S.-K., Liu, J.-Q., Lv, F., and Wan, K., *High tap-density and high performance LiFePO4/C cathode material synthesized by the combined sol spray-drying and liquid nitrogen quenching method.* Materials Letters, 2012. **89**: p. 32-35.
234. Xia, J., Fitch, B., Watson, A., Cabaniss, E., Black, R., and Yakovleva, M., *Printed Thin Lithium Foil with Flexible Thickness and Width for Industrial Battery Applications.* ECS Meeting Abstracts, 2020. **MA2020-02**(5): p. 976-976.
235. Wu, J., Yuan, L., Zhang, W.-X., Li, Z., Xie, X., and Huang, Y., *Reducing the Thickness of Solid-State Electrolyte Membranes for High-Energy Lithium Batteries.* Energy & Environmental Science, 2021. **14**: p. 12-36.
236. Balaish, M., Gonzalez-Rosillo, J.C., Kim, K.J., Zhu, Y., Hood, Z.D., and Rupp, J.L.M., *Processing thin but robust electrolytes for solid-state batteries.* Nature Energy, 2021. **6**: p. 227-239.
237. Finsterbusch, M., Danner, T., Tsai, C.-L., Uhlenbruck, S., Latz, A., and Guillon, O., *High Capacity Garnet-Based All-Solid-State Lithium Batteries: Fabrication and 3D-Microstructure Resolved Modeling.* ACS Applied Materials & Interfaces, 2018. **10**(26): p. 22329-22339.
238. Liu, H., Cheng, X.-B., Huang, J.-Q., Yuan, H., Lu, Y., Yan, C., Zhu, G.-L., Xu, R., Zhao, C.-Z., Hou, L.-P., He, C., Kaskel, S., and Zhang, Q., *Controlling Dendrite Growth in Solid-State Electrolytes.* ACS Energy Letters, 2020: p. 833-843.
239. Kasemchainan, J., Zekoll, S., Spencer Jolly, D., Ning, Z., Hartley, G.O., Marrow, J., and Bruce, P.G., *Critical stripping current leads to dendrite formation on plating in lithium anode solid electrolyte cells.* Nature Materials, 2019. **18**(10): p. 1105-1111.
240. Ihrig, M., Finsterbusch, M., Laptev, A.M., Tu, C.-h., Tran, N.T.T., Lin, C.-a., Kuo, L.-Y., Ye, R., Sohn, Y.J., Kaghazchi, P., Lin, S.-k., Fattakhova-Rohlfing, D., and Guillon, O., *Study of LiCoO2/Li7La3Zr2O12:Ta Interface Degradation in All-Solid-State Lithium Batteries.* ACS Applied Materials & Interfaces, 2022. **14**(9): p. 11288-11299.

241. Xia, Y., Fujieda, T., Tatsumi, K., Prosini, P.P., and Sakai, T., *Thermal and electrochemical stability of cathode materials in solid polymer electrolyte.* Journal of Power Sources, 2001. **92**(1): p. 234-243.
242. Su, S., Ma, J., Zhao, L., Lin, K., Li, Q., Lv, S., Kang, F., and He, Y.-B., *Progress and perspective of the cathode/electrolyte interface construction in all-solid-state lithium batteries.* Carbon Energy, 2021. **3**(6): p. 866-894.
243. Morita, M., Shibata, T., Yoshimoto, N., and Ishikawa, M., *Anodic behavior of aluminum current collector in LiTFSI solutions with different solvent compositions.* Journal of Power Sources, 2003. **119-121**: p. 784-788.
244. Il'ina, E.A., Druzhinin, K.V., Lyalin, E.D., Plekhanov, M.S., Talankin, I.I., Antonov, B.D., and Pankratov, A.A., *Li-In alloy: preparation, properties, wettability of solid electrolytes based on Li7La3Zr2O12.* Journal of Materials Science, 2022. **57**: p. 1291-1301.
245. Lu, Y., Zhao, C.-Z., Yuan, H., Cheng, X.-B., Huang, J.-Q., and Zhang, Q., *Critical Current Density in Solid-State Lithium Metal Batteries: Mechanism, Influences, and Strategies.* Advanced Functional Materials, 2021. **31**(18): p. 2009925.
246. Tan, D.H.S., Chen, Y.-T., Yang, H., Bao, W., Sreenarayanan, B., Doux, J.-M., Li, W., Lu, B., Ham, S.-Y., Sayahpour, B., Scharf, J., Wu, E.A., Deysher, G., Han, H.E., Hah, H.J., Jeong, H., Lee, J.B., Chen, Z., and Meng, Y.S., *Carbon-free high-loading silicon anodes enabled by sulfide solid electrolytes.* Science, 2021. **373**(6562): p. 1494-1499.
247. Yan, X., Li, Z., Wen, Z., and Han, W., *Li/Li7La3Zr2O12/LiFePO4 All-Solid-State Battery with Ultrathin Nanoscale Solid Electrolyte.* The Journal of Physical Chemistry C, 2017. **121**(3): p. 1431-1435.
248. Ye, R., Ihrig, M., Figgemeier, E., Fattakhova-Rohlfing, D., and Finsterbusch, M., *Aqueous Processing of LiCoO2-Li6.6La3Zr1.6Ta0.4O12 Composite Cathode for High-Capacity Solid-State Lithium Batteries.* ACS Sustainable Chemistry & Engineering, 2023. **in press**.
249. Uhlenbruck, S., Dornseiffer, J., Lobe, S., Dellen, C., Tsai, C.-L., Gotzen, B., Sebold, D., Finsterbusch, M., and Guillon, O., *Cathode-electrolyte material interactions during manufacturing of inorganic solid-state lithium batteries.* Journal of Electroceramics, 2017. **38**(2): p. 197-206.
250. Vardar, G., Bowman, W.J., Lu, Q., Wang, J., Chater, R.J., Aguadero, A., Seibert, R., Terry, J., Hunt, A., Waluyo, I., Fong, D.D., Jarry, A., Crumlin, E.J., Hellstrom, S.L., Chiang, Y.-M., and Yildiz, B., *Structure, Chemistry, and Charge Transfer Resistance of the Interface between Li7La3Zr2O12 Electrolyte and LiCoO2 Cathode.* Chemistry of Materials, 2018. **30**(18): p. 6259-6276.
251. Huang, X., Shen, C., Rui, K., Jin, J., Wu, M., Wu, X., and Wen, Z., *Influence of La2Zr2O7 Additive on Densification and Li+ Conductivity for Ta-Doped Li7La3Zr2O12 Garnet.* JOM, 2016. **68**(10): p. 2593-2600.
252. Huang, X., Lu, Y., Song, Z., Rui, K., Wang, Q., Xiu, T., Badding, M.E., and Wen, Z., *Manipulating Li2O atmosphere for sintering dense Li7La3Zr2O12 solid electrolyte.* Energy Storage Materials, 2019. **22**: p. 207-217.
253. Kim, K.H., Iriyama, Y., Yamamoto, K., Kumazaki, S., Asaka, T., Tanabe, K., Fisher, C.A.J., Hirayama, T., Murugan, R., and Ogumi, Z., *Characterization of the interface between LiCoO2 and Li7La3Zr2O12 in an all-solid-state rechargeable lithium battery.* Journal of Power Sources, 2011. **196**(2): p. 764-767.
254. Kato, T., Hamanaka, T., Yamamoto, K., Hirayama, T., Sagane, F., Motoyama, M., and Iriyama, Y., *In-situ Li7La3Zr2O12/LiCoO2 interface modification for advanced all-solid-state battery.* Journal of Power Sources, 2014. **260**: p. 292-298.
255. Ihrig, M., Dashjav, E., Laptev, A.M., Ye, R., Grüner, D., Ziegner, M., Odenwald, P., Finsterbusch, M., Tietz, F., Fattakhova-Rohlfing, D., and Guillon, O., *Increasing the performance of all-solid-state Li batteries by infiltration of Li-ion conducting polymer into LFP-LATP composite cathode.* Journal of Power Sources, 2022. **543**: p. 231822.

256. Jiang, Y., Yan, X., Ma, Z., Mei, P., Xiao, W., You, Q., and Zhang, Y., *Development of the PEO Based Solid Polymer Electrolytes for All-Solid State Lithium Ion Batteries.* Polymers, 2018. **10**(11): p. 1237.
257. Danks, A.E., Hall, S.R., and Schnepp, Z., *The evolution of 'sol–gel' chemistry as a technique for materials synthesis.* Materials Horizons, 2016. **3**(2): p. 91-112.
258. Wang, Y., Wu, L., Lin, Z., Tang, M., Ding, P., Guo, X., Zhang, Z., Liu, S., Wang, B., Yin, X., Chen, Z., Amine, K., and Yu, H., *Hydrogen Bonds Enhanced Composite Polymer Electrolyte for High-Voltage Cathode of Solid-State Lithium Battery.* Nano Energy, 2022: p. 107105.
259. Ohta, S., Komagata, S., Seki, J., Saeki, T., Morishita, S., and Asaoka, T., *All-solid-state lithium ion battery using garnet-type oxide and Li3BO3 solid electrolytes fabricated by screen-printing.* Journal of Power Sources, 2013. **238**: p. 53-56.
260. Ohta, S., Seki, J., Yagi, Y., Kihira, Y., Tani, T., and Asaoka, T., *Co-sinterable lithium garnet-type oxide electrolyte with cathode for all-solid-state lithium ion battery.* Journal of Power Sources, 2014. **265**: p. 40-44.
261. Liu, T., Ren, Y., Shen, Y., Zhao, S.-X., Lin, Y., and Nan, C.-W., *Achieving high capacity in bulk-type solid-state lithium ion battery based on Li6.75La3Zr1.75Ta0.25O12 electrolyte: Interfacial resistance.* Journal of Power Sources, 2016. **324**: p. 349-357.
262. Liu, T., Zhang, Y., Chen, R., Zhao, S.-X., Lin, Y., Nan, C.-W., and Shen, Y., *Non-successive degradation in bulk-type all-solid-state lithium battery with rigid interfacial contact.* Electrochemistry Communications, 2017. **79**: p. 1-4.
263. Ohta, S., Kobayashi, T., Seki, J., and Asaoka, T., *Electrochemical performance of an all-solid-state lithium ion battery with garnet-type oxide electrolyte.* Journal of Power Sources, 2012. **202**: p. 332-335.
264. Hou, A.-Y., Huang, C.-Y., Tsai, C.-L., Huang, C.-W., Schierholz, R., Lo, H.-Y., Tempel, H., Kungl, H., Eichel, R.-A., Chang, J.-K., and Wu, W.-W., *All-Solid-State Garnet-Based Lithium Batteries at Work–In Operando TEM Investigations of Delithiation/Lithiation Process and Capacity Degradation Mechanism.* Advanced Science, 2023. **10**: p. 2205012.
265. Rosen, M., Finsterbusch, M., Guillon, O., and Fattakhova-Rohlfing, D., *Free standing dual phase cathode tapes – scalable fabrication and microstructure optimization of garnet-based ceramic cathodes.* Journal of Materials Chemistry A, 2021. **10**: p. 2320-2326.
266. Ihrig, M., Kuo, L.-Y., Lobe, S., Laptev, A.M., Lin, C.-a., Tu, C.-h., Ye, R., Kaghazchi, P., Cressa, L., Eswara, S., Lin, S.-k., Guillon, O., Fattakhova-Rohlfing, D., and Finsterbusch, M., *Thermal Recovery of the Electrochemically Degraded LiCoO2/Li7La3Zr2O12:Al,Ta Interface in an All-Solid-State Lithium Battery.* ACS Applied Materials & Interfaces, 2023. **15**(3): p. 4101-4112.
267. Nie, K., Hong, Y., Qiu, J., Li, Q., Yu, X., Li, H., and Chen, L., *Interfaces Between Cathode and Electrolyte in Solid State Lithium Batteries: Challenges and Perspectives.* Frontiers in Chemistry, 2018. **6**: p. 616.
268. Lu, Y., Zhao, C.-Z., Zhang, R., Yuan, H., Hou, L.-P., Fu, Z.-H., Chen, X., Huang, J.-Q., and Zhang, Q., *The carrier transition from Li atoms to Li vacancies in solid-state lithium alloy anodes.* Science Advances, 2021. **7**(38): p. eabi5520.
269. Tan, D.H.S., Banerjee, A., Chen, Z., and Meng, Y.S., *From nanoscale interface characterization to sustainable energy storage using all-solid-state batteries.* Nature Nanotechnology, 2020. **15**(3): p. 170-180.
270. Xiang, Y., Li, X., Cheng, Y., Sun, X., and Yang, Y., *Advanced characterization techniques for solid state lithium battery research.* Materials Today, 2020. **36**: p. 139-157.
271. Zheng, C., Tang, S., Wen, F., Peng, J., Yang, W., Lv, Z., Wu, Y., Tang, W., Gong, Z., and Yang, Y., *Reinforced Cathode | Garnet Interface for High-Capacity All-Solid-State Batteries.* Materials Futures, 2022. **1**(4): p. 045103.

272. Kotobuki, M., Munakata, H., Kanamura, K., Sato, Y., and Yoshida, T., *Compatibility of Li7La3Zr2O12 Solid Electrolyte to All-Solid-State Battery Using Li Metal Anode.* Journal of the Electrochemical Society, 2010. **157**(10): p. A1076-A1079.
273. Kotobuki, M., Kanamura, K., Sato, Y., and Yoshida, T., *Fabrication of all-solid-state lithium battery with lithium metal anode using Al2O3-added Li7La3Zr2O12 solid electrolyte.* Journal of Power Sources, 2011. **196**(18): p. 7750-7754.
274. Scheld, W.S., Lobe, S., Dellen, C., Ihrig, M., Häuschen, G., Hoff, L.C., Finsterbusch, M., Uhlenbruck, S., Guillon, O., and Fattakhova-Rohlfing, D., *Rapid thermal processing of garnet-based composite cathodes.* Journal of Power Sources, 2022. **545**: p. 231872.
275. Watanabe, K., Tashiro, A., Ichinose, Y., Takeno, S., Suematsu, K., Mitsuishi, K., and Shimanoe, K., *Lowering the sintering temperature of Li7La3Zr2O12 electrolyte for co-fired all-solid-state batteries via partial Bi substitution and precise control of compositional deviation.* Journal of the Ceramic Society of Japan, 2022. **130**(7): p. 416-423.

Band / Volume 597
Nanostructures of Transition Metal Sulfides for Anion Exchange Membrane Water Electrolysis
L. Xia (2022), 161 pp
ISBN: 978-3-95806-670-0

Band / Volume 598
Recycling- und Defossilisierungsmaßnahmen der Energieintensiven Industrie Deutschlands im Kontext von CO_2-Reduktionsstrategien
F. Kullmann (2022), XII, 237 pp
ISBN: 978-3-95806-672-4

Band / Volume 599
IEK-14 Report 2022
Research contributions for the energy transition and structural change in the Rhineland
B. Emonts (Ed.) (2022), 83 pp
ISBN: 978-3-95806-676-2

Band / Volume 600
Development of Glass-based Sealants for the Joining of Oxygen Transport Membranes
X. Li (2022), IV, 159 pp
ISBN: 978-3-95806-677-9

Band / Volume 601
High-resolution imaging of transport processes with GPR full-waveform inversion
P. Haruzi (2022), iv, 173 pp
ISBN: 978-3-95806-678-6

Band / Volume 602
Synthesis of optimized cathode materials for all-solid-state lithium batteries
C. Roitzheim (2022), xv, 221 pp
ISBN: 978-3-95806-679-3

Band / Volume 603
Development of components based on Ti_2AlC/fiber composites for aggressive environmental conditions
S. Badie (2023), x, 161 pp
ISBN: 978-3-95806-680-9

Band / Volume 604
Multiregionales Energiesystemmodell mit Fokus auf Infrastrukturen
T. M. Groß (2023), xx, 235 pp
ISBN: 978-3-95806-681-6

Schriften des Forschungszentrums Jülich
Reihe Energie & Umwelt / Energy & Environment

Band / Volume 605
Temporal Aggregation Methods for Energy System Modeling
M. A. C. Hoffmann (2023), XXVI, 341 pp
ISBN: 978-3-95806-683-0

Band / Volume 606
Examining transport in the Upper Troposphere – Lower Stratosphere with the infrared limb imager GLORIA
L. Krasauskas (2023), v, 107 pp
ISBN: 978-3-95806-691-5

Band / Volume 607
Sustainable Fabrication of Ceramic Solid Electrolytes for Solid-State Lithium Batteries
R. Ye (2023), vi, 119 pp
ISBN: 978-3-95806-694-6

Weitere ***Schriften des Verlags im Forschungszentrum Jülich*** unter
http://wwwzb1.fz-juelich.de/verlagextern1/index.asp

Energie & Umwelt / Energy & Environment
Band / Volume 607
ISBN 978-3-95806-694-6

Mitglied der Helmholtz-Gemeinschaft

JÜLICH
Forschungszentrum